Enhanced PEEC Electromagnetic Modeling For RF/Microwave Multi-layer Circuits

By

Hu Mengna

A Thesis Submitted in Partial Fulfillment of the
Requirements for the Degree of
Master of Philosophy

July 2004

ABSTRACT

With the ever-increasing operating frequency and complexity of microwave circuits and systems, three-dimensional EM environment becomes more and more dominant, computer simulation of microwave circuits and systems relies greatly on accurate models with both physical information and electromagnetic effects. While various advanced accurate but time consuming EM models have being developed, the research in this thesis places attention to less accurate but super fast EM models, which are also highly demanding in practical circuit initial design. Among various effective but less accurate EM simulation techniques, the enhancement of the well known coupled EM and circuit simulation approach, Partial Element Equivalent Circuit (PEEC) is fully studied in this thesis. It is an effective method to convert three-dimensional multi-conductor structures to circuit domain descriptions.

Based on the traditional PEEC algorithm, some enhancements are proposed in this thesis. Firstly, a mixed rectangular and annular meshing scheme based PEEC approach is developed, wherein the surfaces of irregularly shaped conducting structures, especially mixed rectangular and annular ones, are represented by two basic building blocks, rectangles and annular sectors. A coupled EM-circuit formulation is obtained through the separation of the scalar and vector potential interactions between a pair of directional pulse basis functions for the derivation of equivalent circuit model. Secondly, when the operating frequency of the microwave circuits and systems is very high or when the problem under analysis involves radiation loss, a full-wave technique is proposed for the PEEC approach to considerablely minimize the simulation error brought by quasi-static approximation in the traditional method. Finally, an effective microwave

circuit design and optimization approach based on aggressive space mapping (ASM) method and the PEEC model developed in this research is demonstrated, where the PEEC model is set as the coarse model in ASM because of its efficiency and the resultant equivalent circuit model.

摘要

隨著微波電路及系統工作頻率以及複雜程度的不斷提高，系統內的三維電磁耦合效應變得愈發重要。微波電路及系統的仿真成功與否，在很大程度上取決於一個既含有物理尺寸信息又包括電磁耦合效應的模型的建立。儘管各種各樣精確但耗時的電磁模型曾被提出過，本論文更傾向於研究不完全精確但非常之快的電磁模型的建立，該模型在實際電路的初始設計中是非常重要的。在上述的各種電磁仿真技術中，該論文選取了一種電磁電路混合仿真方法，PEEC，各方面的性能改善，作爲研究課題。該方法可以有效地將三維多導體結構的場問題轉變到電路域進行描述進而變成爲一個電路問題。

基於傳統算法，本論文提出了兩點改進。首先本文提出了一種基於矩形扇形混合剖分機制的 PEEC 方法，在該方法中，不規則形狀導體，特別是矩形扇形混合的導體，由兩個基本構件模塊，矩形和扇形剖分單元，進行剖分逼近。然後從一對變方向性脈衝基函數之間相互作用的矢量和標量位函數中可以分離出一套混合電磁電路公式，從而推導出其等效電路模型。其次，當微波電路及系統的工作頻率非常之高或者待仿真系統並非一個電小尺寸系統又或者待仿真系包含有輻射損耗時，爲了避免由於傳統 PEEC 方法中採用的準靜態近似而引起的計算誤差，全波技術被應用於 PEEC 方法。最後，一個有效的基於 ASM 的微波電路設計和優化方法於本論文中被提出。由於 PEEC 的仿真效率以及其等效電路模型等方面的優勢，在該方法中，PEEC 模型被作爲粗略模型，進而由 ASM 方法進行優化。

TABLE OF CONTENTS

1

INTRODUCTION

1.1. PEEC Modeling Method

Microwave circuits are becoming ever more commercially and militarily viable and, coupled with large scale production, computer simulation of circuits and systems is an essential part of the development process, and accurate component and circuit models are required to ensure that the simulations reliably predict real-world performance.

With the ever-increasing operating frequency and complexity of the circuit, wavelengths become smaller and smaller with respect to device and circuit dimensions and the three-dimensional EM environment becomes more significant. A fundamental problem in designing RF circuits is the parasitic effects between closely spaced elements in EM environment, which affect the frequency behavior of the circuits. So if reliable, high yielding and optimized designs of microwave and millimeter-wave circuits are to be achieved, models with both physical/geometrical information and electromagnetic effects become necessary. There are several EM simulation techniques, such as Method of Moment (MoM), Boundary Element Method (BEM), Finite-Difference Time Domain (FDTD), Finite Difference Method (FDM), Finite Element Method (FEM), Transmission Line Matrix (TLM), etc.

With the increase of the complexity of today's electronic system, for radio-frequency (RF) design, in particular, there are always both passive structures and nonlinear active components in one physical system. The passive structures, such as microwave filters, couplers, can only be accurately modeled by electromagnetic (EM) field analysis while the active components, such as transistors, require time domain circuit analysis. To understand the performance of the whole system, the combination of the two analytical technologies is needed. The Partial Element Equivalent Circuit (PEEC) approach, developed by A.E.Ruehli in 1974, is particularly suitable for this kind of mixed EM and circuit problem. It can extract an equivalent circuit model from the original passive structure.

1.2. Overview of the work

However, conventional PEEC approach, originally formulated for modeling thin and long interconnect structure, assumes rectangular discretization scheme and filamental current flow, so it is not well suited for modeling irregular structures, such as a generally used circular spiral inductor.

In conventional PEEC, quasi-static approximation is made, because the kernels of the quasi-static integral equations are considerably simpler than full-wave kernels, which will make the analysis less cumbersome and clearer. But when the problem under analysis is a radiation one or the structure of interest has dimensions comparable to or even larger than the operating wavelength, this approximation will be no longer acceptable.

Aiming at breaking these two limitations, two enhancements of the conventional algorithms are proposed in this work.

1.3. Original Contributions

Following are two original contributions in this work:

1. Generalization of PEEC to model irregular geometries, especially mixed rectangular and circular geometries

2. Application of full-wave techniques to PEEC modeling method

1.4. Organization of the thesis

The thesis begins with the introduction of the fundamentals of the conventional PEEC modeling technique. Basic mathematical formulations are provided in this chapter for better understanding the theory. Chapter three focuses on the generalization of PEEC to model irregular structures. A new meshing scheme is proposed to facilitate PEEC to model both rectangular and irregular geometries, and formulas to get partial elements in the new meshing scheme are given too. The application of full wave technique in PEEC to replace quasi-static approximation is discussed in chapter four. Some design examples are discussed at the end of chapter three and four to validate the efficiency and accuracy of the enhanced PEEC, and also give a guideline to design and optimize LTCC multi-layer RF circuit with PEEC modeling technique.

2

CLASSICAL PARTIAL ELEMENT EQUIVALENT CIRCUIT MODELING

2.1. Introduction

In early 1970s, based on the study of inductance [1], [5], [6] and capacitance calculation [2] of the three dimensional multi-conductor system, and also the electrical analysis of the circuit interconnections [3], A. E. Reuhli developed the Partial Element Equivalent Circuit (PEEC) modeling method, to model three dimensional multi-layer multi-conductor systems. It is based on the conversion of the Mixed Potential Integral Equation (MPIE) to circuit domain, which provides us a better understanding of the electrical behavior of mixed EM-circuit problems.

The PEEC method is developed from an integral equation description of the geometry. Then it is interpreted in terms of circuit elements, partial inductances and partial capacitances, the resultant equivalent circuit can then be solved with conventional circuit solvers, such as SPICE. Since this algorithm can be applied to a wide range of the problems, which include both circuit and field theories, and also help us understand the basic electrical performance of these problems in both time and frequency domain, it is worthwhile to study the basic concepts to have a general understanding of this modeling method. So in this chapter, the basic principles, as well as the mathematical formulation for conventional PEEC algorithm will be addressed.

2.2. Mathematical Formulation in PEEC

2.2.1 Basic Integral Equation

We start with Ohm's law in the field form:

$$\mathbf{E} = \frac{\mathbf{J}}{\sigma} \tag{2-1}$$

The electric field is broken up into an incident field, $\mathbf{E}^i$ and a scattered field, $\mathbf{E}^s$.

$$\mathbf{E} = \mathbf{E}^i + \mathbf{E}^s \tag{2-2}$$

The incident field can also be represented in terms of the retarded potentials:

$$\mathbf{E}^s = -\nabla\Phi - \frac{\partial A}{\partial t} \tag{2-3}$$

Substitute (2-1) and (2-3) into (2-2):

$$\frac{\mathbf{J}(\mathbf{r},t)}{\sigma} = \mathbf{E}^i(\mathbf{r},t) + \left[-\frac{\partial}{\partial t}\mathbf{A}(\mathbf{r},t) - \nabla\Phi(\mathbf{r},t)\right] \tag{2-4}$$

In (2-4), $\mathbf{J}$ is the current density, σ is the conductivity, $\mathbf{A}$ is the vector magnetic potential and Φ is the scalar electric potential.

$$\mathbf{A}(\mathbf{r},t) = \sum_{k=1}^{K} \frac{\mu}{4\pi} \int_{v_k} G(\mathbf{r},\mathbf{r}')\mathbf{J}(\mathbf{r}',t')dv_k' \tag{2-5}$$

$$\Phi(\mathbf{r},t) = \sum_{k=1}^{K} \frac{1}{4\pi\varepsilon} \int_{v_k} G(\mathbf{r},\mathbf{r}')q(\mathbf{r}',t')dv_k' \tag{2-6}$$

in which, $G(\mathbf{r},\mathbf{r}')$ is the Green's function, which will be discussed in details later. In time domain, the following relationship represents the time delay in free space with propagation speed of c,

$$t' = t - \frac{|\mathbf{r}-\mathbf{r}'|}{c} \tag{2-7}$$

Substitute equations (2-5), (2-6) into equation (2-4), it can be represented in an integral form:

$$\mathbf{E}^i(\mathbf{r},t) = \frac{\mathbf{J}(\mathbf{r},t)}{\sigma} + \sum_{k=1}^{K} \frac{\mu}{4\pi} \frac{\partial}{\partial t} \left[\int_{v_k} G(\mathbf{r},\mathbf{r}')\mathbf{J}(\mathbf{r}',t')dv_k' \right] + \sum_{k=1}^{K} \frac{1}{4\pi\varepsilon} \nabla \left[\int_{v_k} G(\mathbf{r},\mathbf{r}')q(\mathbf{r}',t')dv_k' \right] \tag{2-8}$$

Equation (2-8) is called Mixed Potential Integral Equation (MPIE) [4].

There are two unknowns in a multi-conductor or multi-wire system: charge density q on the surfaces and current density $\mathbf{J}$ within the conductors. Suppose these two unknowns are both locally constant functions and apply Galerkin's matching to the MPIE, equation (2-8), an equivalent circuit model can be generated for the structure under analysis. Assuming $\mathbf{J}$ and q to be locally constant variables, the original structure can be discretized into a number of surface and volume cells, and these two variables are supposed to be constant over these cells.

2.2.2 Current and Charge discretization

Representing the current density $\mathbf{J}$ in terms of orthogonal components:

$$\mathbf{J}(\mathbf{r},t) = J_x(\mathbf{r},t)\hat{\mathbf{x}} + J_y(\mathbf{r},t)\hat{\mathbf{y}} + J_z(\mathbf{r},t)\hat{\mathbf{z}} \tag{2-9}$$

A rectangular volume cell is defined by a pulse function:

$$P_n^{\gamma}(\mathbf{r}) = \begin{cases} 1 & \mathbf{r} \in nth \text{ volume cell for the } J_{\gamma} \text{ component} \\ 0 & \mathbf{r} \in \text{elsewhere} \end{cases} \tag{2-10}$$

Here, for ease of presentation, $\gamma = x, y, z$, representing three orthogonal current directions to avoid repetition.

The current density is then expanded as:

$$J_{\gamma}(\mathbf{r},t) = \sum_{n=1}^{N} J_n^{\gamma}(t) P_n^{\gamma}(\mathbf{r}) \tag{2-11}$$

This basis function involved method applied above is called method of subsections. Since the basis function only exists over subsections of the domain of $J_{\gamma}(\mathbf{r},t)$, each $J_n^{\gamma}(t)$ of the expansion (2-11) affects the approximation of $J_{\gamma}(\mathbf{r},t)$ only over a subsection of the region of interest.

Then (2-8) can be rewritten as:

$$\frac{J^{\gamma}(\mathbf{r},t)}{\sigma} + \sum_{k=1}^{K}\sum_{n=1}^{N} \frac{\mu}{4\pi}\left[\int_{v_{nk}} G(\mathbf{r},\mathbf{r}')dv'_{nk}\right]\frac{\partial J_{nk}^{\gamma}(t')}{\partial t} + \sum_{k=1}^{K}\frac{1}{4\pi\varepsilon}\frac{\partial}{\partial\gamma}\left[\int_{v_k} G(\mathbf{r},\mathbf{r}')q(\mathbf{r}',t')dv'_k\right] = E_{\gamma}^{i}(\mathbf{r},t) \tag{2-12}$$

in which, *nk* represents the *nth* element on conductor k.

Furthermore, the charge density q is written as another expansion function of the same type. Since free charge is restricted to the outside surfaces of all conductors, a rectangular surface cell is defined also by a pulse function:

$$p_m(\mathbf{r}) = \begin{cases} 1 & \mathbf{r} \in mth \text{ surface cell for q} \\ 0 & \mathbf{r} \in \text{elsewhere} \end{cases} \tag{2-13}$$

The charge density can be expanded:

$$q(\mathbf{r},t)=\sum_{m=1}^{M} q_m(t)p_m(\mathbf{r}) \tag{2-14}$$

Then equation (2-12) turns out to be:

$$\frac{J^{\gamma}(\mathbf{r},t)}{\sigma}+\sum_{k=1}^{K}\sum_{n=1}^{N}\frac{\mu}{4\pi}\left[\int_{v_{nk}} G(\mathbf{r},\mathbf{r}')dv'_{nk}\right]\frac{\partial J^{\gamma}_{nk}(t')}{\partial t}$$
$$+\sum_{k=1}^{K}\sum_{m=1}^{M}\frac{1}{4\pi\varepsilon}\frac{\partial}{\partial\gamma}\left[q_{mk}(t')\int_{s_{mk}} G(\mathbf{r},\mathbf{r}')ds'_{mk}\right]=E^{i}_{\gamma}(\mathbf{r},t) \tag{2-15}$$

in which, mk represents the m^{th} cell on conductor k.

2.2.3 Galerkin Matching Method

After the discretization of MPIE, the next step is to apply Galerkin matching to convert equation (2-15) into a set of coupled equations, from which the inductive and capacitive elements of the equivalent circuit model can be obtained.

First, an inner product operation is defined:

$$\langle f,g\rangle=\int_{v} fgdv \tag{2-16}$$

If f is chosen to be equation (2-15) and g is the volume pulse function defined in (2-10) divided by the cross section area, called weighting function or testing function, the integration of (2-15) over the l^{th} cell leads to:

$$\frac{1}{a_l\sigma}\int_{v_l} J^{\gamma}(\mathbf{r},t)dv_l + \sum_{k=1}^{K}\sum_{n=1}^{N}\frac{\mu}{4\pi}\frac{1}{a_l}\left[\int_{v_l}\int_{v_{nk}} G(\mathbf{r},\mathbf{r}')dv'_{nk}dv_l\right]\frac{\partial J^{\gamma}_{nk}(t')}{\partial t}$$
$$+\sum_{k=1}^{K}\sum_{m=1}^{M}\frac{1}{4\pi\varepsilon}\frac{1}{a_l}\int_{v_l}\frac{\partial}{\partial\gamma}\left[q_{mk}(t')\int_{s_k} G(\mathbf{r},\mathbf{r}')ds'_k\right]dv_l = \left\langle E^i_{\gamma}(\mathbf{r},t), \frac{p^{\gamma}_l E^i_{\gamma}(\mathbf{r})}{a_l}\right\rangle \tag{2-17}$$

Now there is a set of N_T equations for γ components with $l = 1,2,...,N_T$. If the continuity equation, equation (2-18), is substituted into equation (2-17), $\mathbf{J}$ and q can be easily solved.

$$\nabla \bullet \mathbf{J} = -\frac{\partial \rho}{\partial t} \tag{2-18}$$

But in PEEC, our objective is to solve equation (2-17) in the circuit domain, so the equivalent circuit model must be obtained first. Notice that if there is no incident field,

$$E^i_{\gamma} = 0 \tag{2-19}$$

With the assumption of the absence of incident field, equation (2-17) has the same form as:

$$V_R + V_L + V_C = 0 \tag{2-20}$$

in which, V_R, V_L, V_C represent the resistive, inductive and capacitive voltage drop across the cell respectively.

$$V_R = \frac{1}{a_l\sigma}\int_{v_l} J^{\gamma}(\mathbf{r},t)dv_l \tag{2-21}$$

$$V_L = \sum_{k=1}^{K}\sum_{n=1}^{N}\frac{\mu}{4\pi}\frac{1}{a_l}\left[\int_{v_l}\int_{v_{nk}} G(\mathbf{r},\mathbf{r}')dv'_{nk}dv_l\right]\frac{\partial J^{\gamma}_{nk}(t')}{\partial t} \tag{2-22}$$

$$V_C = \sum_{k=1}^{K}\sum_{m=1}^{M}\frac{1}{4\pi\varepsilon}\frac{1}{a_l}\int_{v_l}\frac{\partial}{\partial\gamma}\left[q_{mk}(t')\int_{s_k}G(\mathbf{r},\mathbf{r}')ds'_k\right]dv_l \tag{2-23}$$

2.3. Partial Inductance

2.3.1 General Formula for partial mutual inductance

Based on equation (2-22) in section 2.2.3, the current density is written to be the total current divided by the cross sectional area perpendicular to the direction of current flow,

$$V_L = \sum_{k=1}^{K}\sum_{n=1}^{N}\frac{\mu}{4\pi}\frac{1}{a_l a_{nk}}\left[\int_{v_l}\int_{v_{nk}}G(\mathbf{r},\mathbf{r}')dv'_{nk}dv_l\right]\frac{\partial I^{\gamma}_{nk}(t')}{\partial t} \tag{2-24}$$

It has the same form as the voltage-current relationship for an inductor:

$$V_L = \sum_{k=1}^{K}\sum_{n=1}^{N}Lp_{l,nk}\frac{dI^{\gamma}_{nk}(t')}{dt} \tag{2-25}$$

Compare equations (2-24) and (2-25), $Lp_{l,nk}$ can be represented as the integration form of the Green's function:

$$Lp_{l,nk} = \frac{\mu}{4\pi}\frac{1}{a_l a_{nk}}\left[\int_{v_l}\int_{v_{nk}}G(\mathbf{r},\mathbf{r}')dv'_{nk}dv_l\right] \tag{2-26}$$

The above equation provides us the way to calculate the partial self-inductance ($l = nk$) and partial mutual inductance ($l \neq nk$) between two arbitrarily shaped conductors having same current orientation.

2.3.2 Mutual Inductance between two Thin Rectangular Tapes

In the general formula (2-26) to calculate the partial inductance, to simplify the calculation, free space Green's function is adopted at first:

$$G(\mathbf{r},\mathbf{r}') = \frac{1}{|\mathbf{r}-\mathbf{r}'|} \tag{2-27}$$

However, it is only suitable for conducting cells embedded in a homogeneous substrate of infinite extent. It can be used as a basic element of the quasi-static Green's function of a microstrip substrate by applying the ray-tracing technique, which will be introduced in section 2.6.

While calculating the inductance, the current direction on each inductive cell is also an important parameter. Since the inductive cells are all rectangles in conventional PEEC, there are only two possibilities, parallel or perpendicular, for the relationship between the current directions on two inductive cells. It is obvious that the mutual inductance between two perpendicular cells is zero. So to get the inductance between two thin strips, we only need to consider two parallel filaments located inside a homogeneous region, like the one shown in figure. 2-3 (a). In such cases, equation (2-26) reduces to the famous Neumann's formula:

$$Lp_{l,nk}^{f} = \frac{\mu}{4\pi}\int_{l_l}\int_{l_{nk}} \frac{dl'_{nk}\,dl_l}{|\mathbf{r}-\mathbf{r}'|} \tag{2-28}$$

This integration leads to an analytical form:

$$Lp_{l,nk}^{f} = \frac{\mu}{4\pi}\sum_{k=1}^{4}(-1)^{k+1}\left[z_k \ln\left(z_k + \sqrt{z_k^2+\rho^2}\right) - \sqrt{z_k^2+\rho^2}\right] \tag{2-29}$$

in which, $z_1 = l_3 - l_1$, $z_2 = l_3 + l_2 - l_1$, $z_3 = l_3 + l_2$, $z_4 = l_3$

To obtain the mutual inductance $Lp^{t}_{l,nk}$ between two parallel thin strips of zero thickness such as the one shown in figure 2-3 (b), $Lp^{f}_{l,nk}$ is integrated over all filaments over both strips.

$$Lp^{t}_{l,nk} = \frac{\mu}{4\pi}\frac{1}{w_l w_{nk}}\sum_{i=1}^{4}\sum_{j=1}^{4}(-1)^{i+j}\left[\frac{y_j^2 - P^2}{2}x_i \ln[x_i + \rho]\right.$$
$$\left. + \frac{x_j^2 - P^2}{2}y_i \ln[y_i + \rho] - \frac{1}{6}\left(x^2 + y^2 - 2P^2\right)\rho - x_i y_j P \tan^{-1}\frac{x_i y_j}{\rho P}\right] \quad (2\text{-}30)$$

in which,

$$\rho = \sqrt{x_i^2 + y_j^2 + P^2}$$

and

$x_1 = dl - l_l$ $\quad$ $y_1 = E - w_l$

$x_2 = dl + l_{nk} - l_l$ $\quad$ $y_2 = E + w_{nk} - w_l$

$x_3 = dl + l_{nk}$ $\quad$ $y_3 = E + w_{nk}$

$x_4 = dl$ $\quad$ $y_4 = E$

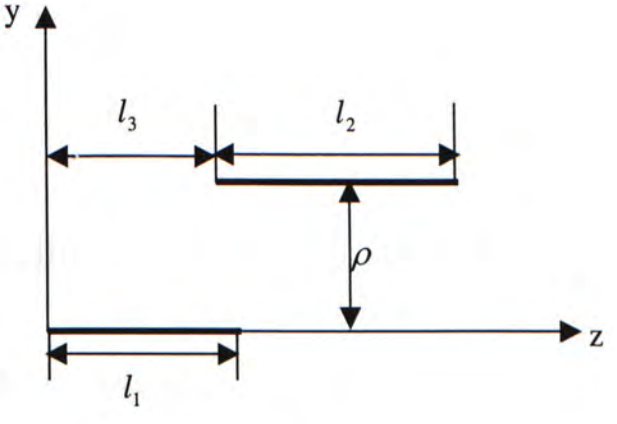

(a)

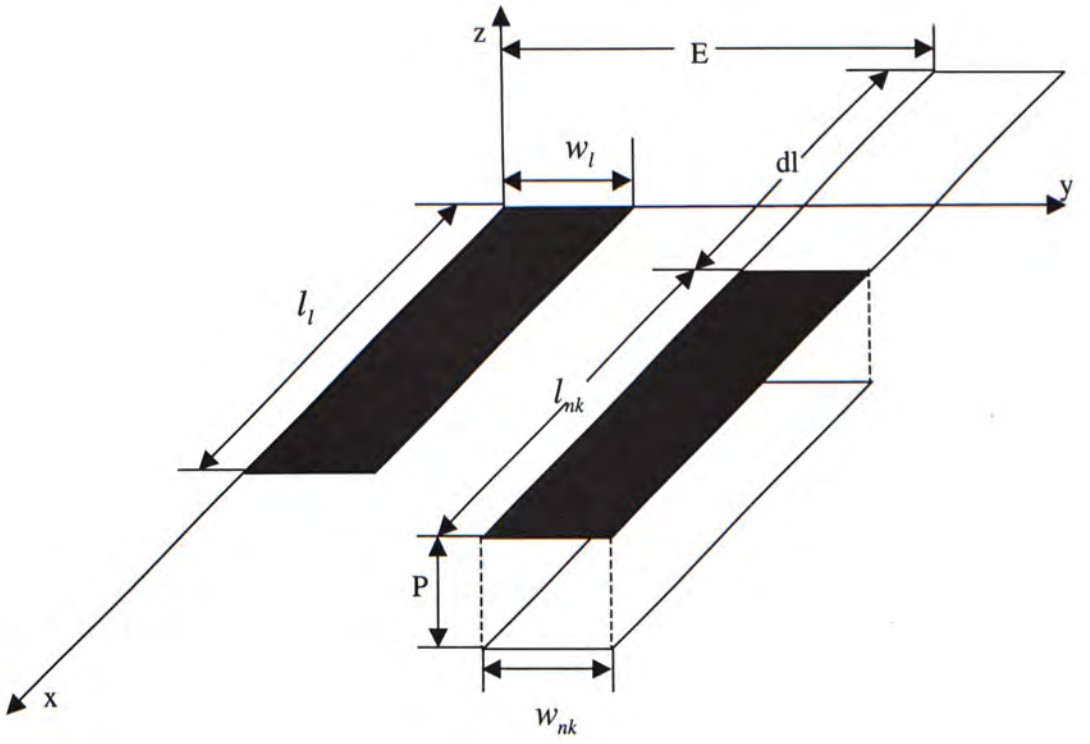

(b)

Fig. 2-3 (a) Two parallel filaments

(b) Two parallel thin inductive cells

Notice that the self-inductance can be calculated by setting $l_l = l_{nk}$, $w_l = w_{nk}$ and $E = P = dl = 0$ in equation (2-30). In the derivation, since the free-space Green's function has been used, equation (2-30) is applicable only for the case of the cells inside a homogenous region of infinite extent.

2.4. Partial Capacitance

2.4.1 General Formula for partial mutual capacitance

Equation (2-23) in section 2.2.3 is related to the capacitive portion in equivalent circuit model.

Firstly, an approximation is made:

$$\int_{v_l} \frac{\partial}{\partial \gamma} F_{mk}(\mathbf{r},\mathbf{r}',t')dv_l \cong a_l\left[F_{mk}(\mathbf{r}_l^+,\mathbf{r}',t') - F_{mk}(\mathbf{r}_l^-,\mathbf{r}',t')\right] \tag{2-31}$$

where $F_{mk}(\mathbf{r},\mathbf{r}',t') = q_{mk}(t')\int_{S_{mk}} G(\mathbf{r},\mathbf{r}')ds'_{mk}$;

$r_l^+ = \left(x_l + \frac{\Delta x_l}{2}, y_l, z_l\right)$, $r_l^- = \left(x_l - \frac{\Delta x_l}{2}, y_l, z_l\right)$, if $\gamma = x$.

Similar forms for r_l^+ and r_l^- can be got for $\gamma = y, z$

This approximation reveals the relationship between the capacitive cells and the inductive cells in the same structure under analysis: the capacitive cells should be shifted by half the size of the corresponding inductive cells.

Substituting (2-31) into (2-23):

$$V_C = \sum_{k=1}^{K}\sum_{m=1}^{M} \frac{q_{mk}(t')}{4\pi\varepsilon}\left[\int_{S_{mk}} G(\mathbf{r}_l^+,\mathbf{r}')ds'_{mk} - \int_{S_{mk}} G(\mathbf{r}_l^-,\mathbf{r}')ds'_{mk}\right] \tag{2-32}$$

The charge density is written to be the total charge divided by the cross sectional area:

$$V_C = \sum_{k=1}^{K}\sum_{m=1}^{M} \frac{1}{4\pi\varepsilon}\frac{Q_{mk}(t')}{S_{mk}}\left[\int_{S_{mk}} G(\mathbf{r}_l^+,\mathbf{r}')ds'_{mk} - \int_{S_{mk}} G(\mathbf{r}_l^-,\mathbf{r}')ds'_{mk}\right] \tag{2-33}$$

It has the same form as the voltage-charge relationship for a capacitor:

$$V_C = \sum_{k=1}^{K}\sum_{m=1}^{M} Q_{mk}(t')\left[pp_{l,mk}^+ - pp_{l,mk}^-\right] = \Phi^+ - \Phi^- \tag{2-34}$$

where $pp_{l,mk}^{+}$ and $pp_{l,mk}^{-}$ are both the coefficients of potential.

In general,

$$pp_{l,mk}^{\pm} = \frac{1}{4\pi\varepsilon}\frac{1}{S_{mk}}\int_{S_{mk}} G\left(\mathbf{r}_l^{\pm}, \mathbf{r}'\right) ds'_{mk} \tag{2-35}$$

$$\Phi^{\pm} = \sum_{k=1}^{K}\sum_{m=1}^{M}\frac{1}{4\pi\varepsilon} q_{mk}(t') \int_{S_{mk}} G\left(\mathbf{r}_l^{\pm}, \mathbf{r}'\right) ds'_{mk} \tag{2-36}$$

From the method of subsections, the potential vector is matched to the known potential at the center of each cell in the system and $q_{mk}(t')$ is assumed to be of constant density over cell mk. Equation (2-36) is integrated over cell mk, the left hand side is then $\Phi_l^{\pm} S_l^{\pm}$ since all the cells are supposed to be equal-potential one [2]:

$$\Phi_l^{\pm} = \sum_{k=1}^{K}\sum_{m=1}^{M}\frac{1}{4\pi\varepsilon}\frac{Q_{mk}(t')}{S_l^{\pm} S_{mk}} \int_{S_l^{\pm}}\int_{S_{mk}} G\left(\mathbf{r}_l^{\pm}, \mathbf{r}'\right) ds'_{mk}\, ds_l^{\pm} \tag{2-37}$$

Correspondingly, the coefficients of potential are re-defined to be:

$$pp_{l,mk}^{\pm} = \frac{1}{4\pi\varepsilon}\frac{1}{S_l^{\pm} S_{mk}} \int_{S_l^{\pm}}\int_{S_{mk}} G\left(\mathbf{r}_l^{\pm}, \mathbf{r}'\right) ds'_{mk}\, ds_l^{\pm} \tag{2-38}$$

in which, $S_l^{\pm}$ represents the capacitive surface cells associating at both ends of the inductive volume cell l. The coefficient of potential matrix **PP** is constructed by collecting all the coefficients. Suppose $\mathbf{CS} = \mathbf{PP}^{-1}$, then:

$$C_{i,i} = \sum_{j=1}^{N_T} CS_{i,j}\ ,\ i = 1,2,\ldots,N_T \tag{2-39}$$

$$C_{i,j} = -CS_{i,j},\ i \neq j \tag{2-40}$$

where $C_{i,i}$ is the self capacitance of node i and $C_{i,j}$ is the coupling capacitance between node i and node j. N_T is the total number of cells in the multi-conductor system.

2.4.2 Mutual Capacitance Between Two Thin Rectangular Strips

Based on equation (2-38), the potential coefficients between two parallel thin tapes of zero thickness such as shown in figure 2-4, $pp^{\pm}_{l,mk}$, can be written to be the closed-form expression [2]:

$$pp^{\pm}_{l,mk} = \frac{1}{4\pi\varepsilon}\frac{1}{S^{\pm}_{l}S_{mk}}\sum_{i=1}^{4}\sum_{j=1}^{4}(-1)^{i+j}\left[\frac{y_j^2 - C^2}{2}x_i \ln[x_i + \rho]\right.$$
$$\left. + \frac{x_i^2 - C^2}{2}y_j \ln[y_j + \rho] - \frac{1}{6}\left(x^2 + y^2 - 2C^2\right)\rho - x_i y_j C \tan^{-1}\frac{x_i y_j}{\rho C}\right] \tag{2-41}$$

in which,

$$\rho = \sqrt{x_i^2 + y_j^2 + C^2}$$

and

$$x_1 = l^{\pm}_{l,mk} - \frac{l^{\pm}_{l}}{2} - \frac{l_{mk}}{2} \qquad y_1 = w^{\pm}_{l,mk} - \frac{w^{\pm}_{l}}{2} - \frac{w_{mk}}{2}$$

$$x_2 = l^{\pm}_{l,mk} + \frac{l^{\pm}_{l}}{2} - \frac{l_{mk}}{2} \qquad y_2 = w^{\pm}_{l,mk} + \frac{w^{\pm}_{l}}{2} - \frac{w_{mk}}{2}$$

$$x_3 = l^{\pm}_{l,mk} + \frac{l^{\pm}_{l}}{2} + \frac{l_{mk}}{2} \qquad y_3 = w^{\pm}_{l,mk} + \frac{w^{\pm}_{l}}{2} + \frac{w_{mk}}{2}$$

$$x_4 = l^{\pm}_{l,mk} - \frac{l^{\pm}_{l}}{2} + \frac{l_{mk}}{2} \qquad y_4 = w^{\pm}_{l,mk} - \frac{w^{\pm}_{l}}{2} + \frac{w_{mk}}{2}$$

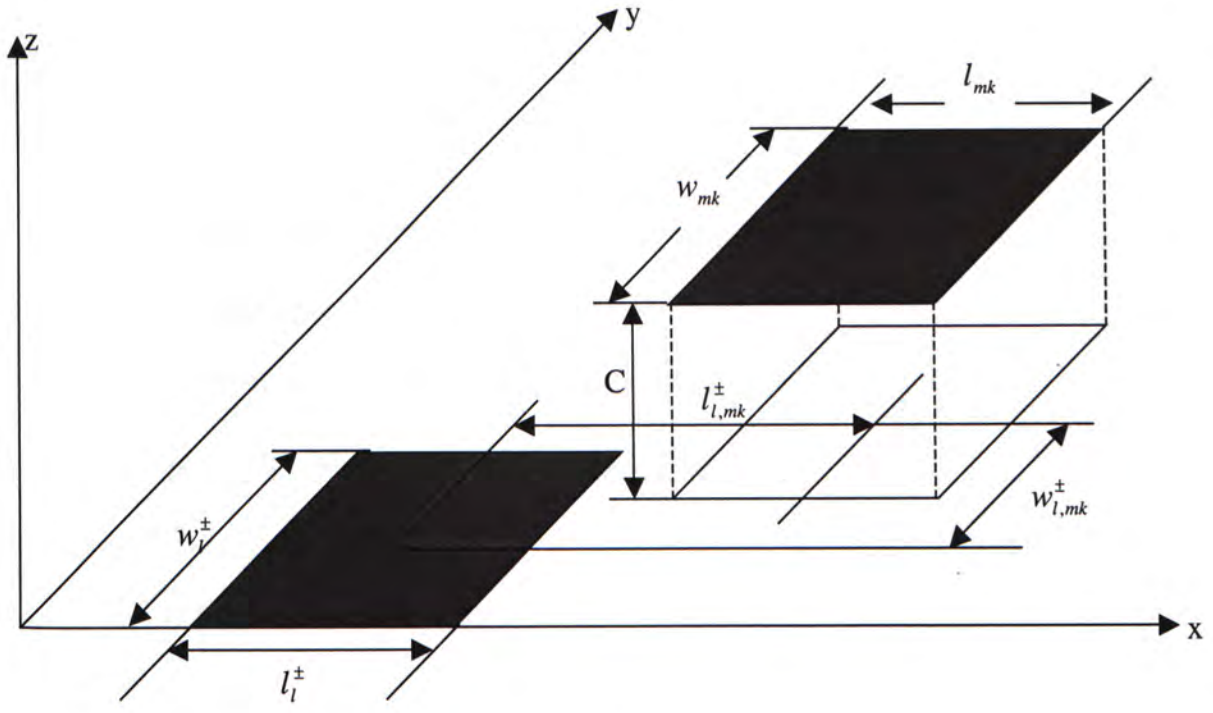

Fig. 2-4 Two parallel thin capacitive cells

The self-capacitance can be calculated by setting $l_l^{\pm} = l_{mk}$, $w_l^{\pm} = w_{mk}$ and $C = l_{l,mk}^{\pm} = w_{l,mk}^{\pm} = 0$ in equation (3-41). It has a very similar form as equation (3-30) except that it is calculated by dividing the 4-D integration by the areas of the surface cells instead of the cross-section widths.

2.5. Meshing Scheme

To present how the inductive and capacitive cells are chosen, an example structure, a thin filamental conducting strip, is given in this section to show the discretization principle. The equivalent circuit model will also be provided.

The number of network nodes specified within a conductor determines the size of the cells and, ultimately, the complexity of the networks. So the number of the network nodes should not be

exceedingly large. At the same time, the choice of the inductive cells with locally constant current and the capacitive cells with locally constant charge distribution is uniquely given by the nodes, so the number of the nodes should not be too small either.

Figure 2-5 shows a piece of thin filamental conducting strip in free space. In figure 2-6 (a), the network nodes, capacitive cells (solid line) and inductive cells (dotted line) are shown. Notice that an inductive cell is formed through shifting two adjacent capacitive cells by halves of their sizes according to what has been stated in section 2.4.1. The elements of the equivalent circuits, shown in fig. 2-6 (b), are fully determined by these cells. For the reason of clarity, in fig. 2-6 (b), only the self-inductances and self-capacitances are included.

Fig. 2-5: A thin filamental conducting strip

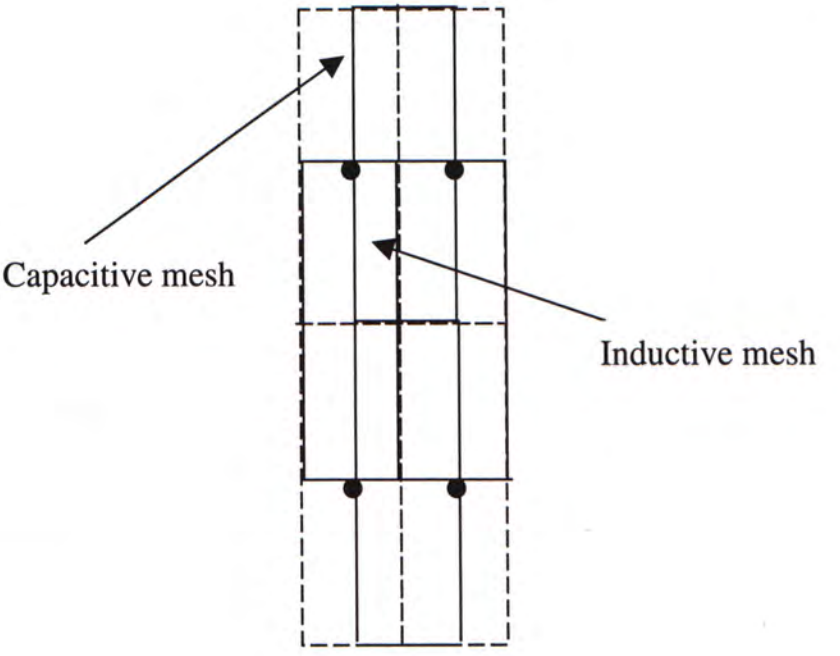

(a)

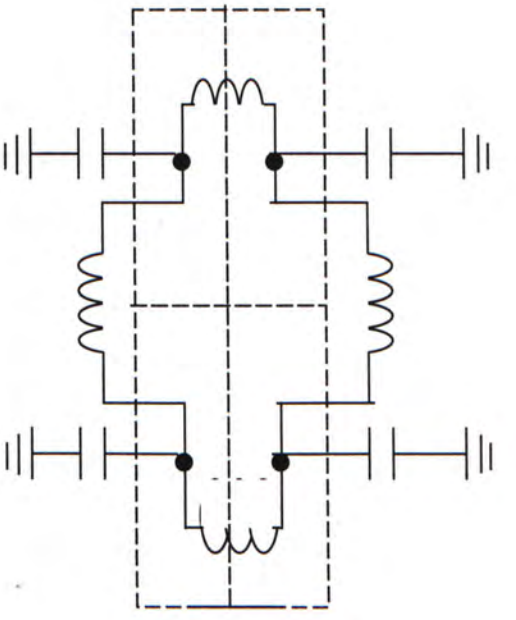

(b)

Fig. 2-6 (a) Inductive and capacitive cells for the discretization of the conductive strip

(b) The equivalent circuit model

The above example of a filamental conductive strip can clearly show how a physical conductive structure can be converted to a network of discrete circuit elements, based on the conversion from the Mixed Potential Integral Equation into a set of coupled equations, namely equation (2-17).

2.6. Green's function

2.6.1 Modification of free space Green's function through Ray-tracing technique

In section 2.3.2 and 2.4.2, to simplify the calculation of the 4-D integration, the free space Green's function is used to get the closed-form mutual inductance and mutual capacitance. However, it is only applicable for the case of conducting cells embedded in a homogeneous substrate of infinite extent, which is rarely the case.

A typical microwave circuit always has one ground on the bottom of the substrate or two grounds on the top and the bottom. Based on these two structures, the ray-tracing technique, shown in figure 2-7, is applied to find the quasi-static Green's function to replace the original static Green's function [7]. In the following sections, for clear description, G_A and G_Φ are used to represent the Green's function for current and charge respectively. When the system has a single ground plane located at the bottom, z=0:

$$G_A(x,y,z)=\frac{1}{\sqrt{\rho^2+(z-z_0)^2}}-\frac{1}{\sqrt{\rho^2+(z+z_0)^2}} \tag{2-42}$$

$$G_\Phi(x,y,z)=\sum_{n=-\infty}^{\infty}(\eta_g\eta_a)^{|n|}\left[\frac{1}{\sqrt{\rho^2+(z-z_n^+)^2}}-\frac{1}{\sqrt{\rho^2+(z-z_n^-)^2}}\right] \tag{2-43}$$

When the system has two ground planes located at the bottom and the top respectively:

$$G_A(x,y,z)=G_\Phi(x,y,z)=\sum_{n=-\infty}^{\infty}(\eta_g\eta_a)^{|n|}\left[\frac{1}{\sqrt{\rho^2+(z-z_n^+)^2}}-\frac{1}{\sqrt{\rho^2+(z-z_n^-)^2}}\right] \tag{2-44}$$

where $\rho=\sqrt{(x-x_0)^2+(y-y_0)^2}$, $z_n^{\pm}=2nh\pm z_0$, $\eta_g=-1$;

$$\eta_a=\begin{cases}\dfrac{\varepsilon_r-1}{\varepsilon_r+1} & \text{One ground plane}\\ -1 & \text{Two ground planes}\end{cases}$$

η_g and η_a are the reflection coefficients for the bottom and top grounds respectively.

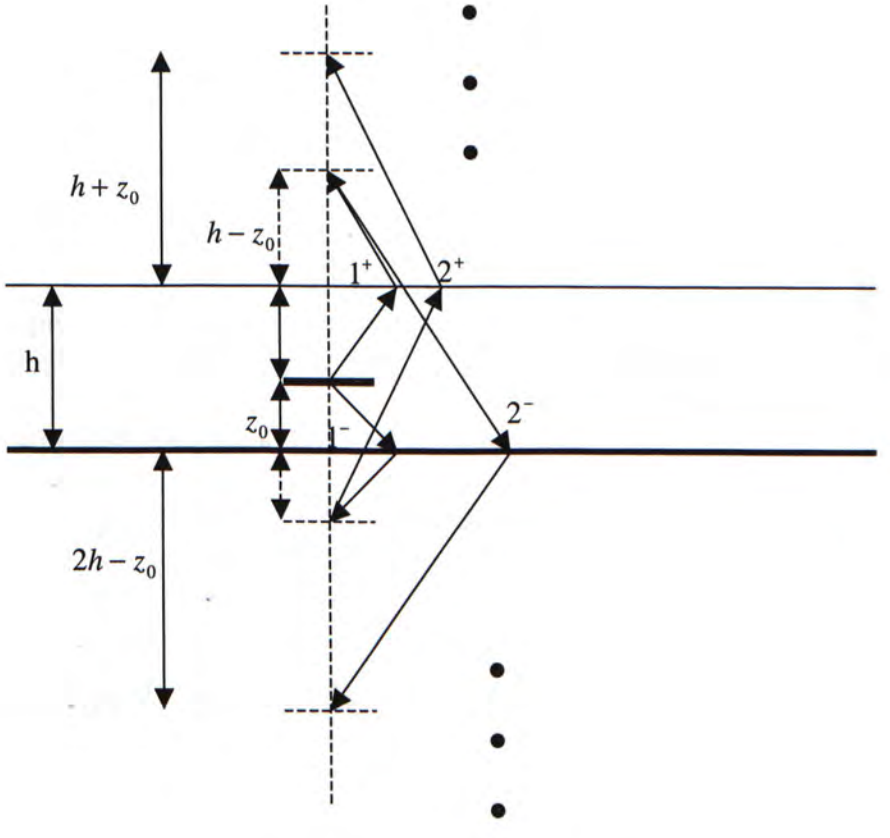

Fig. 2-7 Ray-tracing technique

2.6.2 Impact on partial inductance and partial capacitance

In the previous presentation, equations (2-30) and (2-41) give the formulas to calculate partial inductance and partial capacitance respectively when free space Green's function is adopted. But it has strict limitation on the application environment. So in last section, quasi-static Green's function obtained through the ray-tracing technique is introduced to replace the static Green's function, which will also influence the closed-form formulas to calculate partial inductance and partial capacitance. How to modify the formulas for the partial elements according to the change of the Green's function is the topic of this section.

Firstly the mutual inductance and capacitance are denoted as the functions of the z coordinate of the cells:

$$Lp^{t}_{l,nk} = Lp^{t}(z_l, z_{nk}) \tag{2-45}$$

$$pp^{\pm}_{l,mk} = pp^{\pm}(z_l, z_{mk}) \tag{2-46}$$

where z_l, z_{mk} represent the z coordinates of the inductive/capacitive cells with index l and nk.

For a system with just one ground on the bottom of $z = 0$:

$$Lp^{qs,t}_{l,nk} = Lp^{t}(z_l, z_{nk}) - Lp^{t}(z_l, -z_{nk}) \tag{2-47}$$

$$pp^{qs,\pm}_{l,mk} = \sum_{n=-\infty}^{\infty} (\eta_g \eta_a)^{|n|} \left[pp^{\pm}(z_l, z^{+}_{mk,n}) - pp^{\pm}(z_l, z^{-}_{mk,n}) \right] \tag{2-48}$$

where η_g, η_a and $z^{\pm}_{mk,n}$ have the same definitions as before.

For a system with two grounds on the top and the bottom:

$$Lp_{l,nk}^{qs,t} = \sum_{n=-\infty}^{\infty}\left[Lp^{t}\left(z_l, z_{nk,n}^{+}\right) - Lp^{t}\left(z_l, z_{nk,n}^{-}\right)\right] \tag{2-49}$$

$$pp_{l,mk}^{qs,\pm} = \sum_{n=-\infty}^{\infty}\left[pp^{\pm}\left(z_l, z_{mk,n}^{+}\right) - pp^{\pm}\left(z_l, z_{mk,n}^{-}\right)\right] \tag{2-50}$$

These four equations, in conjunction with equation (2-30) and (2-41), give the closed-form partial inductances and partial capacitances for general microwave circuit, with quasi-static, thin film approximations and rectangular meshing scheme.

2.7. PEEC Modeling of A LTCC 2.4GHz Band Pass Filter

2.7.1 General Procedures to apply PEEC Modeling Method

The fundamental principles behind the PEEC algorithm and the mathematical formulation on how to convert a field problem into a circuit domain problem have been introduced. Based on the understanding of these introductions, the modeling of microwave circuits through PEEC technique consists of three major steps in general:

1. Divide the given structure with network nodes and build inductive and capacitive cells based on this division.

2. Use equation (2-30), (2-41), (2-47), (2-48), (2-49) and (2-50) to get the partial inductance and partial capacitance of the equivalent circuit.

3. Solve the equivalent circuit by a conventional circuit solver for the desired type of solution.

During the modeling, quasi-static approximation is made to avoid time-consuming full-wave solution. Quasi-static approximation is applicable when the overall dimensions of the circuit are much smaller than the operating wavelength, that is, the quasi-static solution is a low-frequency approximation to the full-wave solution. Another approximation is the thin film approximation, which is applicable for the structures, in which the metal thickness is so small compared with the dielectric layer thickness that it can be neglected.

Under such approximations, in conjunction with rectangular meshing scheme, a set of formulation in closed form is available for partial inductance and capacitance calculation. So compared with numerical methods that solve Sommerfeld integration in a full-wave solution, PEEC modeling method has a significant improvement on the simulation speed. On the other hand, equivalent circuit model is another important product of PEEC modeling. With the help of an accurate and simplified equivalent circuit model, we can better understand the electrical behavior of the original field problem under analysis, thus the efficiency of the design and optimization of the circuit layout is greatly improved, which will be introduced in next chapter through a design example.

2.7.2 Numerical Results of a LTCC Band Pass Filter Modeling

A typical embedded structure, a compact band pass filter, implemented with Low Temperature Co-fired Ceramic (LTCC) technology, shown in figure 2-8 (a), is built in this section. The filter is built using LTCC substrate with dielectric constant of 7.8. A total of six 3.6mils thick dielectric layers are used. The buried conductor thickness is 0.47mils, which is about one eighth of the dielectric layer thickness. So the thin film approximation is expected to be well suited for PEEC modeling of this band pass filter.

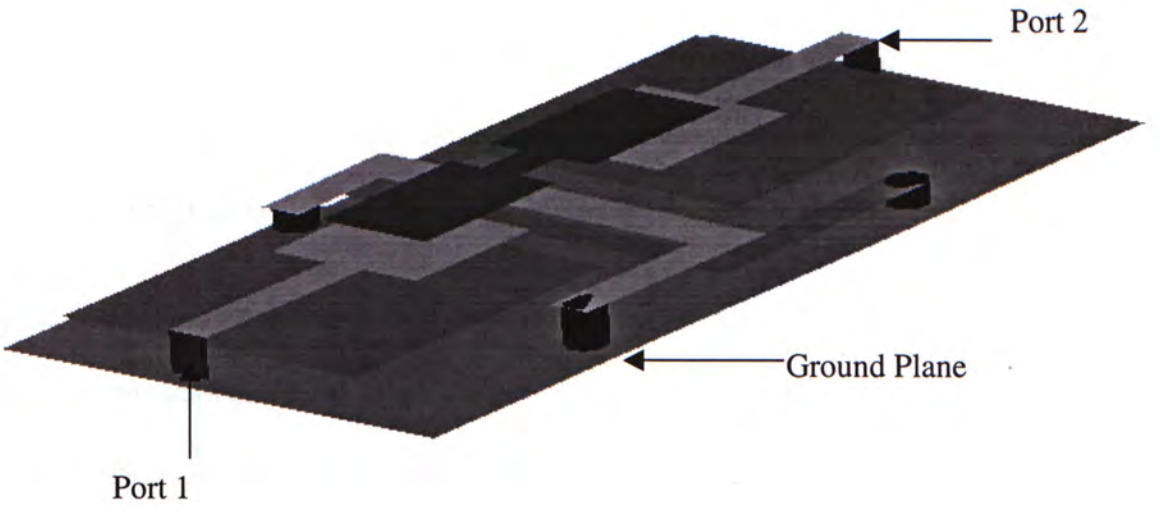

(a)

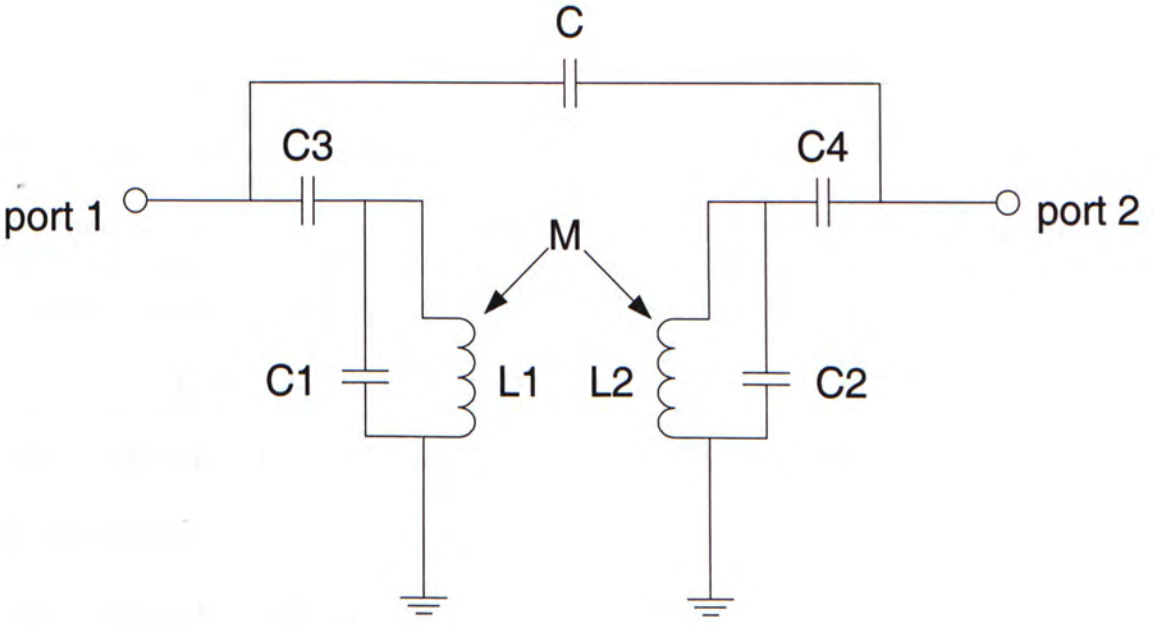

(b)

Fig. 2-8 :(a) 3-D layout of the LTCC Band Pass Filter

(b) Schematic Circuit of the Filter

As shown in the schematic circuit, figure 2-8 (b), this filter consists of five capacitors and two inductors, all of which are built by rectangular strips and patches. So the rectangular descretization scheme will be well suited; the filter is designed to be operating at 2.4GHz, and it is not a very high frequency for quasi- static approximation being applied.

At the same time, a commercially available full-wave circuit EM solver, HFSS, is also used to do the EM simulation. HFSS is an electromagnetic, finite-element simulation tool for high-frequency design of Ansoft Corporation, Pittsburgh, PA, which is now being widely used in MMIC, RFIC and microwave/millimeter-wave circuit designs. The simulation results got from PEEC modeling, HFSS and measurement are compared, as shown in figure 2-9, to quantitatively validate the accuracy and efficiency of the PEEC algorithm. Generally speaking, they show a good agreement with each other.

Consider the two transmission zeros at 1.84-GHz and 3.15-GHz respectively, the simulation by PEEC is quite accurate since the result got from PEEC is nearly the same as that got from HFSS and measurement, while the two frequency responses in the pass band have slight difference, which may be caused by different reasons, such as the quasi-static approximation, the substrate loss not considered in PEEC, the thin-film approximation and the supposed locally constant current and charge, etc. But considering that PEEC is just a coarse model of the original band pass filter, its result has been very satisfactory. After all, the basic information of a band pass filter, the cut-off frequencies, the insertion loss, has been accurately modeled through PEEC. The detailed meshing information and the dimensions of this band pass filter can be found in [7]. There are some techniques introduced in [7] to improve the simulation accuracy of PEEC approach based on this specified example of band pass filter.

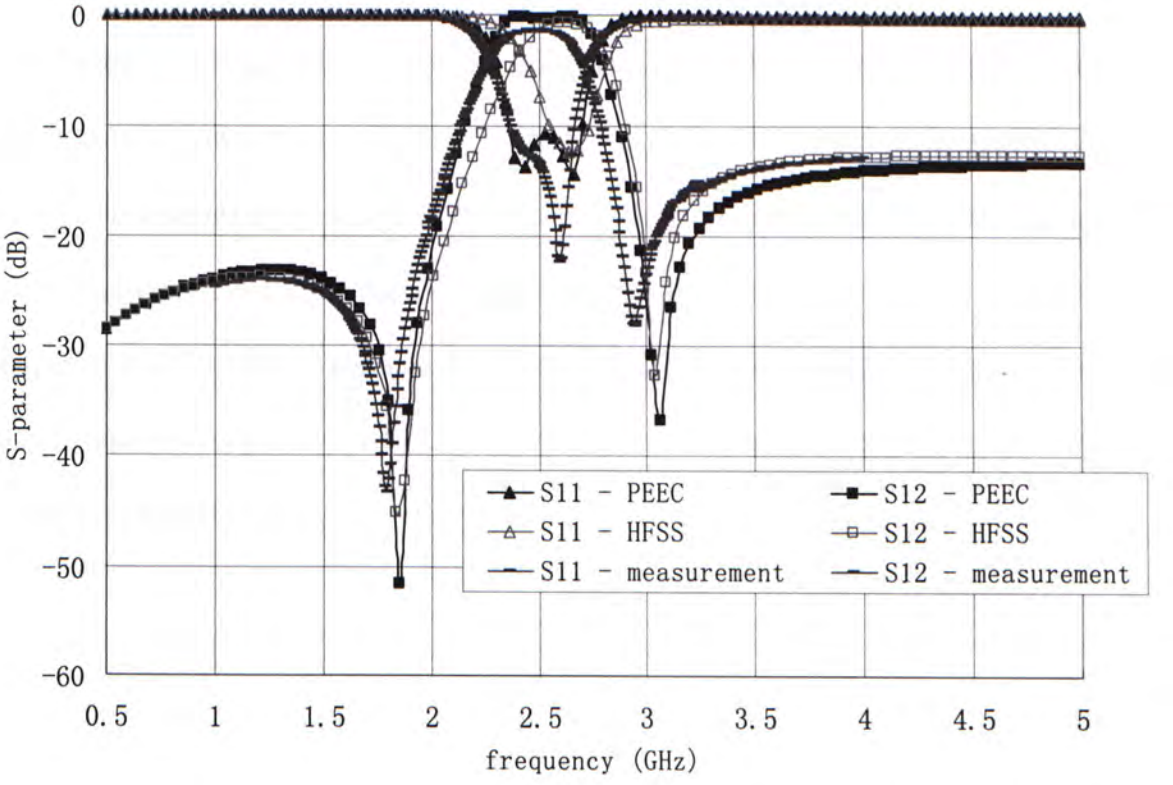

Fig. 2-9 Numerical Results of the Band Pass Filter from PEEC, HFSS and Measurement

2.8. Summary

In this chapter, the basic principle and the mathematical formulation for PEEC modeling are presented first. Then a LTCC band pass filter is built to validate the algorithm. In this modeling method, three approximations are made. The first one is the representation of the conductor by a network of rectangular cells. Intuitively it limits the general application of PEEC algorithm to non-rectangular geometries. The generalization of PEEC approach to model irregular structures will be addressed in the next chapter. The second approximation is quasi-static approximation. A simple ray-tracing technique is used to find the quasi-static Green's function for microstrip

problems from the static one, which leads to straightforward modifications to the closed-form solutions of the partial elements. It agrees well with the full wave solution when the frequency is low, for example, lower than 5 GHz. In chapter four, full-wave technique is applied to replace quasi-static approximation to model radiation and high-frequency problems. The relationship and agreement between quasi-static approximation and the full-wave solution will be given through the mathematical derivation. The last one is the thin film approximation. When the metal layer thickness cannot be neglected compared to the substrate layer thickness, a modification on the PEEC algorithm can be made, the detailed introduction of the modification is given in [7].

3

Generalized PEEC Modeling For Passive Component Of Irregular Shapes

3.1. Introduction

Conventional PEEC algorithm, including the principles and mathematical formulation, has been presented in details in previous chapter. Due to the approximations made in the conventional algorithm, there are some limitations in its application conditions. To generalize the application of the algorithm, this and next chapters propose some new methods to break some of its limits.

One of the approximations introduced in chapter two is to model the structures under analysis with rectangular meshes and assume the direction of current flow to be along the length of each mesh. This approximation is quite reasonable since this algorithm was originally developed to model interconnects and packaging structures for signal integrity analysis purposes. Since most of the interconnect structures are always thin and long, the longitudinal filament discretization and the filamental current flow are well suitable. But with the popularity of Systems-on-Chip (SoCs) in VLSI, the system achieves more reliability and complexity. As a result, more and more irregularly shaped conductors, such as circular spiral inductors, appear. The ability to analyze the circuits of non-rectangular shapes that are embedded in a multi-layered medium allows for more versatile designs with higher density. But the classical rectangular meshing scheme is no longer

suitable since it will cause considerable errors in the representation of a non-rectangular shaped conductor, such as a circle or a hexagonal, with rectangular meshes. It is the purpose of this chapter to generalize the conventional PEEC approach to model irregular geometries.

3.2. Triangular meshing scheme in MoM

3.2.1 Triangular meshing scheme adopted in MoM

In the Method of Moment (MoM) technique, to solve irregular structure modeling problem, the surface of the conductor is modeled in terms of triangular patches and especially designed basis function defined on a pair of adjacent triangles is adopted, which will yield a surface current representation free of line or point charges at sub-domain boundaries The scheme was originally developed by S.M.Rao, Wilton and Glisson [8], [9], [10]. More recently, Schaubert, Wilton and Glisson [11] extended this procedure to volume integral equations for penetrable bodies, which are modeled in terms of tetrahedral elements. Similar with MoM, this triangular meshing scheme was introduced into PEEC in some earlier works [12], [13] to generalize the conventional PEEC method to model irregular geometries, mainly non-orthogonal polygons.

In the generalized approach in [12], [13], triangular meshes are used to represent arbitrarily shaped conductors. Common edges between two adjacent triangles are used to define RWG basis function, which is given in equation 3-1. It defines current flows from one triangle (+) across the common edge to the other (-) one. A piecewise constant basis function, given in equation 3-2, is defined for the charge density q.

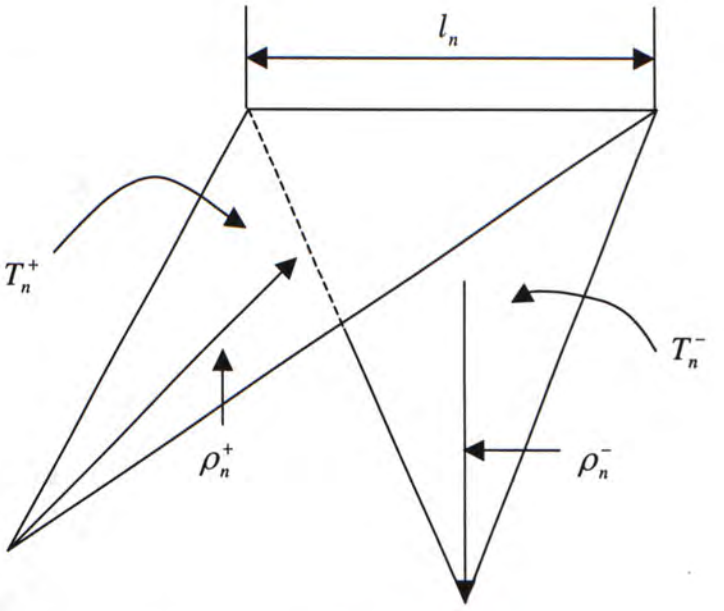

Fig. 3-1 Definition of triangle basis function

$$f_n(\mathbf{r}) = \begin{cases} \dfrac{l_n}{2A_n^+}\rho_n^+ & \text{When } \mathbf{r} \text{ is in } T_n^+ \\ \dfrac{l_n}{2A_n^-}\rho_n^- & \text{When } \mathbf{r} \text{ is in } T_n^- \\ 0 & \text{Elsewhere} \end{cases} \tag{3-1}$$

$$P_n(\mathbf{r}) = \begin{cases} 1 & \mathbf{r} \in nth \text{ Triangle} \\ 0 & \mathbf{r} \in \text{Elsewhere} \end{cases} \tag{3-2}$$

The triangular basis function describes the vector surface current, matches the boundary conditions with no normal components along the boundary edges, and has the potential to represent non-planar current flow. The unknown current distribution on non-orthogonal polygons can be modeled accurately with triangular basis function. An example of such a structure and

suggested meshing scheme are shown in figure 3-2. For clarity, only inductive meshes and corresponding current flow directions are shown.

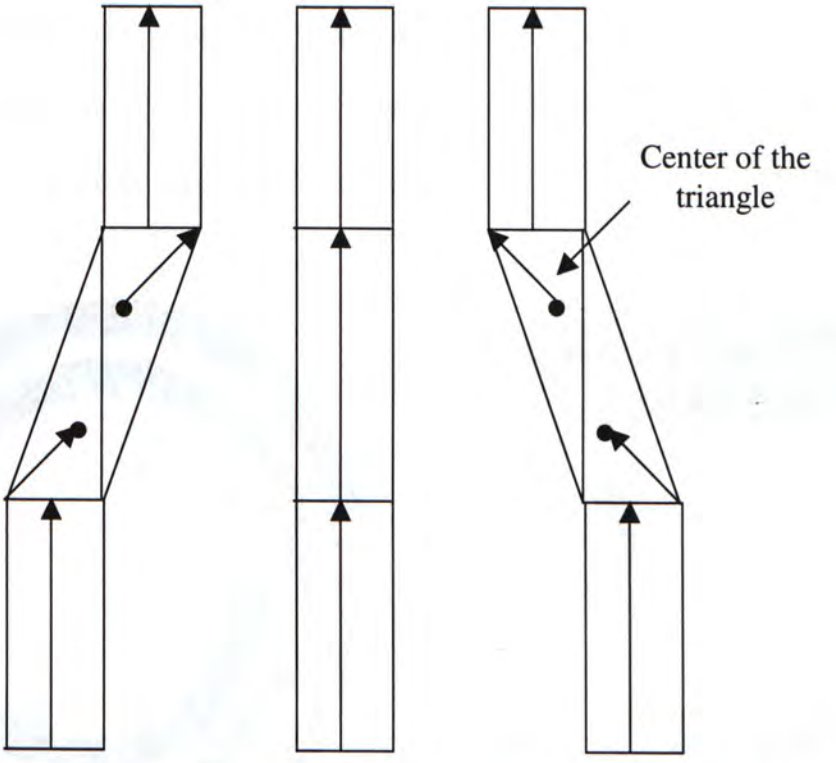

Figure 3-2. An example of a structure containing both rectangles and non-orthogonal polygons and the mixed rectangular and triangular meshing scheme

3.2.2 Spiral Inductor

Besides non-orthogonal polygons, there is another kind of widely used irregular geometries, that is, curved structure. One typical example is spiral inductor. There are many kinds of spiral inductors, such as square, octagon and circular ones. With loss in the spiral-coil metals and the substrate, the capacitive coupling effects to the substrate, spiral inductors always behave quite differently with ideal inductor models. Successful design and simulation of the whole system rely greatly on accurate characterization of the electrical behavior of spiral inductors.

The spirals are usually designed for a maximum quality factor (Q) at the desired operating frequency, in combination with the desired inductance value and available substrate floor space. It has been shown in [14] that for the same inner dimension, the Q of a circular spiral, as figure 3-3 (a), will be about 10% higher than that of a square spiral, as figure 3-3 (b), although the inductance is significantly less (about 20%). So it is worthwhile to study how to accurately model a circular spiral inductor through PEEC approach.

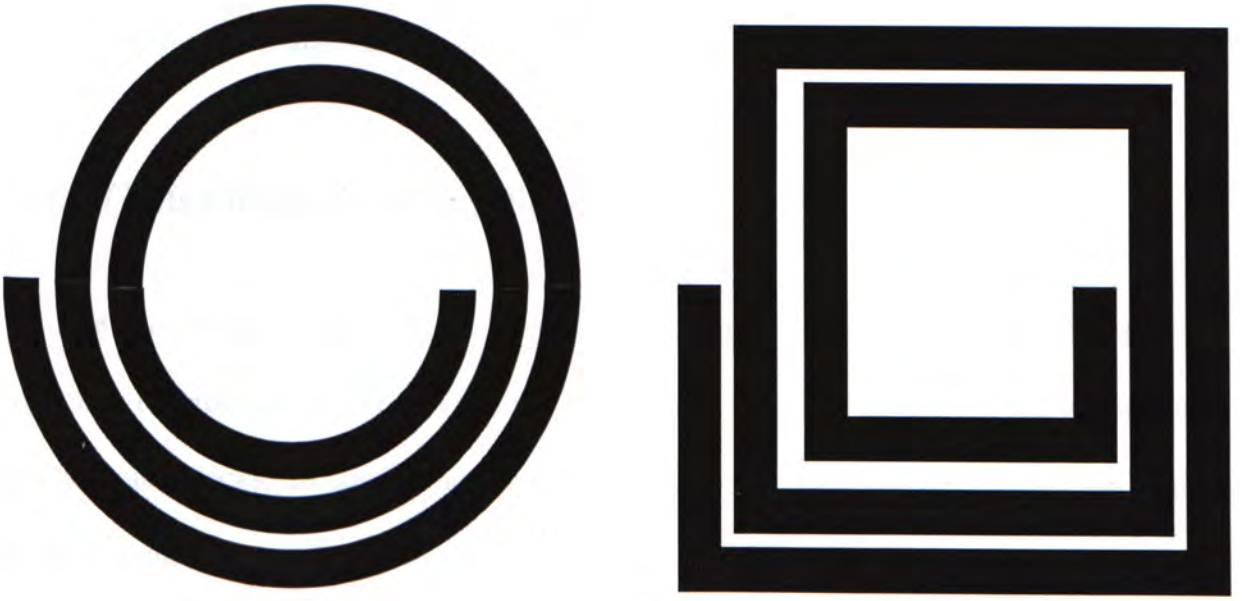

(a) (b)

Fig. 3-3. Two kinds of spiral inductor:

(a): circular spiral inductor; (b): rectangular spiral inductor

Conventional rectangular meshing scheme models the circular conductor surface with rectangles, and the current flow is assumed to be a uniform longitudinal one; while triangular meshing scheme models the circular conductor with pairs of triangular patches, and supposes the current on each pair of triangles to be along the direction defined in figure 3-1. So it is intuitive to find that neither conventional rectangular meshing scheme nor triangular meshing scheme is

suitable for modeling such circular spiral inductors. And also, there is some difference between the basic theories of PEEC and MoM. In MoM, the final objective is to get the current and charge densities from the full-system matrix. While in PEEC, the current and charge densities are supposed to be known, local constant parameters. Instead, partial inductance and partial capacitance coefficients are the two unknowns to be solved directly from MPIE. So instead of triangular meshing scheme together with RWG basis function and rectangular meshing scheme with pulse basis function, in this chapter, a combined rectangular and annular meshing scheme, together with a generalized directional pulse basis function, is proposed.

3.3. Generalized Meshing Scheme

Since the enhancement of PEEC algorithm is aimed at generalizing its application to the modeling of irregular structures, especially those mixed rectangular and curved geometries, two fundamental blocks, rectangle and annular sector, are adopted for discretizing the conductor instead of just rectangular meshes in conventional algorithm. Figure 3-4 shows two exemplary capacitive meshes. There can be many other forms of capacitive meshes in practical applications, for example, the rectangle can be y-directional and the annular sector can vary from 90° to 270° etc. Since inductive meshes are formed through shifting two adjacent capacitive cells by halves of their sizes, there are three possibilities for an inductive mesh, as shown in figure 3-5. Case (a) is generated from two rectangular capacitive meshes; case (b) corresponds to a rectangular capacitive mesh and an annular one, and case (c) is formed when the two adjacent capacitive meshes are both annular sectors. After the discussion of the mesh shapes, we will focus on the definition of the current flow direction on the inductive mesh.

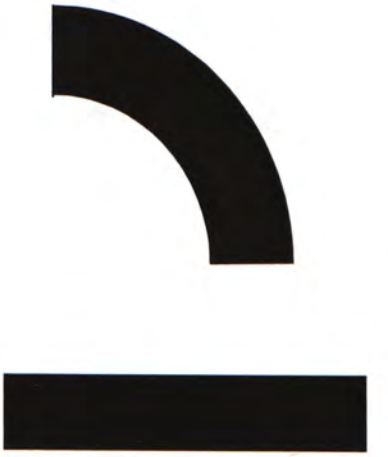

Figure 3-4 Two Types of Capacitive Meshes:

A rectangle and an annular sector

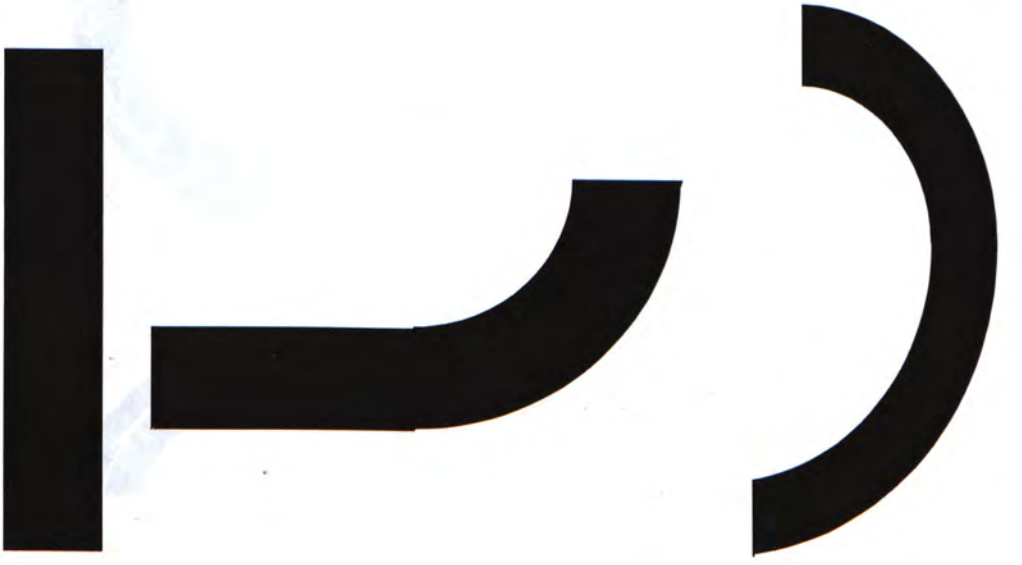

(a) **(b)** **(c)**

Figure 3-5 Three Types of inductive meshes

It is instinctive to define the current flow direction to be +x/+y on a rectangle, and the anticlockwise direction, $+\hat{\phi}$ on an annular sector, respectively. But for the inductive mesh of case (b) in figure 3-5, there are four exceptions, listed in figure 3-6. To keep consistency with the current directions on the other rectangular meshes, the current direction on the rectangular part must be +x or +y. But this definition will conflict with that defined on the annular part of the same mesh. To solve this problem, the direction of the annular part of such an inductive mesh must be modified to be the opposite, $-\hat{\phi}$. The solid and dotted lines represent the current directions before and after modification respectively.

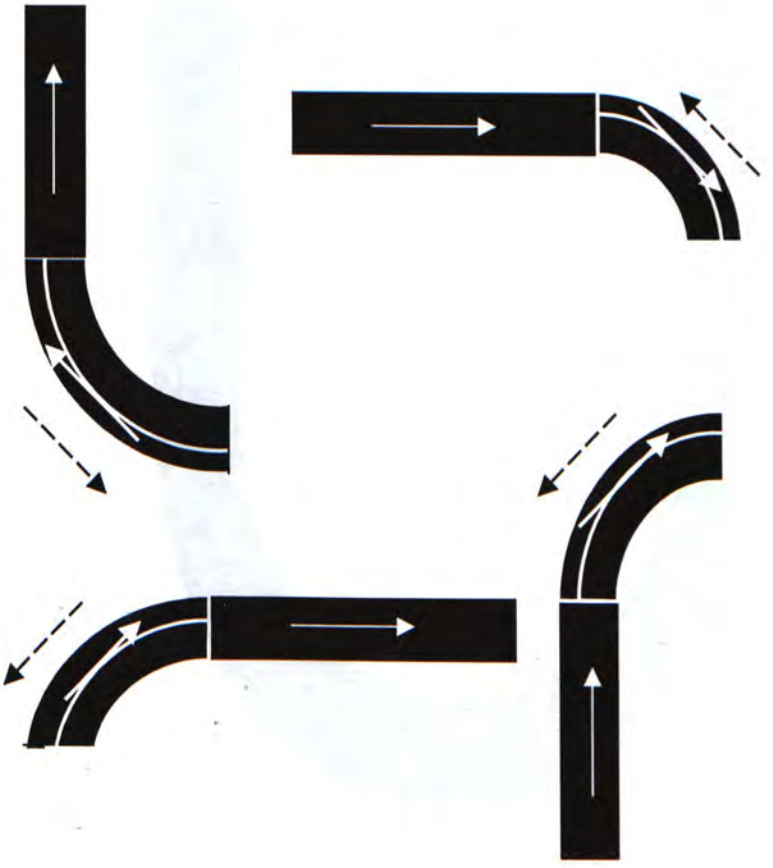

Fig. 3-6: Four Special case for current direction definition

Following is a very simple mixed rectangular and annular example, U-shaped conductor, to show the new meshing scheme. Figure 3-4 shows a piece of thin U-shaped conductor in free space. Figure 3-5 (a) shows a set of network nodes, capacitive cells (solid line) and inductive cells (dotted line). The elements of the equivalent circuits are given in figure 3-5 (b). For clarity, in figure 3-5 (b), only the self-inductances and self-capacitances are included. The detailed introduction on how to generate the inductive and capacitive meshes and how to define the current flow directions on the inductive meshes in irregular geometries will be given in more details in next section.

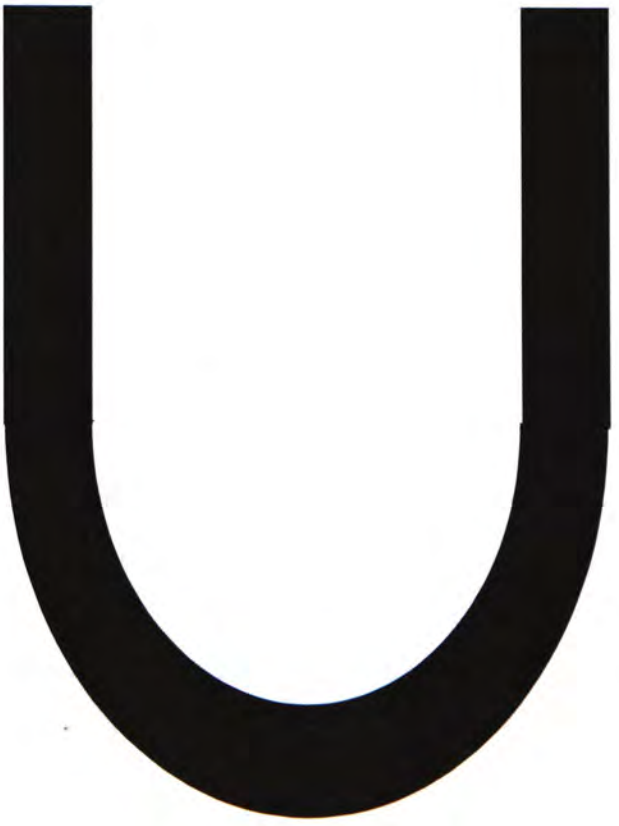

Fig. 3-4: A thin U-shaped conductor

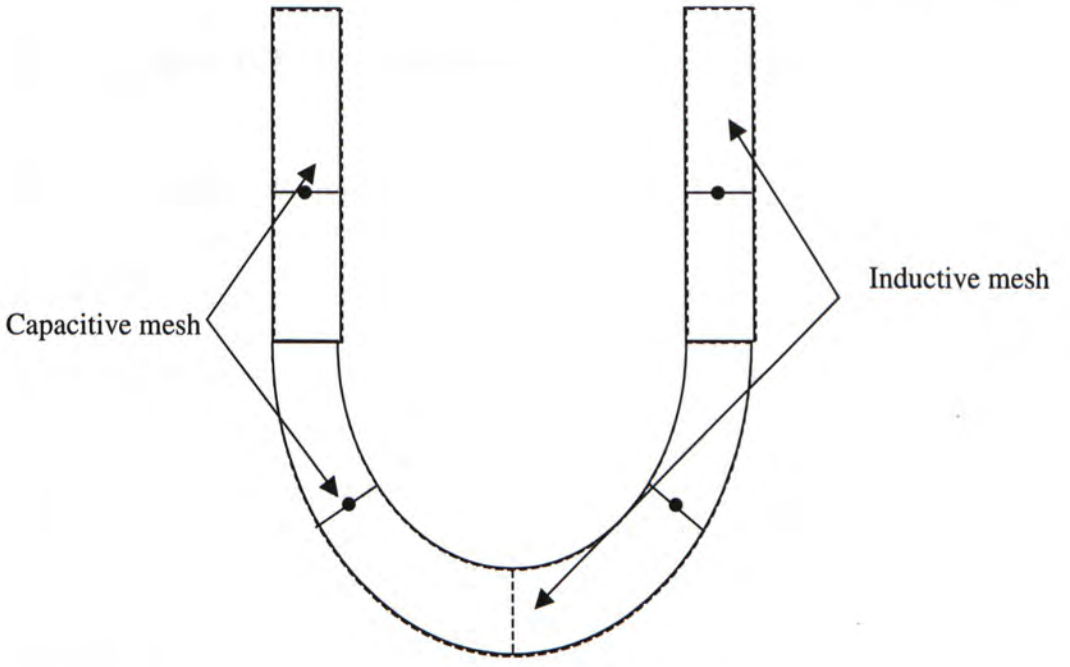

(a)

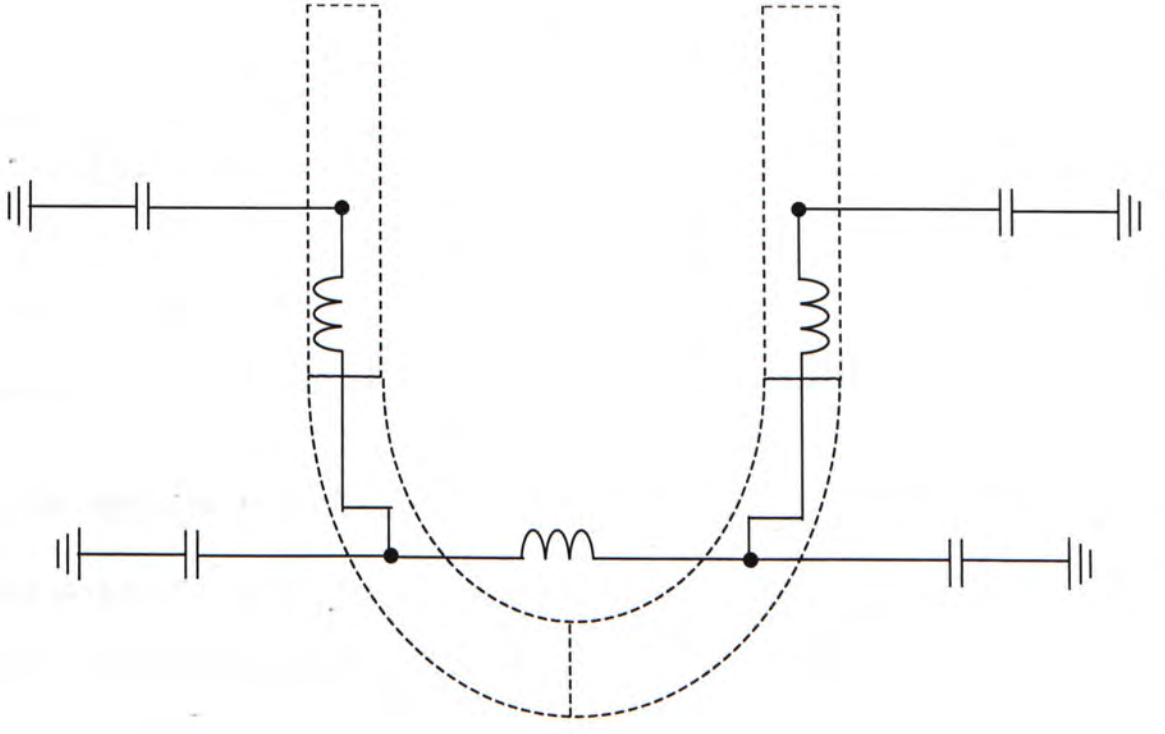

(b)

Fig. 3-5 (a) Inductive and capacitive cells for the discretization of the conductor

(b) The equivalent circuit model

3.4. Mathematical Formulation for Enhanced PEEC

3.4.1 Current and Charge discretization

In enhanced PEEC, the starting point of the derivation is still MPIE, equation (2-8). A circular volume cell is defined by an anticlockwise directional pulse function:

$$\vec{P}_n^{\phi}(\mathbf{r}) = \begin{cases} \vec{\varphi} & \mathbf{r} \in nth \text{ volume circular cell for J} \\ 0 & \mathbf{r} \in \text{elsewhere} \end{cases} \tag{3-3}$$

Using the new basis function, equation 3-3, together with the pulse function defined in chapter two, equation 2-10, the current density is then expanded as:

$$\mathbf{J}(\mathbf{r},t) = \begin{cases} \sum_{n=1}^{N_r} J_n(t) P_n^{\gamma}(\mathbf{r})\hat{\gamma} & \mathbf{r} \in \text{ the inductive cell of rectangle} \\ \sum_{n=1}^{N_c} J_n(t) \vec{P}_n^{\phi}(\mathbf{r}) & \mathbf{r} \in \text{ the inductive cell of annular sector} \end{cases} \tag{3-4}$$

in which, N_r and N_c are the total number of rectangular and annular inductive meshes respectively.

On the other hand, the pulse function for the charge density, $p_m(\mathbf{r})$, has the same form as that defined in chapter 2. So the charge density in the enhanced algorithm still has the same form as equation 2-14. The only difference is that the capacitive cells include both rectangles and annular sectors now while the conventional ones are all rectangles.

Based on the generalized meshing scheme, MPIE turns to be a different form for modeling irregular structures compared with the conventional counterpart, equation 2-15:

$$\frac{J^{\gamma}(\mathbf{r},t)}{\sigma}+\sum_{k=1}^{K}\sum_{n=1}^{N_r}\frac{\mu}{4\pi}\left[\int_{v_{nk}}G(\mathbf{r},\mathbf{r}')dv'_{nk}\right]\frac{\partial J^{\gamma}_{nk}(t')}{\partial t}$$
$$+\sum_{k=1}^{K}\sum_{m=1}^{M}\frac{1}{4\pi\varepsilon}\frac{\partial}{\partial\gamma}\left[q_{mk}(t')\int_{s_{mk}}G(\mathbf{r},\mathbf{r}')ds'_{mk}\right]=E^{i}_{\gamma}(\mathbf{r},t)$$

When $\mathbf{r}\in$ a surface rectangular cell

$$\frac{J^{\varphi}(\mathbf{r},t)}{\sigma}+\sum_{k=1}^{K}\sum_{n=1}^{N_c}\frac{\mu}{4\pi}\left[\int_{v_{nk}}G(\mathbf{r},\mathbf{r}')dv'_{nk}\right]\frac{\partial J^{\varphi}_{nk}(t')}{\partial t}$$
$$+\sum_{k=1}^{K}\sum_{m=1}^{M}\frac{1}{4\pi\varepsilon}\frac{\partial}{\partial\varphi}\left[q_{mk}(t')\int_{s_{mk}}G(\mathbf{r},\mathbf{r}')ds'_{mk}\right]=E^{i}_{\varphi}(\mathbf{r},t)$$

When $\mathbf{r}\in$ a surface annular sector cell

(3-5)

Apply Galerkin matching:

$$\frac{1}{a_l\sigma}\int_{v_l}J^{\gamma}(\mathbf{r},t)dv_l+\sum_{k=1}^{K}\sum_{n=1}^{N_r}\frac{\mu}{4\pi}\frac{1}{a_l}\left[\int_{v_l}\int_{v_{nk}}G(\mathbf{r},\mathbf{r}')dv'_{nk}dv_l\right]\frac{\partial J^{\gamma}_{nk}(t')}{\partial t}$$
$$+\sum_{k=1}^{K}\sum_{m=1}^{M}\frac{1}{4\pi\varepsilon}\frac{1}{a_l}\int_{v_l}\frac{\partial}{\partial\gamma}\left[q_{mk}(t')\int_{s_k}G(\mathbf{r},\mathbf{r}')ds'_k\right]dv_l=\left\langle E^{i}_{\gamma}(\mathbf{r},t),\frac{P^{\gamma}_l}{a_l}\right\rangle$$

when $\mathbf{r}\in$ a rectangular cell and $\mathbf{r}'\in$ a rectangular cell too

$$\frac{1}{a_l\sigma}\int_{v_l}J^{\gamma}(\mathbf{r},t)dv_l\hat{\gamma}\bullet\hat{\varphi}+\sum_{k=1}^{K}\sum_{n=1}^{N_r}\frac{\mu}{4\pi}\frac{1}{a_l}\left[\int_{v_l}\int_{v_{nk}}G(\mathbf{r},\mathbf{r}')dv'_{nk}dv_l\right]\frac{\partial J^{\gamma}_{nk}(t')}{\partial t}\hat{\gamma}\bullet\hat{\varphi}$$
$$+\sum_{k=1}^{K}\sum_{m=1}^{M}\frac{1}{4\pi\varepsilon}\frac{1}{a_l}\int_{v_l}\frac{\partial}{\partial\gamma}\left[q_{mk}(t')\int_{s_k}G(\mathbf{r},\mathbf{r}')ds'_k\right]dv_l\hat{\gamma}\bullet\hat{\varphi}=\left\langle E^{i}_{\gamma}(\mathbf{r},t),\frac{\vec{P}^{\hat{\varphi}}_l}{a_l}\right\rangle$$

when $\mathbf{r}\in$ a cell of rectangle and $\mathbf{r}'\in$ a cell of annular sector, and vice versa.

$$\frac{1}{a_l\sigma}\int_{v_l} J^{\varphi}(\mathbf{r},t)dv_l\hat{\varphi}_l \bullet \hat{\varphi}_{nk} + \sum_{k=1}^{K}\sum_{n=1}^{N}\frac{\mu}{4\pi}\frac{1}{a_l}\left[\int_{v_l}\int_{v_{nk}} G(\mathbf{r},\mathbf{r}')dv'_{nk}dv_l\right]\frac{\partial J^{\varphi}_{nk}(t')}{\partial t}\hat{\varphi}_l \bullet \hat{\varphi}_{nk}$$

$$+\sum_{k=1}^{K}\sum_{m=1}^{M}\frac{1}{4\pi\varepsilon}\frac{1}{a_l}\int_{v_l}\frac{\partial}{\partial\varphi}\left[q_{mk}(t')\int_{s_k} G(\mathbf{r},\mathbf{r}')ds'_k\right]dv_l\hat{\varphi}_l \bullet \hat{\varphi}_{nk} = \left\langle E^i_{\gamma}(\mathbf{r},t), \frac{\vec{P}^{\hat{\varphi}}_l}{a_l}\right\rangle$$

when $\mathbf{r}\in$ a cell of annular sector and $\mathbf{r}'\in$ a cell of annular sector

(3-6)

3.4.2 Enhanced Formulation for partial mutual inductance and capacitance

The second terms in all of the three equations of (3-6), are related with the inductive portion of the final circuit model.

Take the two rectangular cells as an example:

$$Lp_{l,nk} = \frac{\mu}{4\pi}\frac{1}{a_l a_{nk}}\left[\int_{S_l}\int_{S_{nk}}\frac{1}{|\mathbf{r}-\mathbf{r}'|}dv'_{nk}dv_l\right] \tag{3-7}$$

Since the thin film approximation is made in PEEC, the dimension of the edge in the rectangle, along which the current flows, can be cancelled. The cell volumes v_l, v_{nk} turn to be cell surface areas S_l, S_{nk} and the cross-sectional areas a_l, a_{nk} change into the cross-sectional lengths w_l, w_{nk}. Equation (3-7) changes into:

$$Lp_{l,nk} = \frac{\mu}{4\pi}\frac{1}{w_l w_{nk}}\left[\int_{S_l}\int_{S_{nk}}\frac{1}{|\mathbf{r}-\mathbf{r}'|}ds'_{nk}ds_l\right] \tag{3-8}$$

Corresponding to the three possibilities of inductive meshes, three sets of formulation to calculate the partial inductance in newly enhanced PEEC are given below:

$$Lp_{l,nk} = \frac{\mu}{4\pi}\frac{1}{w_l w_{nk}}\left[\int_{S_l}\int_{S_{nk}}\frac{1}{|\mathbf{r}-\mathbf{r}'|}ds'_{nk}ds_l\right]$$

when $\mathbf{r}\in$ a cell of rectangle and $\mathbf{r}'\in$ a cell of rectangle

$$Lp_{l,nk} = \frac{\mu}{4\pi}\frac{1}{w_l w_{nk}}\left[\int_{S_l}\int_{S_{nk}}\frac{1}{|\mathbf{r}-\mathbf{r}'|}ds'_{nk}ds_l\right]\hat{\gamma}\bullet\hat{\varphi}$$

when $\mathbf{r}\in$ a cell of rectangle and $\mathbf{r}'\in$ a cell of annular sector, and vice versa.

$$Lp_{l,nk} = \frac{\mu}{4\pi}\frac{1}{w_l w_{nk}}\left[\int_{S_l}\int_{S_{nk}}\frac{1}{|\mathbf{r}-\mathbf{r}'|}ds'_{nk}ds_l\right]\hat{\varphi}_l\bullet\hat{\varphi}_{nk}$$

when $\mathbf{r}\in$ a cell of annular sector and $\mathbf{r}'\in$ a cell of annular sector (3-9)

in which, w_l and w_{nk} are the cross sectional lengths of the two edges, perpendicular to the direction of current flow, on the cells with the index l and nk respectively.

The third term in equation (3-6) has similar form as the counterpart in chapter two except for the factor, $\frac{\partial}{\partial a_l}\hat{a}_l\bullet\hat{a}_{nk}$. Here, the parameters are defined as

$$\hat{a}_l(\hat{a}_{nk}) = \begin{cases}\hat{\gamma} & \text{when } l^{th}\ (nk^{th}) \text{ cell is a rectangle}\\ \hat{\varphi} & \text{when } l^{th}\ (nk^{th}) \text{ cell is an annular sector}\end{cases} \quad (3\text{-}10)$$

If some mathematical transformation are made to this factor:

$$\frac{\partial}{\partial a_l}\hat{a}_l\bullet\hat{a}_{nk} = \frac{\partial}{\partial\frac{a_l}{\hat{a}_l\bullet\hat{a}_{nk}}} = \frac{\partial}{\partial b_{l,nk}} \quad (3\text{-}11)$$

in which, $\vec{b}_{l,nk} = \dfrac{a_l}{\hat{a}_l \bullet \hat{a}_{nk}}$, representing the projection of $\vec{a}_l$ to the direction of $\hat{a}_{nk}$. To get the coefficient of potential, similar transformation as that in section 2.4.1 is made, just to change γ into $b_{l,nk}$. Similarly, a closed-form set of formulation can be got. It has the same form as the conventional one, equation (2-38), but in the generalized approach, S_l and S_{mk} may represent the areas of both rectangles and annular sectors.

Free-space Green's function is also adopted here, so this analysis is also applicable only for the case of the cells inside a homogenous region of infinite extent.

3.4.3 Four-Dimensional Integration

Equations (3-9) and (2-38) are the kernels to be solved in calculating the partial inductance and the coefficient of potential in enhanced PEEC algorithm. The key step in the calculation is to solve the four-dimensional integrations:

$$\int_{S_f}\int_{S_s} \frac{\hat{J}_s \bullet \hat{J}_f}{|\mathbf{r}-\mathbf{r}'|} ds_s' ds_f \tag{3-12}$$

$$\int_{S_f}\int_{S_s} \frac{1}{|\mathbf{r}-\mathbf{r}'|} ds_s' ds_f \tag{3-13}$$

Expression (3-12) and (3-13) are the kernel integrations in the inductance and capacitance calculation respectively. S_s and S_f represent the areas of the inductive/capacitive cells on which the source and field point exist; $\hat{J}_s$ and $\hat{J}_f$ represent the unit vectors to indicate the current directions on the source and field inductive cells.

In conventional PEEC, solving these 4-dimensional integrations is relatively simple. Firstly, the integration areas are all rectangles. Secondly, since the current flow direction on any inductive cell is either x or y, $\hat{J}_s \bullet \hat{J}_f$ only has two values: 1 or 0. So analytical results can be got for the two 4-dimensional integrations in conventional PEEC. But with the increasing complexity of mesh shape and current flow direction, analytical forms of the two kernel integrations may be impossible or infeasible. Then it is necessary to find a relatively efficient and still accurate numerical algorithm to solve the 4-D integrations.

3.4.4 Gauss Numerical Integration

There are many numerical methods to solve an integration, duringwhich, Gauss-Legendre method is a simple, efficient and accurate choice for solving non-adaptive numerical integration of arbitrary function. Gauss integration method is explained in detail in [15]. The basic idea is to compute the rate at positions in the total integration interval area as representative as possible. The formula for Gauss numerical integration is given :

$$\int_a^b f(x)dx = \frac{b-a}{2}\int_{-1}^{1} f\left(\frac{b-a}{2}\xi + \frac{b+a}{2}\right)d\xi \cong \frac{b-a}{2}\sum_{k=1}^{n} w(\xi_k) f\left(\frac{b-a}{2}\xi + \frac{b+a}{2}\right) \tag{3-14}$$

in which $w_k = w(\xi_k)$ is the weight, $x_k = \frac{b-a}{2}\xi + \frac{b+a}{2}$ is the abscissa. The table of abscissas and weights up to n =96 can be found in [16].

To validate the accuracy of the numerical method applied to solve the 4-D integrations, (3-12) and (3-13), an example of a simple 4-D integration, given in equation (3-15), is verified. Its integration area is a rectangle, shown in figure 3-6, so that this 4-D integration can be solved

analytically as a reference. And also it is solved by Gauss numerical integration method. Since the integrand of this 4-D integration is the same as the integrand in equation (3-13), the comparison of the two results can reflect the accuracy of the Gauss method in solving the 4-D integrations in the enhanced PEEC approach.

$$y = \int_{S_s}\int_{S_f} \frac{1}{r} dsds' \tag{3-15}$$

in which $r = \sqrt{(x_s - x_f)^2 + (y_s - y_f)^2}$, which is the distance between the source and field points. (x_s, y_s) and (x_f, y_f) have the same definition as the last section.

Since the integration area is a rectangle, the integration can be solved analytically:

$$\int_{S_s}\int_{S_f} \frac{1}{r} dsds' = \sum_{i=1}^{4}\sum_{j=1}^{4} (y(j)^2 \bullet x(i) \bullet \log(x(i) + \sqrt{x(i)^2 + y(j)^2})/2 + x(i)^2 \bullet y(j) \bullet \log(y(j) + \sqrt{x(i)^2 + y(j)^2})/2) - \sqrt{(x(i)^2 + y(j)^2)^3}/6) \tag{3-16}$$

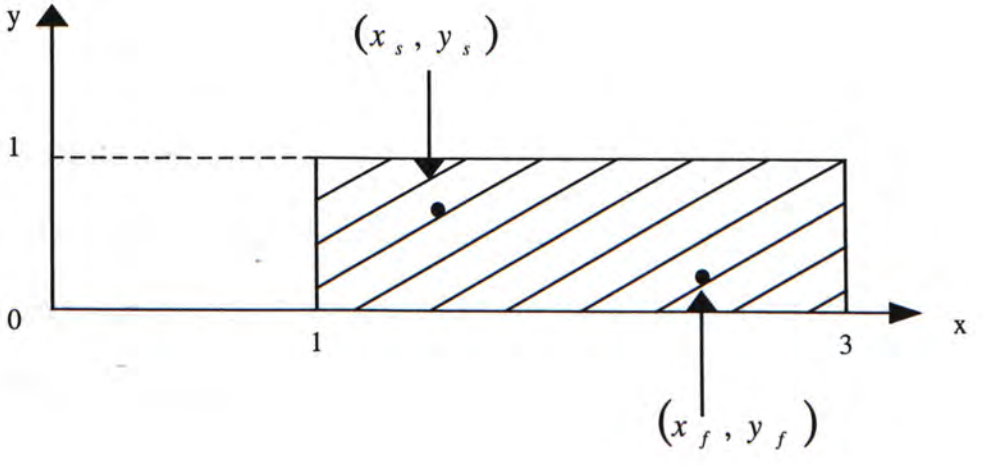

Figure 3-6: 4-D Integration area: an example geometry of a rectangle

On the other hand, Gauss numerical method is used. But at first, x and x' are regarded to be the integration variables, the integration is solved analytically in these two dimensions. The closed-form formula is given:

$$\int_{S_s}\int_{S_f}\frac{1}{r}dsds' = \sum_{i=1}^{2}\sum_{j=1}^{2}\left((-1)^{i+j}\left(\sqrt{(x_2(j)-x_1(i))^2+(y_2-y_1)^2}-\right.\right.$$
$$\left.\left.(x_2(j)-x_1(i))\bullet\log\left((x_2(j)-x_1(i))+\sqrt{(x_2(j)-x_1(i))^2+(y_2-y_1)^2}\right)\right)\right) \quad (3\text{-}17)$$

Then apply Gauss-Legendre method to solve the integration over the remained two dimensions of y and y'. These two parameters both vary from 0 to 1. Since this is a 2-D numerical integration, there should be two numbers of points for Gauss numerical integration over y and y' respectively to be chosen, M and N. In our program, to simplify the problem, $M = N - 3$ is supposed. Based on the number of weights and abscissas available in [16], M is set to be a parameter varying from 1 to 30. The integration error function can be defined as equation (3-18), which is plotted as figure 3-7.

$$error = \frac{y_{Gauss} - y_{analytic}}{y_{analytic}} \quad (3\text{-}18)$$

From this figure, we can know when N = 6 (M=3), the absolute error will be approximately 0.02(2%), which has been quite accurate for our use to solve the 4-D kernel integrations. Since this integrand in equation (3-15) is the same as that in the two 4-D integrations, (3-9) and (2-38), in PEEC, the four numbers of points in Gauss numerical integration are chosen to be 6, 6, 3 and 3 at first. But this combination will cause the integrand $\frac{1}{r}$ to be singular, so the set of four numbers

is adjusted to be 6, 6, 4 and 4. With the increase of the sampling number, the accuracy should be still a little lower than 2%.

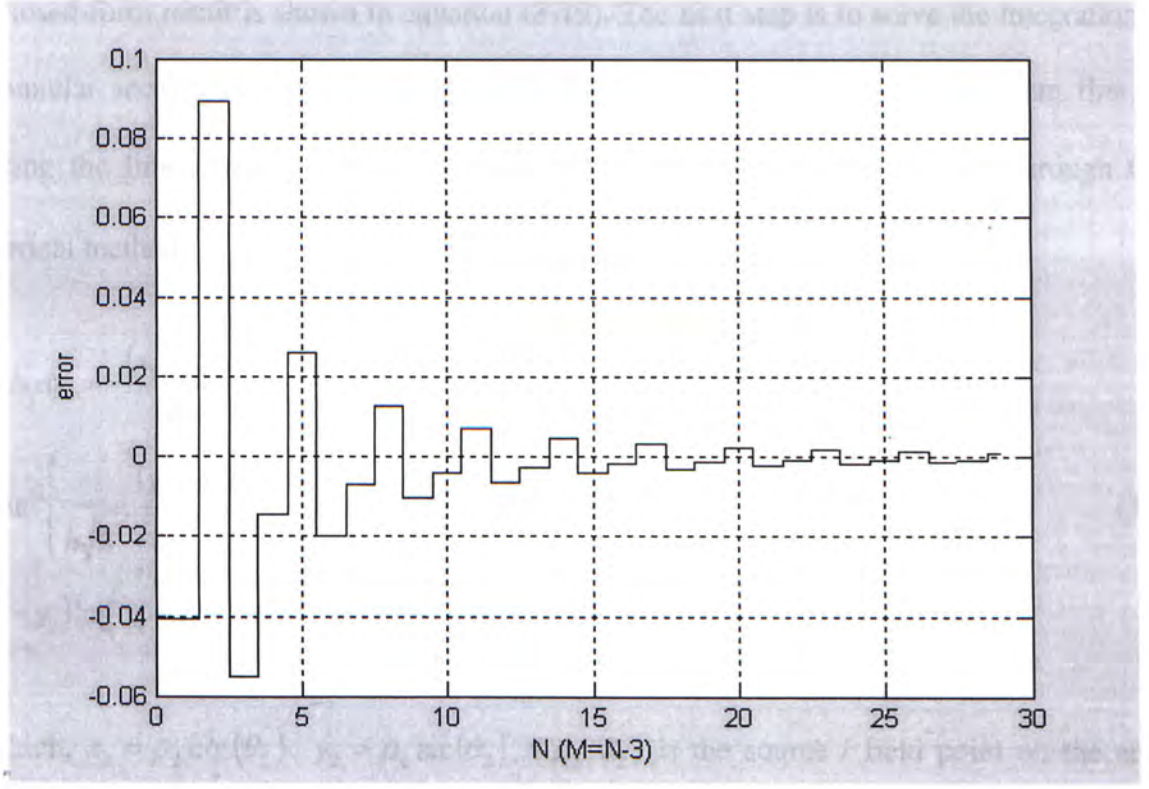

Figure 3-7 Error function of the Gausian numerical integration method

3.4.5 Mixed Numerical and Analytical Technique

After the introduction of the Gauss numerical integration method, the 4-D integrations for partial inductance and capacitance calculation will be solved in different ways for different cases. Consider equation (3-9) first, the solution is divided into three cases:

1. Both the source and field meshes are rectangles:

This case is in fact the same as that considered in conventional PEEC, the formulation is given in (2-30), (2-47) and (2-49).

2. The source and field meshes are respectively, a rectangle and an annular sector, or vise versa:

The 4-D integration is integrated analytically on the rectangle, that is, in x_1 and y_1 dimensions, the closed-form result is shown in equation (3-19). The next step is to solve the integration over the annular sector part. Change equation (3-19) into cylindrical coordinate system first, then utilizing the limits of ρ_2 and θ_2, this 2-D integration is solved numerically through Gauss numerical method.

$$\begin{aligned}\iint_r \frac{1}{r} dx_1 dy_1 = &-\frac{(x_1-x_2)}{2}\frac{h^2-(x_1-x_2)^2}{h^2+(x_1-x_2)^2}-(y_1-y_2)+h\tan^{-1}\left(\frac{y_1-y_2}{h}\right)\\ &-h\tan^{-1}\left(\frac{(x_1-x_2)(y_1-y_2)}{h\sqrt{h^2+(x_1-x_2)^2+(y_1-y_2)^2}}\right)+(x_1-x_2)\log\left(y_1-y_2+\sqrt{h^2+(x_1-x_2)^2+(y_1-y_2)^2}\right)\\ &+(y_1-y_2)\log\left(x_1-x_2+\sqrt{h^2+(x_1-x_2)^2+(y_1-y_2)^2}\right)\end{aligned} \tag{3-19}$$

in which, $x_2 = \rho_2\cos(\theta_2)$, $y_2 = \rho_2\sin(\theta_2)$, (ρ_2, θ_2) is the source / field point on the annular sector in cylindrical coordinate system.

3. Both the source mesh and field mesh are annular sectors:

Cylindrical coordinate system is built first, the 4-D integration can be integrated analytically in ρ_1 direction, as shown in equation (3-20). Then the remained 3-D integration problem $(\rho_2, \theta_1, \theta_2)$ can be solved numerically by Gaussian integration method.

$$\begin{aligned}&\int_{r_1}\frac{1}{|\vec{r}_1-\vec{r}_2|}dr_1 = r_2\sqrt{\text{var}}+\\ &r_2\bullet(r_0\cos(\theta_0-\theta_1)+r_2\cos(\theta_1-\theta_2))\bullet\\ &\log(r_1-(r_0\cos(\theta_0-\theta_1)+r_2\cos(\theta_1-\theta_2))+\sqrt{\text{var}})\end{aligned} \tag{3-20}$$

in which, $\text{var} = h^2 + r_0^2 + r_1^2 + r_2^2$

After analyzing the solution to equation (3-9) to calculate the partial coefficient of potential, following is how to solve equation (2-38) to get the partial inductance. There are three kinds of inductive mesh, as shown in figure 3-5, so there are totally 6 cases to consider: a&a, a&b, a&c, b&b, b&c, c&c.

1. The two inductive meshes are both of type a:

This has been considered in conventional PEEC. Please refer to equation (2-30).

2. The other five cases:

The principle for the other five cases is the same, so only one of them, the two inductive meshes are of type a and type b respectively, shown in figure 3-8, is analyzed here as an example to avoid repetition. l^{th} and nk^{th} inductive meshes are both divided into two parts: l_1, l_2 and nk_1, nk_2, called sub-meshes. Since the integration is in fact a summation, the total partial inductance $Lp_{l,nk}$ can be written to be the summation of the four partial inductances between each two sub-meshes:

$$Lp_{l,nk} = Lp_{l1,nk1} + Lp_{l1,nk2} + Lp_{l2,nk1} + Lp_{l2,nk2} \tag{3-21}$$

Consider one of the four terms in the above equation, when the two sub-meshes are rectangle and annular sector respectively, such as $Lp_{l1,nk2}$, the result for 2-D integration of the rectangle, is given in equation (3-19); when the two sub-meshes are both annular sectors, such as $Lp_{nk2,nk2}$, the analytical result for 1-D integration of the partial inductance, is given in equation (3-20). Then Gauss numerical method is applied to solve the integrations in the remained two or three dimensions.

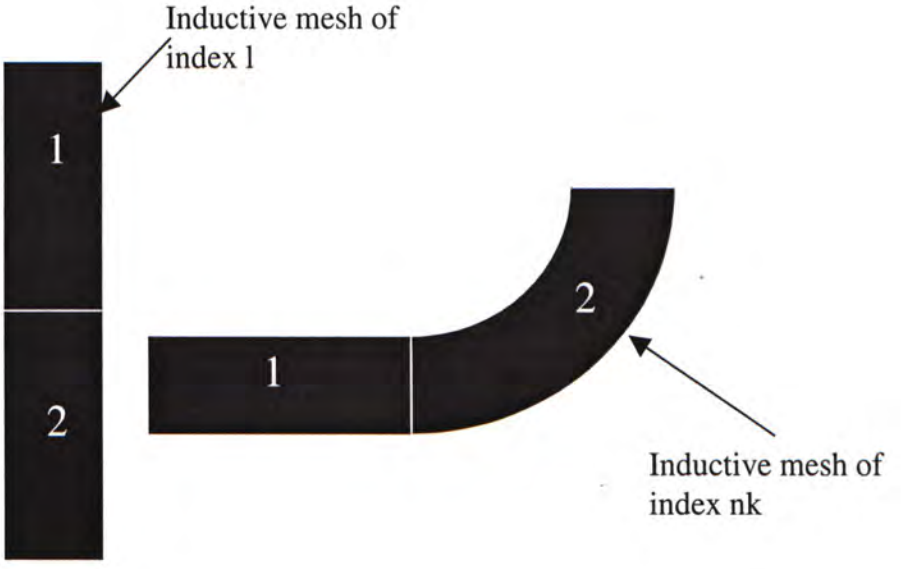

Figure 3-8: The calculation of the inductance between the two inductive meshes of type (a) and (b)

After discussing each possible case in the calculation of the partial inductance *Lp* and the coefficient of potential *pp* in enhanced PEEC algorithm, since the free space Green's function is still adopted, equations (2-47), (2-48), (2-49) and (2-50) are also needed to modify the results. The inverse of the potential coefficient natrix is the matrix of the partial capacitance.

3.5. Numerical Results from Enhanced PEEC Modeling Method

3.5.1 Spiral Inductor

In section 3.2.2, the introduction of the spiral inductor has been given in details. To validate the accuracy and efficiency of enhanced PEEC algorithm, a two-layer circular spiral inductor with

just one ground is built. The inductor is buried in a 440μm substrate with the dielectric constant of 9.1. It has two layers with the height of 239 μm and 317.5 μm respectively, connected with each other through a via-hole. Each dielectric layer has a thickness of 79 μm. On each layer, the inductor is realized by a 1.5-turn circular spiral structure, as shown in figure 3-9 (a), the outer radius is 850 μm, the turn width is 150 μm and the turn space is 100 μm. The buried conductor thickness is 8 μm, which is about one tenth of the dielectric layer thickness, which assures the accuracy of the application of the thin-film approximation.

A large number of meshes are needed if classical rectangular meshing scheme is used to accurately model such a spiral inductor, which will definitely have much influence on both the simulation efficiency and accuracy. Figure 3-9 (b) gives a possible rectangular meshing scheme of the two-layer circular spiral inductor, in which, totally up to 34 rectangular meshes are needed to model it and each of the meshes is labeled in the figure by its index number. In fact, after rectangular discretizaiton, it turns out to be a square spiral inductor instead of a circular one from figure 3-9 (b). So when the conventional rectangular meshing scheme is used to model irregular geometries, there may be great difference between the structure surfaces before and after the discretization. While in enhanced PEEC, this is a different case. To assure the accuracy, the number of meshes per wavelength is set to be 20, which is the same as the setting in chapter two. For this two-layer spiral inductor example:

$$\lambda = \frac{c}{f\sqrt{\varepsilon_r}} \tag{3-22}$$

in which, c is the speed of light, f is the frequency under consideration, which is set to be lower than 5GHz, so the wavelength calculated is greater than 19.9mm. While the perimeter of the two

1.5-turn spirals is less than 0.008mm, which is much less than the wavelength, hence only four meshes are needed in the equivalent circuit. The detailed information of both the conventional and the newly proposed meshing schemes of the two layers of the spiral inductor will be given in appendix A.

The simulation time using enhanced PEEC, conventional PEEC and HFSS is 6 seconds, 1 second, 436 seconds respectively, so either conventional PEEC or enhanced PEEC algorithm is much faster than the full-wave EM solver, HFSS. The improvement on the simulation speed due to the adoption of the quasi-static approximation can be embodied. Enhanced PEEC is slower than the conventional PEEC in the simulation of this example structure since the numerical integration is very time-consuming, comparing with the analytical method. But efficiency is only one factor, and another more important factor is the accuracy of the algorithm.

Because of the existence of the parasitic effect, the spiral inductor may resonate with parasitic capacitances. Since thin-film approximation is used in PEEC model, the distance of the parasitic capacitor is larger, hence the capacitance is smaller, that is, the resonant frequency simulated by PEEC should be a little higher than that got from HFSS. As shown in figure 3-9(c), the simulation result got from conventional PEEC algorithm does have some difference with that got from HFSS but its resonant frequency is lower than the one simulated by HFSS, which is not in coincidence with the analysis from the physical aspect. This is mainly because of the inappropriate representation of the circular structure by rectangular meshes. While enhanced PEEC algorithm overcomes this error by perfectly representing the spiral with two circular meshes and two rectangular meshes. The S-parameter in figure 3-9 (c) shows that the resonant frequency got from enhanced PEEC and HFSS is about 2.71GHz and 2.64GHz respectively, which satisfies the analysis of the resonant frequency from the thin-film approximation.

Considering the parasitic effects and the approximation, the simulation result of the enhanced PEEC agrees well with that of HFSS. Compared with the conventional algorithm, the accuracy of the enhanced PEEC algorithm can be improved especially for the mixed rectangular and annular structure modeling.

Figure 3-9 (d) is the simplified equivalent circuit derived from the PEEC model. Node 1 and 2 are the two nodes standing for the spirals while node 3 and 4 are the two nodes representing the two ports. The values for different partial inductances and partial capacitances are given in table 3-1. L_{12} is the largest, which represents the self-inductance of the inductive mesh generated by halves of the two spirals on different layers. L_{13} and L_{24} represent the self-inductance of the inductive mesh generated by just one half of the spiral and one half of the rectangular mesh, which explains why L_{13} and L_{24} are much less than L_{12}. All the capacitances are generated by parasitic effect, including the capacitance between each capacitive mesh and the ground, such as C_1, C_2, C_3 and C_4, and the capacitance between the partly overlapping capacitive meshes.

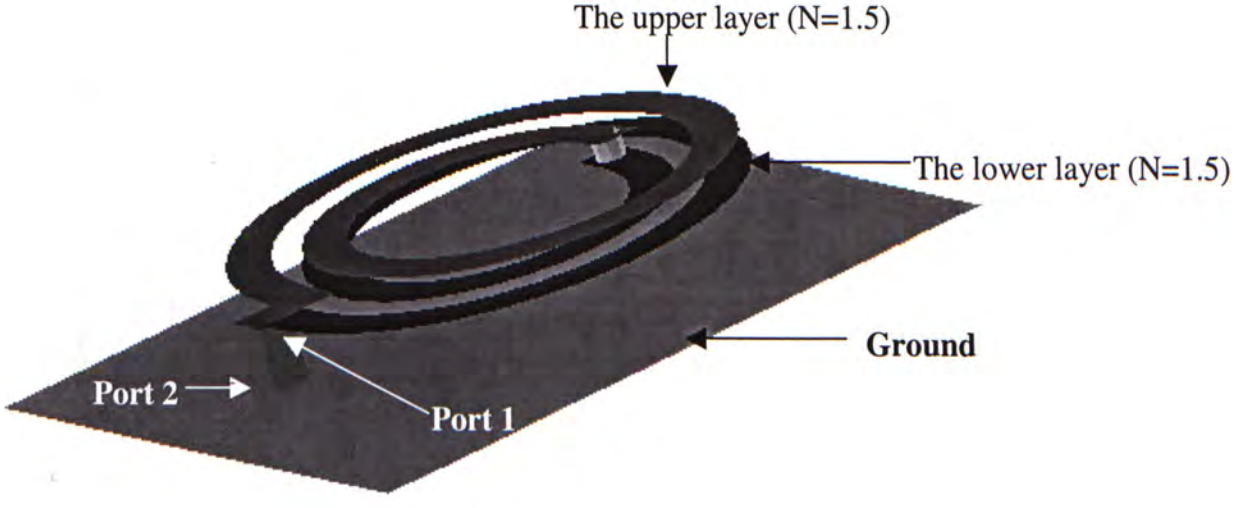

(a)

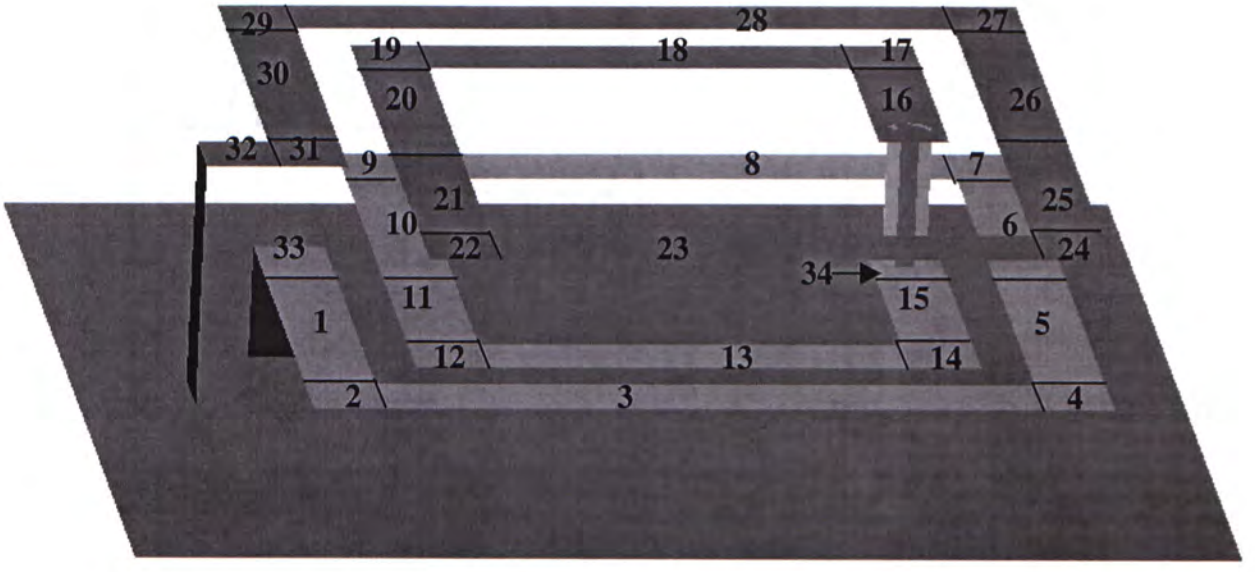
29
28
27
19
18
17
30
20
16
26
32
31
9
8
7
21
25
10
6
33
22
23
24
34
11
15
1
5
12
13
14
2
3
4

(b)

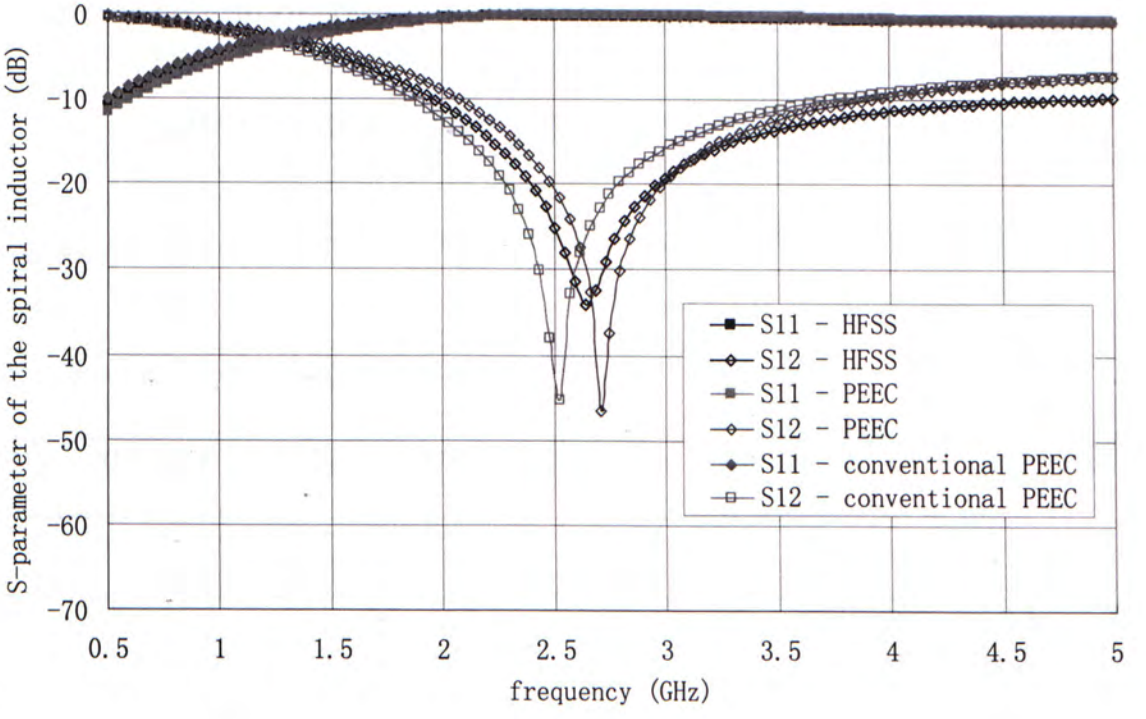
S-parameter of the spiral inductor (dB)
0
-10
-20
-30
-40
-50
-60
-70
0.5
1
1.5
2
2.5
3
3.5
4
4.5
5
frequency (GHz)
S11 - HFSS
S12 - HFSS
S11 - PEEC
S12 - PEEC
S11 - conventional PEEC
S12 - conventional PEEC

(c)

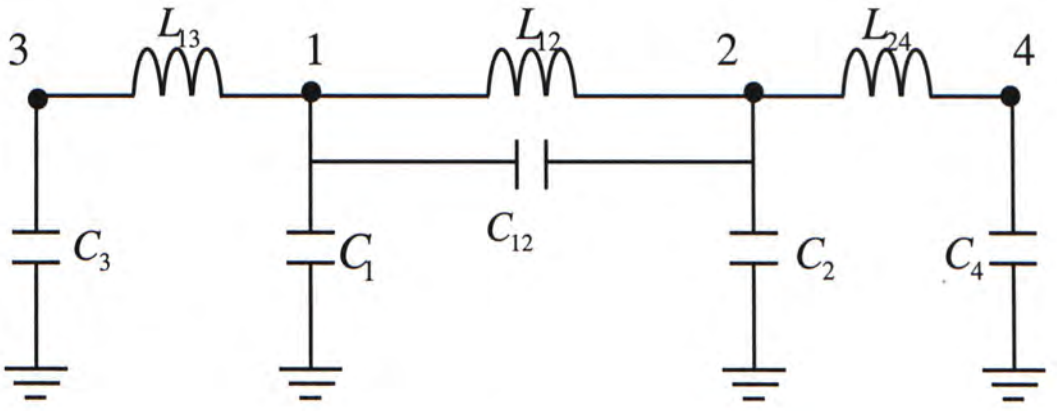

(d)

Figure 3-9: Two-layer Spiral Inductor Simulated by Enhanced PEEC algorithm

(a) Layout of 2-layer circular spiral;

(b) Discretized spiral by rectangular meshing sheme;

(c) Comparison of S-parameter got from DDL and HFSS;

(d) Simplified Equivalent Circuit Model

C_{12}	C_{14}	C_1	C_{23}	C_2	C_{34}	C_3	C_4
0.6010 p	0.0520 p	0.4745 p	0.0312 p	0.2260 p	0.0629 p	0.1824 p	0.2274 p

L_{13}	L_{42}	M		L_{13}	L_{21}	M
0.8159 n	1.6130 n	0.0983 n		0.8159 n	4.7775 n	0.4905 n

Table 3-1: Partial Inductances and Partial Capacitance for figure 3-9 (c)

3.5.2 High Pass Filter

A LTCC high-pass filter is built in this section to verify the generalized algorithm in modeling the two-ground system. The filter is built using the same LTCC substrate as that in the last example with dielectric constant of 9.1. A total of twenty-five 40 μm thick dielectric layers are used. Fig. 3-10(a) shows the physical 3D layout. This high-pass filter will be used in the design example of a LTCC diplexer in the next section, so the detailed information of the layout will be given in the description of the layout of the diplexer in appendix B.

Figure 3-10 (b) gives the schematic model of the high-pass filter. C_1 and L_1 are the fundamental block of a high pass filter; L_{12} is used to resonate with C_1 to decrease S_{11} in the pass band. C_{11} is used to resonate with L_1 to decrease S_{12} in the stop band. C_{12} is used to control the parasitic capacitance in the whole system. Each element is labeled in the layout figure (a).

Fig. 3-10 (c) shows the frequency responses got from enhanced PEEC and HFSS. In HFSS, conductor thickness is not considered either. It is shown that the frequency responses are quite similar except for some slight differences in both the pass band and the stop band. So even in the enhanced PEEC, due to some approximations, such as quasi-static approximation and numerical integration, there will still be some errors introduced. But considering that PEEC is just a coarse model to the structure under analysis, this simulation accuracy has been quite satisfactory since it successfully predicts the performance, even the parasitic effects of the structure.

What's more important, the simulation time of PEEC is only 41s, while it needs 17,290s for HFSS, that is, generalized PEEC model is more than 400 times faster than HFSS for this high-pass filter structure, which is a dramatic improvement on the simulation speed.

Figure 3-10 (d) shows the simplified equivalent circuit model got from PEEC. Compared with (b), the simplified circuit model got from PEEC is more complex than the schematic design since the former contains many parasitic elements. The values for partial capacitances and partial inductances are shown in table 3-2 (a) and (b) respectively. In the table, $L_{35}, C_{34}, L_{62}, C_2$ and C_6 have relatively larger values compared with other elements because they are the counterparts of L_{12}, C_1, L_1, C_{11} and C_{12} in figure 3-10 (b). The remained terms in table (3-2) are all parasitic elements, which won't be contained in figure 3-10 (b).

Generally speaking, PEEC is much faster than full-wave EM solvers since quasi-static approximation avoids time-consuming numerical integration. Secondly, equivalent circuit model can be derived from PEEC method, which can clearly explain the electrical performance of the structure under analysis from circuit domain and easily take the lumped element into consideration too. These two characters of PEEC make it very suitable to be an initial model in the design and optimization of RF passive design, which will be presented in details soon.

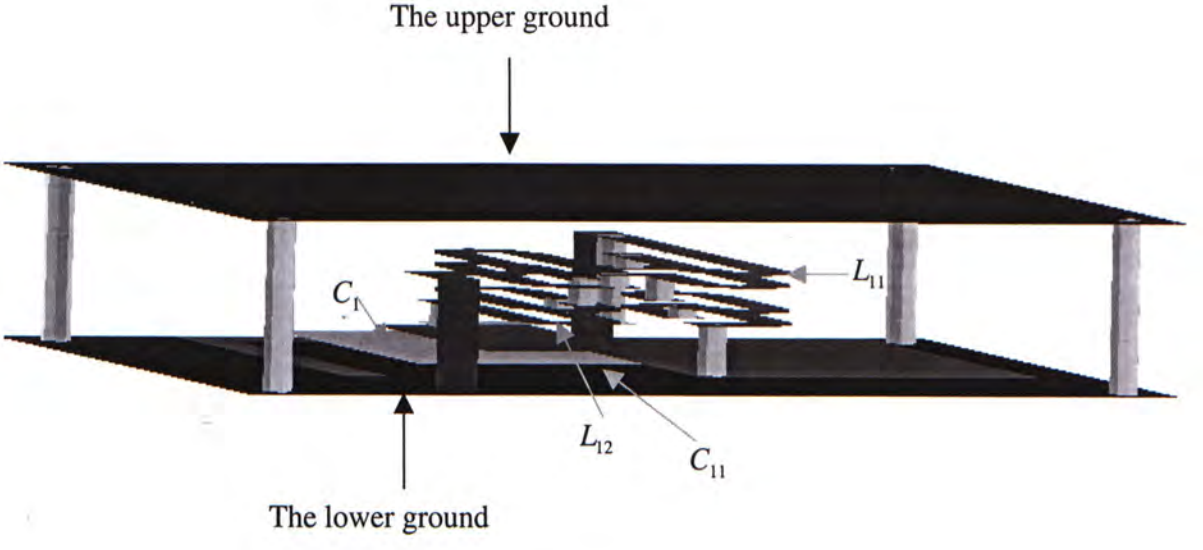

(a) LTCC layout of the multi-layer high pass filter

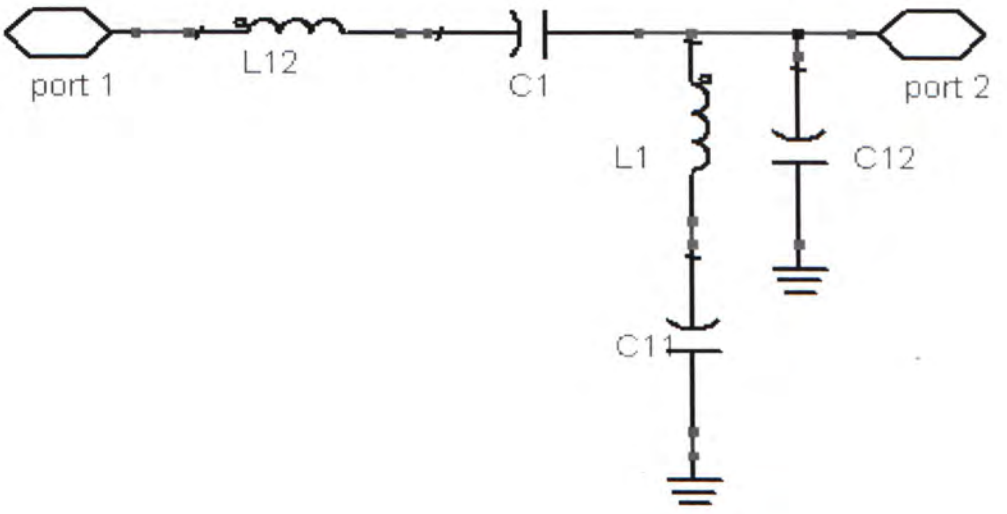

(b) Schematics of the high pass filter

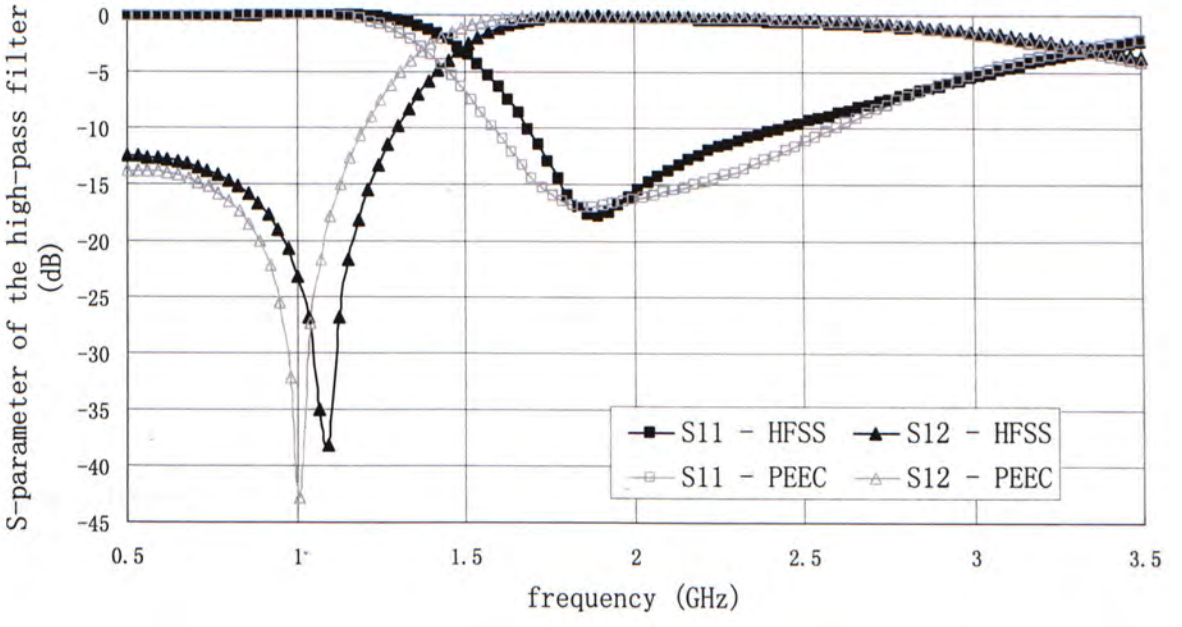

(c) S-parameter figures got from Enhanced HFSS and HFSS

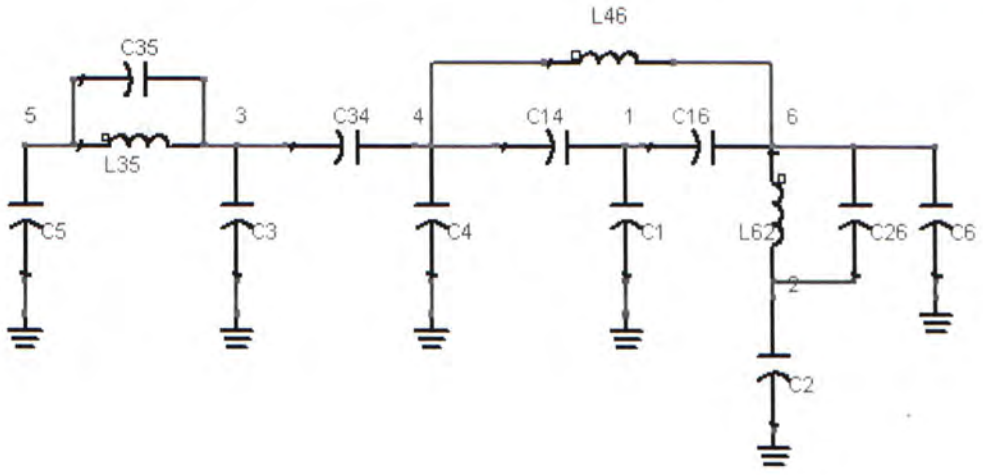

(d) Equivalent Circuit derived in Enhanced PEEC model

Figure 3-10 High Pass Filter Simulated in Enhanced PEEC and HFSS

C_{14}	C_{16}	C_1	C_{24}	C_{26}	C_2
0.0159 p	0.0180 p	0.8597 p	0.0297 p	0.1087 p	4.1490 p
C_{34}	C_{35}	C_3	C_4	C_5	C_6
1.2002 p	0.0993 p	0.0789 p	1.1449 p	0.0736 p	0.1893 p

(a)

L_{35}	L_{46}	L_{26}	L_{12}	L_{46}	$M_{46,12}$	$M_{46,26}$	$M_{12,26}$
5.2232 n	0.4967 n	5.3287 n	0.5452 n	0.4967 n	0.0201 n	0.0480 n	0.0264 n

(b)

Table 3-2(a) Partial Capacitance In the Simplified Equivalent Circuit

(b) Partial Inductance In the Simplified Equivalent Circuit

3.5.3 Design and Optimization of LTCC Diplexer

A general flowchart of LTCC multi-layer RF circuit design and optimization method for given specifications is given in figure 3-11. In this figure, Aggressive space mapping (ASM) algorithm, four steps included, developed by Bandler et al. in 1995 [17], is adopted as an optimization scheme to get an accurate but time-consuming fine EM model from a less accurate but more efficient coarse PEEC model.

First of all, an ideal schematic circuit is designed and optimized to meet with the desired specifications. The model after this optimization is called x_c^*, which is also the initial fine model x_f^1. Realize each inductor and capacitor in x_c^* by calculating its dimensions through empirical formulas [18] then the whole layout is constructed. Full-wave EM solver, such as HFSS, is used to simulate this layout, and the result must be different with the PEEC simulation result since PEEC is just a coarse model. If the HFSS simulation result doesn't satisfy the specifications, curve fit this simulation result by another schematic model, called x_c^1. By Broyden's formula, the second fine model can be got, called x_f^2. These processes are repeated until the fine model satisfies the specifications finally.

In previous section, it has been declared that, compared with full-wave solver, PEEC has two mentionable features, one is its simulation efficiency, which is much higher than HFSS, and the other is the resultant equivalent circuit model, which helps us understand the electrical performance of the structure under analysis more intuitively. It is these two features that serve PEEC well suited to be the coarse model in applying ASM optimization. Next a design example will be given to show how to design and optimize LTCC RF circuit using ASM.

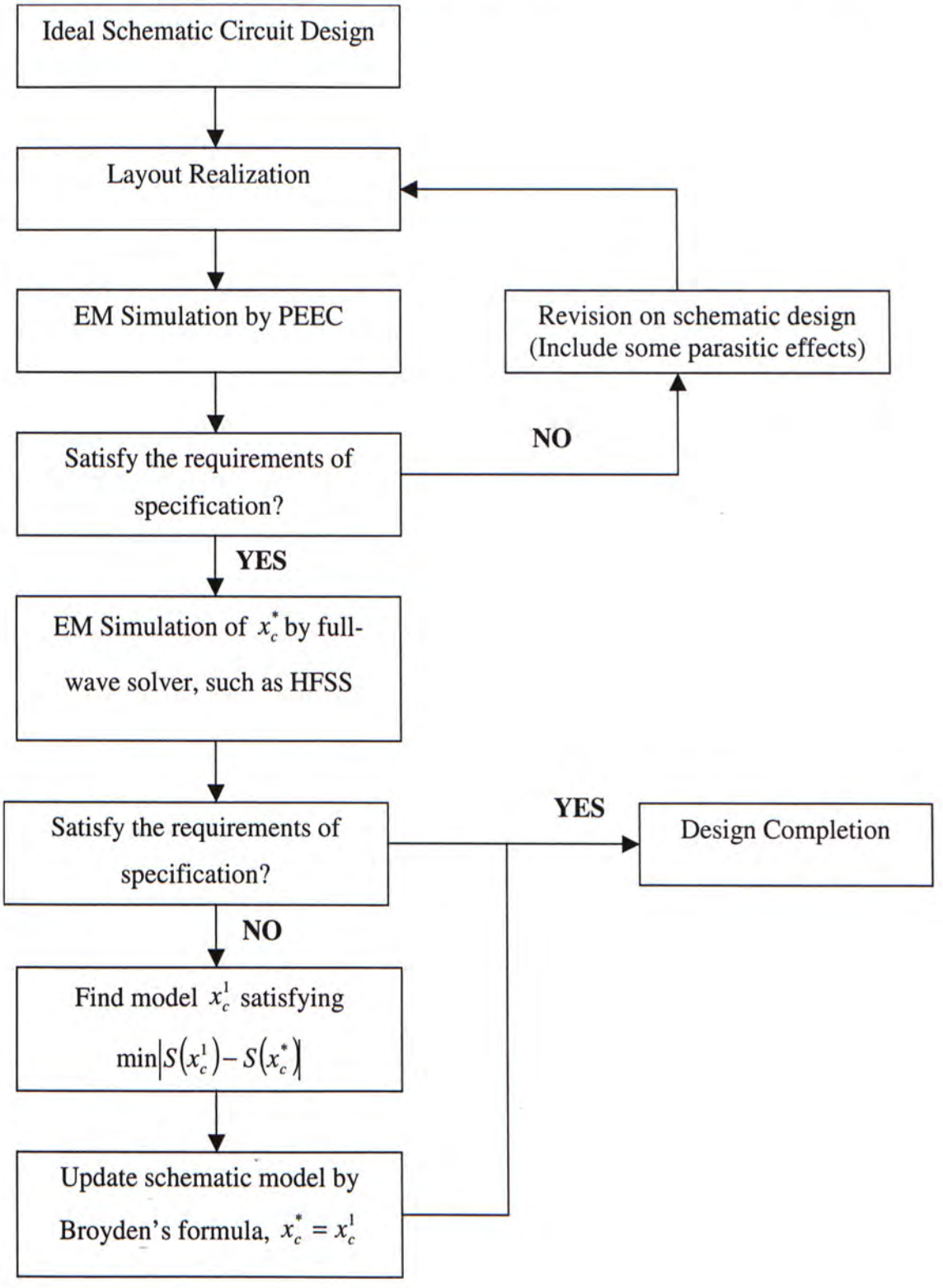

Figure 3-11 Flowchart of LTCC Multi-layer RF Circuit Design

The design example is a LTCC diplexer. Figure 3-12 gives the ideal schematic circuit for the diplexer. It is composed of a low-pass filter (GSM 850/900) and a high-pass filter (GSM 1800/1900). The specifications of the diplexer are:

$$\begin{cases} |S_{11}| < -16dB \\ |S_{12}| > -0.8dB \text{ for low pass filter;} \\ |S_{13}| < -20dB \end{cases} \tag{3-21}$$

$$\begin{cases} |S_{11}| < -15dB \\ |S_{12}| < -25dB \text{ for high pass filter.} \\ |S_{13}| > -1.0dB \end{cases} \tag{3-22}$$

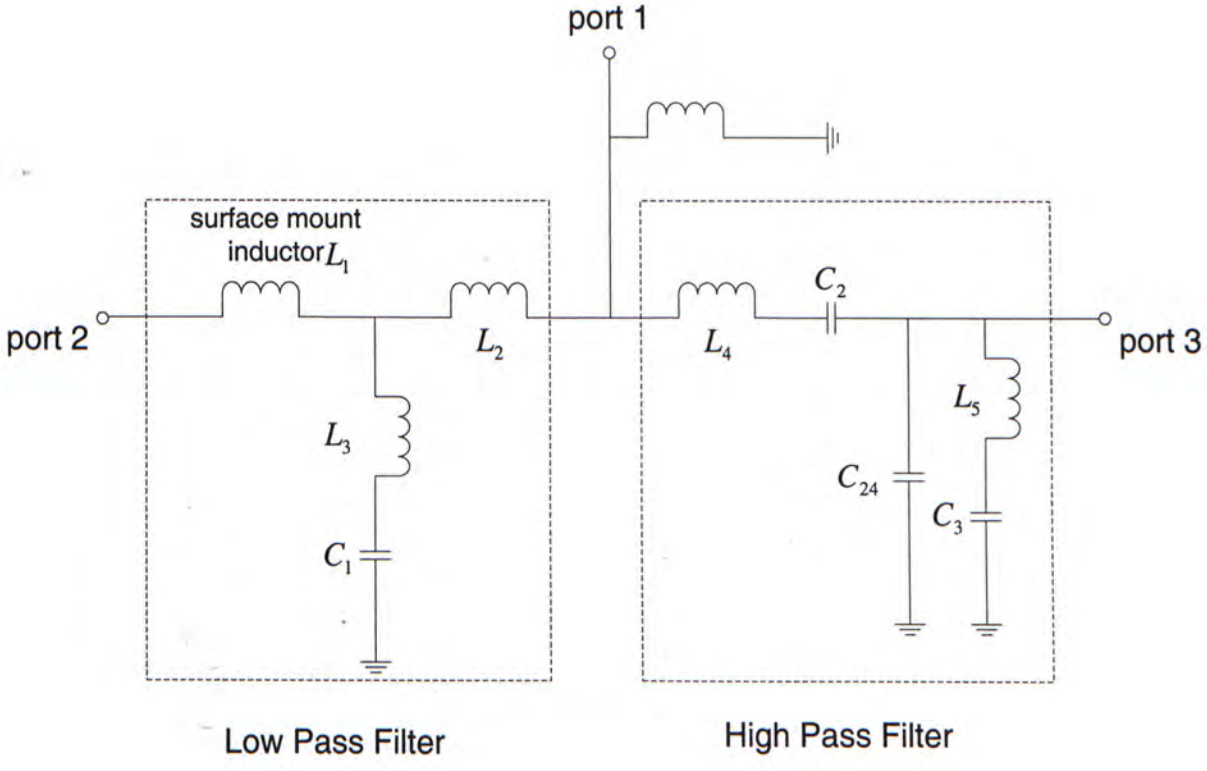

Figure 3-12 Ideal Schematic Circuit for Diplexer

The LTCC layout of the diplexer is given in figure 3-13. The detailed information about each component in the diplexer is given in appendix B. Based on the design flowchart, figure 3-11, only two iterations are needed in the application of ASM before the HFSS simulation result of the model can also satisfy the specification. Table 3-3 gives five sets of values of parameters to be optimized. The unit is micron. The parameters to be optimized are labeled on figure 3-13. x_c^* represents the coarse PEEC model, the PEEC simulation result of which satisfies the specifications, x_f^1 is the same as x_c^* and it also represents the initial fine model in HFSS simulation. x_f^2 and x_f^3 represent the second and third fine models in HFSS simulation respectively. x_c^1 and x_c^2 are the two models whose PEEC simulation results are curve-fitted as close as the HFSS simulations results of x_f^1 and x_f^2.

	x_{C1}	x_{C24}	y_{C2}	x_{C3}	x_{C5}	R_{in_L2}
$x_c^*\left(=x_f^1\right)$	790	1050	550	215	200	510
x_c^1	918.3000	1215.500	735.9630	266.5160	281.7800	515.3480
x_f^2	710	948	436	183	149	507
x_c^2	848.6380	1231.490	573.9850	301.3110	250.0000	518.3600
x_f^3	624	684	401	330	249	495
	R_{in_L3}	y_{L4}	y_{L5}	y_{L6}	y_{L7}	y_{L8}
$x_c^*\left(x_f^1\right)$	315	950	820	850	972	800
x_c^1	447.3250	762.7160	612.2160	1049.670	857.3050	1045.210
x_f^2	233	1064	949	850	972	800
x_c^2	500.0000	814.0990	658.1450	850	972	800
x_f^3	233	1064	949	850	972	800

Table 3-3 Optimized Parameters of the Diplexer

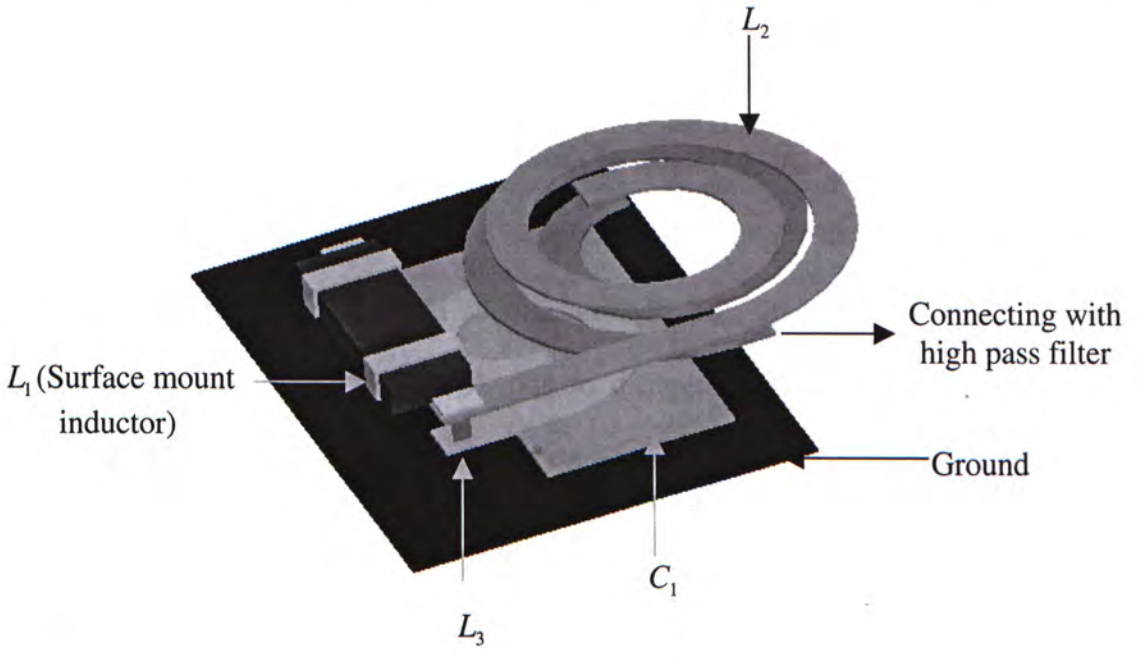

(a)

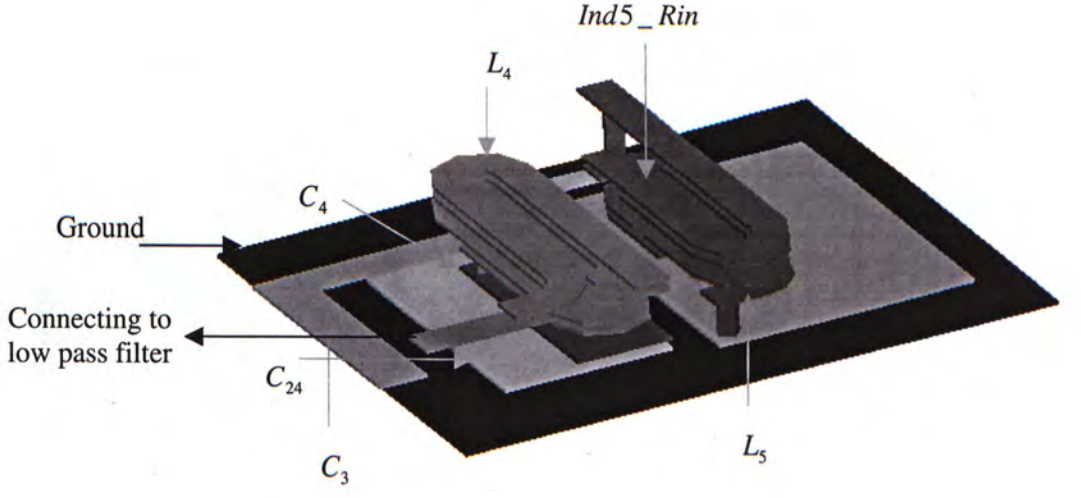

(b)

Figure 3-13 (a) Layout of Low Pass Filter in LTCC Diplexer

(b) Layout of High Pass Filter in LTCC Diplexer

To illustrate the effect of the application of ASM algorithm on LTCC diplexer design, the comparison of the frequency responses from PEEC and HFSS and also the specifications is shown in figure 3-14. From figure 3-14 (a), it can be observed that the coarse PEEC model can reflect the basic capacitive and inductive coupling, for example the low-pass and high-pass characters, the cut-off frequencies and so on, but there still be some difference between the simulation results from PEEC and HFSS due to different approximations adopted in PEEC algorithm. Sometimes, these differences are critical, such as this example of LTCC diplexer, because PEEC simulation result of x_c^* meets with all the specifications while HFSS simulation result of this initial fine model doesn't meet them. So ASM optimization is needed. In figure (d), after two iterations of ASM optimization, HFSS simulation result of x_f^3 has met with all the specifications on both frequency bands.

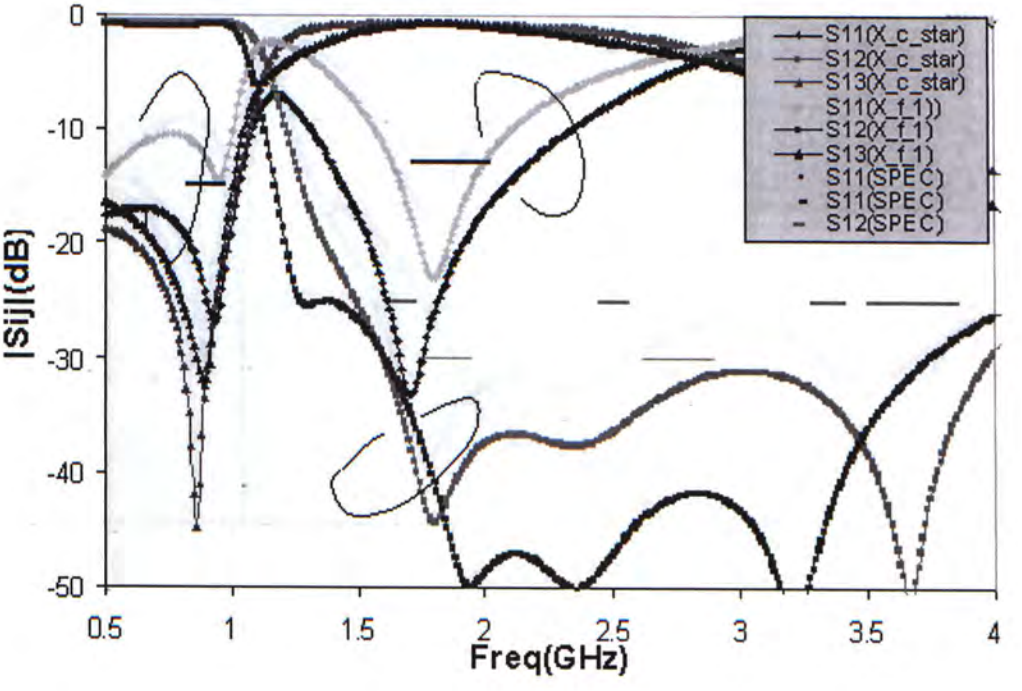

(a)

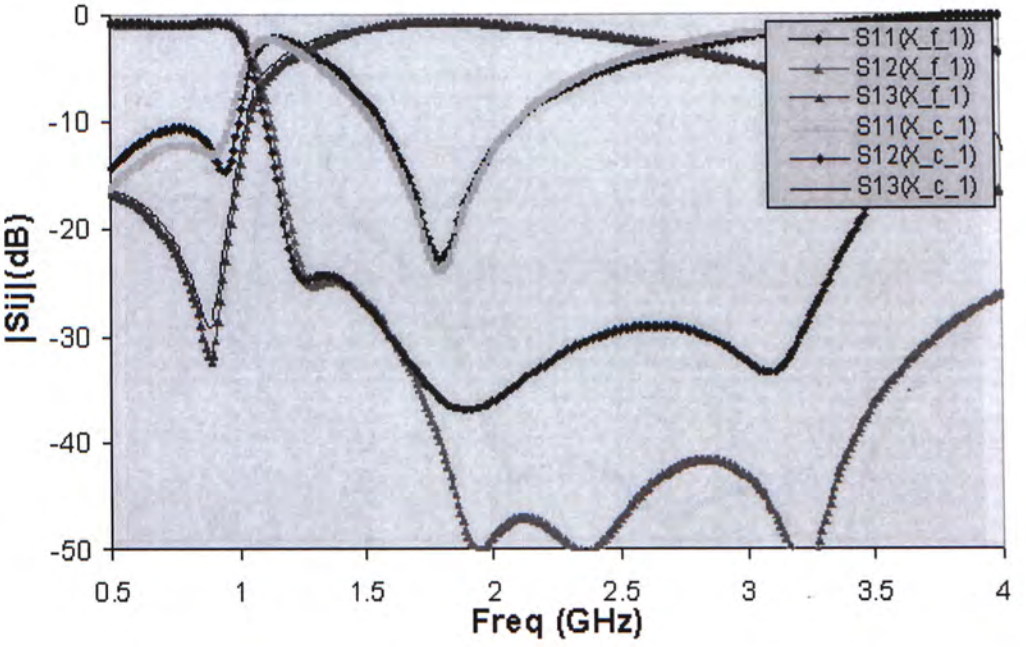
0
-10
-20
-30
-40
-50
|Sij|(dB)
0.5
1
1.5
2
2.5
3
3.5
4
Freq (GHz)
S11(X_f_1))
S12(X_f_1))
S13(X_f_1)
S11(X_c_1)
S12(X_c_1)
S13(X_c_1)

(b)

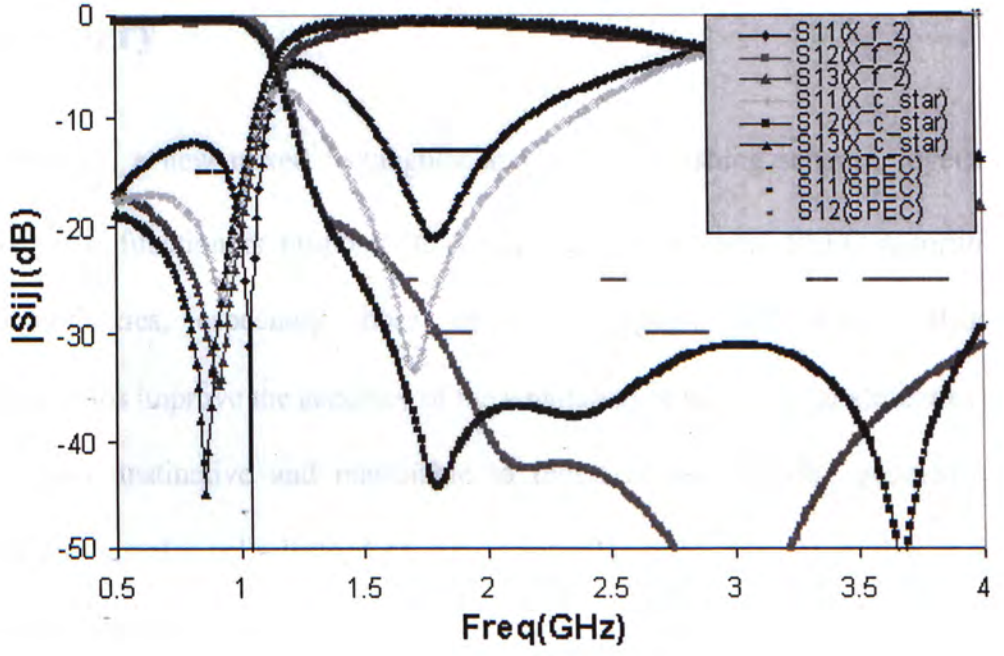
0
-10
-20
-30
-40
-50
|Sij|(dB)
0.5
1
1.5
2
2.5
3
3.5
4
Freq(GHz)
S11(X_f_2)
S12(X_f_2)
S13(X_f_2)
S11(X_c_star)
S12(X_c_star)
S13(X_c_star)
S11(SPEC)
S11(SPEC)
S12(SPEC)

(c)

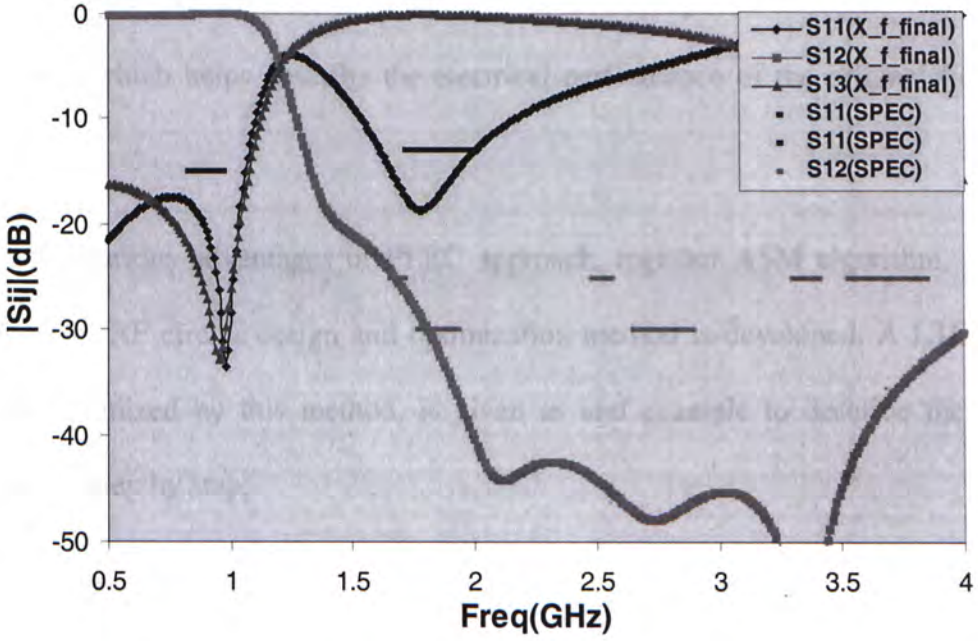

(d)

3.6. Summary

In this chapter, a new mixed rectangular and annular meshing scheme, together with a $\hat{\varphi}$ directional pulse function is proposed to generalize conventional PEEC algorithm to model irregular geometries, especially those mixed rectangular and annular structures. This enhancement helps improve the accuracy of the simulation of the irregular structures greatly since it will be more instinctive and reasonable to represent the irregular geometries with both rectangular and annular cells instead of just rectangular cells. Two examples, a circular spiral inductor and a high-pass filter, are built to validate the accuracy and efficiency of the enhanced PEEC algorithm. By comparing the simulation results got from the conventional, enhanced PEEC and full-wave solver, HFSS, the improvements of the enhanced PEEC algorithm over the conventional one can be shown clearly. Because of the adoption of various approximations,

PEEC is much faster than the full-wave EM solver, HFSS. Equivalent circuit can be got from PEEC modeling, which helps describe the electrical performance of the original field problem intuitively.

Based on the various advantages of PEEC approach, together ASM algorithm, an effective LTCC multi-layer RF circuit design and optimization method is developed. A LTCC diplexer, designed and optimized by this method, is given as and example to describe the procedures mentioned above step by step.

4

High-Frequency PEEC

4.1. Introduction

In the previous chapter, one of the approximations in conventional PEEC algorithm, rectangular meshing together with longitudinal current direction assumption, is modified. There is still another approximation, quasi-static assumption, in the conventional algorithm, which greatly simplifies the 4-D kernel integration computation of the partial elements and yields accurate results especially when the overall dimension of the system under consideration is much smaller than the operating wavelength. In other words, quasi-static analysis can be regarded as a low-frequency approximation of full-wave analysis and well suited for electric small size problem. But with the ever-increasing operating frequency, this approximation begins to break down because the structure has been a significant fraction of a wavelength. It is the purpose of this chapter to introduce full-wave technique, aiming at solving the modeling of high frequency or radiation problems.

High frequency PEEC approach requires the computation of full-wave Green's function for a multi-layer structure. It was traditionally represented by Sommerfeld integrals, which is very time-consuming. In this chapter, complex image method is applied instead of it, which only requires only three or four images with complex locations.

4.2. Spatial Domain Green's Functions

The spatial domain Green's function of multi-layer media is the object of the derivation in the full-wave technique. To get the spatial domain Green's function, the spectral domain counterpart is derived first, then inverse Fourier transform or inverse Hankel transform is applied.

4.2.1 Full-wave Spectral Domain Green's Functions

Apply the theories of wave matrix and multi-section transmission line model [19], [20], to a typical structure in LTCC microwave circuit shown in figure 4-1. The x-directed electric dipole is regarded as the source. Since the potential functions generated by either x or y directed electric dipole have similar forms, except that parameter x in all the expressions is replaced by y, for clarity, only x-directed electric dipole is discussed here.

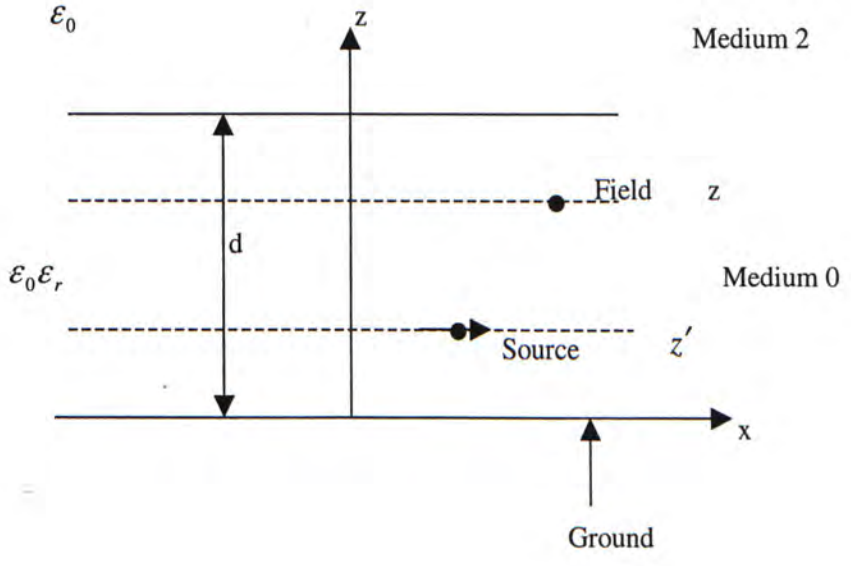

Figure 4-1: Electric dipole inside the substrate

There are detailed derivations about the spectral domain potential functions in [19] and [20]. Only the results are given in this thesis for the simplicity of the presentation.

Quasi-static spectral Green's functions can be written as:

$$\tilde{A}_x^{quasi} = \frac{\mu}{j2k_{z1}}\left[e^{-jk_z(z-z')} - e^{-jk_z(z+z')}\right] \tag{4-1}$$

$$\begin{aligned}\tilde{\Phi}_q^{quasi} = &\frac{1}{j\varpi\varepsilon_0\varepsilon_r}\frac{1}{j2k_{z1}}\left\{e^{-jk_{z1}(z-z')} - e^{-jk_{z1}(z+z')}\right. \\ &\left. + \frac{K}{1+Ke^{-j2k_{z1}d}}\left[e^{-jk_{z1}(2d+z+z')} - e^{-jk_{z1}(2d+z-z')} - e^{-jk_{z1}(2d-z+z')} + e^{-jk_{z1}(2d-z-z')}\right]\right\}\end{aligned} \tag{4-2}$$

Full-wave Green's functions can be written as:

$$\tilde{A}_x = \tilde{A}_x^{quasi} + \frac{\mu_0}{j2k_{z1}}T_1'A \tag{4-3}$$

$$\tilde{\Phi}_q = \tilde{\Phi}_q^{quasi} + \frac{1}{j\varpi\varepsilon_0\varepsilon_r}\frac{1}{j2k_{z1}}\left(T_1' + T_2' - \frac{K}{1+Ke^{-j2k_{z1}d}}\right)A \tag{4-4}$$

in which

$$A = \left[e^{-jk_{z1}(2d+z+z')} - e^{-jk_{z1}(2d-z+z')} - e^{-jk_{z1}(2d+z-z')} + e^{-jk_{z1}(2d-z-z')}\right] \tag{4-5}$$

$$T_1' = \frac{\Gamma_{02}^{TE}}{1+\Gamma_{02}^{TE}e^{-j2k_{z1}d}} \tag{4-6}$$

$$T_2' = \frac{2(\varepsilon_r - 1)k_{z1}^2}{(k_{z1}+k_{z0})(k_{z1}+\varepsilon_r k_{z0})(1+\Gamma_{02}^{TE}e^{-jk_{z1}2d})(1-\Gamma_{02}^{TM}e^{-jk_{z1}2d})} \tag{4-7}$$

The definitions of all of the parameters in the above equations can be found in [19] and [20].

4.2.2 Full-wave Spatial Domain Green's Functions

Based on the spectral Green's functions given in the last section, inverse Hankel Transform in Cylindrical coordinate system and Sommerfeld Identity are applied to get the spatial counterparts. But in the transformation, the integrands, spectral Green's functions, tend to be highly oscillatory and low decaying, hence, computationally expensive to evaluate. Fortunately, the solution developed in [21] and improved in [22] breaks the spatial function into three contributions:

$$G = A + B + C \tag{4-8}$$

in which

A represents the contribution from quasi-static term, which dominates in the near field region:

$$A_x^{quasi} = \frac{\mu_0}{4\pi}\left[\frac{e^{-jk_1 r_0}}{r_0} - \frac{e^{-jk_1 r_0'}}{r_0'}\right] \tag{4-9}$$

$$\Phi_q^{quasi} = \frac{1}{j\varpi\varepsilon_0\varepsilon_r}\frac{1}{4\pi}\left\{\frac{e^{-jk_1 r_0}}{r_0} - \frac{e^{-jk_1 r_0'}}{r_0'} - \sum_{n=1}^{\infty}(-K)^n\left[\frac{e^{-jk_1 r_n'}}{r_n'} - \frac{e^{-jk_1 r_n''}}{r_n''} - \frac{e^{-jk_1 r_n'''}}{r_n'''} + \frac{e^{-jk_1 r_n''''}}{r_n''''}\right]\right\} \tag{4-10}$$

in which, $r_0 = \sqrt{\rho^2 + (z - z'^2)}$, $r_0' = \sqrt{\rho^2 + (z + z')^2}$

$$\begin{cases} r_n' = \sqrt{\rho^2 + (2nd + z + z')^2} \\ r_n'' = \sqrt{\rho^2 + (2nd + z - z')^2} \\ r_n''' = \sqrt{\rho^2 + (2nd - z + z')^2} \\ r'''' = \sqrt{\rho^2 + (2nd - z - z')^2} \end{cases}$$

Two approximations are made to quasi-static Green's functions. If electric small problem is considered, that is, the distance between the source and field points are very small, r can be approximated by zero. Another approximation is to suppose the frequency to be very low, that is, approximate the frequency ϖ, or the wave-number k to be zero. After these two assumptions, the term e^{-jkr} will approach 1, then the quasi-static Green's functions will finally be simplified to be of the following forms:

$$A_x^{quasi} = \frac{\mu_0}{4\pi}\left[\frac{1}{r_0} - \frac{1}{r_0'}\right] \tag{4-11}$$

$$\Phi_q^{quasi} = \frac{1}{j\varpi\varepsilon_0\varepsilon_r}\frac{1}{4\pi}\left\{\frac{1}{r_0} - \frac{1}{r_0'} - \sum_{n=1}^{\infty}(-K)^n\left[\frac{1}{r_n'} - \frac{1}{r_n''} - \frac{1}{r_n'''} + \frac{1}{r_n''''}\right]\right\} \tag{4-12}$$

The above two equations are just the Green's functions adopted in quasi-static PEEC modeling method, so from the derivation, we can prove that the conventional PEEC algorithm is only suitable for modeling electric small and low frequency problems.

B represents the contribution from the complex images, which are related to radiated waves and dominate in the intermediate field region. It is expanded into a series of exponentials, which are interpreted as images with complex displacements, called complex images, [22], [23]:

$$A_x - A_x^{quasi} = \frac{\mu_0}{4\pi}\sum_{i=1}^{N} a_i\left(\frac{e^{-jk_1 r_i'}}{r_i'} - \frac{e^{-jk_1 r_i''}}{r_i''} - \frac{e^{-jk_1 r_i'''}}{r_i'''} + \frac{e^{-jk_1 r_i''''}}{r_i''''}\right) \tag{4-13}$$

$$\Phi_q - \Phi_q^{quasi} = \frac{1}{j\varpi\varepsilon_0\varepsilon_r}\frac{1}{4\pi}\sum_{i=1}^{N} a_i\left[\frac{e^{-jk_1 r_n'}}{r_n'} - \frac{e^{-jk_1 r_n''}}{r_n''} - \frac{e^{-jk_1 r_n'''}}{r_n'''} + \frac{e^{-jk_1 r_n''''}}{r_n''''}\right] \tag{4-14}$$

in which

$$\begin{cases} r_i' = \sqrt{\rho^2 + \left(z + z' - \dfrac{b_i}{k_0}\right)^2} \\ r_i'' = \sqrt{\rho^2 + \left(z - z' - \dfrac{b_i}{k_0}\right)^2} \\ r_i''' = \sqrt{\rho^2 + \left(-z + z' - \dfrac{b_i}{k_0}\right)^2} \\ r_i'''' = \sqrt{\rho^2 + \left(-z - z' - \dfrac{b_i}{k_0}\right)^2} \end{cases},$$

a_i and b_i are complex coefficients got through Prony's method, which is given in [7].

C represents the contribution from surface waves. It comes from poles in the spectral Green's functions, which are removed and evaluated using residue calculus. However, since surface wave dominates in far field region and the calculations of the residues are very time-consuming, in this thesis, the poles for the surface wave aren't extracted. Numerical examples given soon will show that the neglect of the surface wave won't have much influence on the simulation accuracy.

4.3. Frequency-dependent Complex Partial Elements

With the application of full-wave techniques, the partial elements in high-frequency PEEC modeling method now have two new properties. As shown in the previous section, because of the existence of e^{-jkr}, the full-wave spatial domain Green's functions, equations (4-9) to (4-10), are complex functions of r now instead of real ones. Substitute them into MPIE, an equivalent circuit model can be obtained, the partial inductors and capacitors of which, are all of complex values instead of real ones.

The impedance of a complex inductor, $L = L' - jL''$ and the reactance of a complex capacitor, $C = C' - jC''$, can be written as:

$$Z_L = j\varpi L = j\varpi(L' - jL'') = j\varpi L' + \varpi L'' \tag{4-15}$$

$$Y_C = j\varpi C = j\varpi(C' - jC'') = j\varpi C' + \varpi C'' \tag{4-16}$$

So a complex inductor is equivalent to an inductor L', in series with a resistor $\varpi L''$, as shown in figure 4-2 (a), while a complex capacitor C' is equivalent to a capacitor C', in parallel with a resistor $\frac{1}{\varpi C''}$, as shown in figure 4-2 (b).

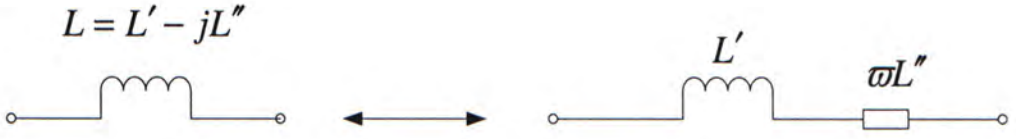

(a)

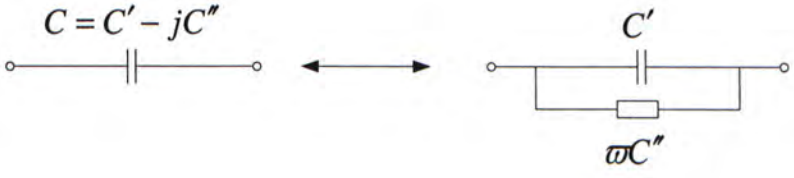

(b)

Figure 4-2 (a) Complex Inductor (b) Complex Capacitor

The above analysis of the complex partial elements shows the imaginary part in a partial element, L'' or C'', represents the radiation loss in the circuit or system under analysis, which is represented by term B in equation (4-8) in the previous section.

To show the frequency dependence of partial elements in high frequency PEEC, consider an example structure of a microstrip filter. The substrate used to build the microstrip filter has a dielectric constant of 2.2 and a height of 0.794mm, which is the same as what is discussed in the previous section. The low pass filter is a symmetrical structure and the dimension of every section of the microstrip lines is labeled in figure 4-3 (a). The maximum distance of the source and field points in this filter is about 22.5mm. The maximum frequency under consideration is 13GHz, so from equation (3-22), the wavelength can be calculated to be 15.56mm, which is smaller than the structure dimension. So in this structure, quasi-static approximation cannot be made.

Consider the near field points, since r is small, the electromagnetic coupling between such source and field points is dominant in the whole coupling matrix. While the frequency dependence of the coupling in such cases is not evident, because when r is small, it is an electric small problem, the electromagnetic coupling tends to be independent on frequency, the same as the case in conventional quasi-static approximation. And it is just the opposite case for far field points. In the partial elements, the inductance matrix is directly got from the calculation of the 4-D integration, which can reflect the changes introduced to the integration due to the application of full-wave techniques to PEEC modeling method. On the other hand, the capacitance matrix is got from the inverse of the matrix of potential coefficient. So in the discussion of the frequency dependence of the partial elements, only partial inductance is considered. What's more, since

compared with the real part, the imaginary part of the partial element is much smaller, , only the real part of the partial element is analyzed.

In this example of microstrip filter, a pair of inductive meshes, one shifted by 1st and 2nd capacitive meshes and the other got from 9th and 10th capacitive meshes, are chosen. The distance between these two meshes is 3.6201mm, which is about 1/4 of the wavelength so both the value and the frequency dependence of their mutual inductance are neither too large nor too small, which is shown in figure 4-3 (b). For each frequency point, there is a different output equivalent circuit, hence a different electrical performance. So sweeping the frequency band to get the full-time frequency response is necessary for full-wave modeling.

As shown in figure 4-3 (b), in the frequency band under analysis, 7GHz to 9GHz, the partial mutual inductance is a slow-varying function of frequency ϖ . If the center frequency, $\varpi = 8GHz$, is set as reference, that is, to represent the partial inductance between these two meshes over the whole frequency band with the inductance on 8GHz. The approximation error of the partial mutual inductance on the three typical frequency ponits, 7GHz, 8GHz and 9GHz, are 5.38%, 0% and 4.21% respectively, so it will be a very good approximation to use the frequency response at $\varpi = 8GHz$ to represent that on the whole frequency band. In fact, in the quasi-static approximation, this is a similar case except that $\varpi = 0GHz$ is set as the reference, we can also see that the approximation errors on the same three frequency points are 26.2%, 29.9% and 32.9% respectively if $\varpi = 0GHz$ is set to be the reference, which are much larger than those in the above case. So similar with the conventional algorithm, the performance over the whole frequency band can still be represented by that at a single frequency point, the only difference is that this reference frequency point must be set as the center frequency in the operating frequency band instead of zero frequency.

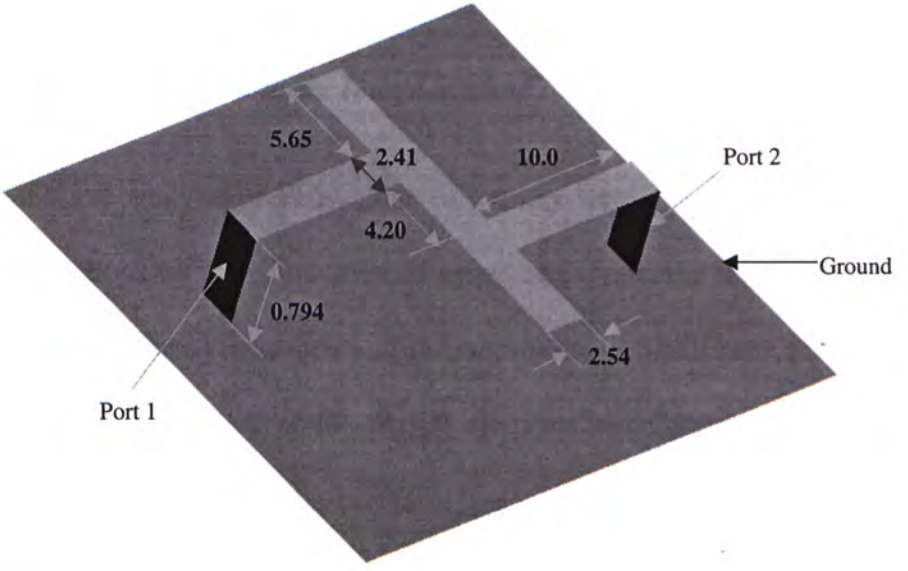

(a)

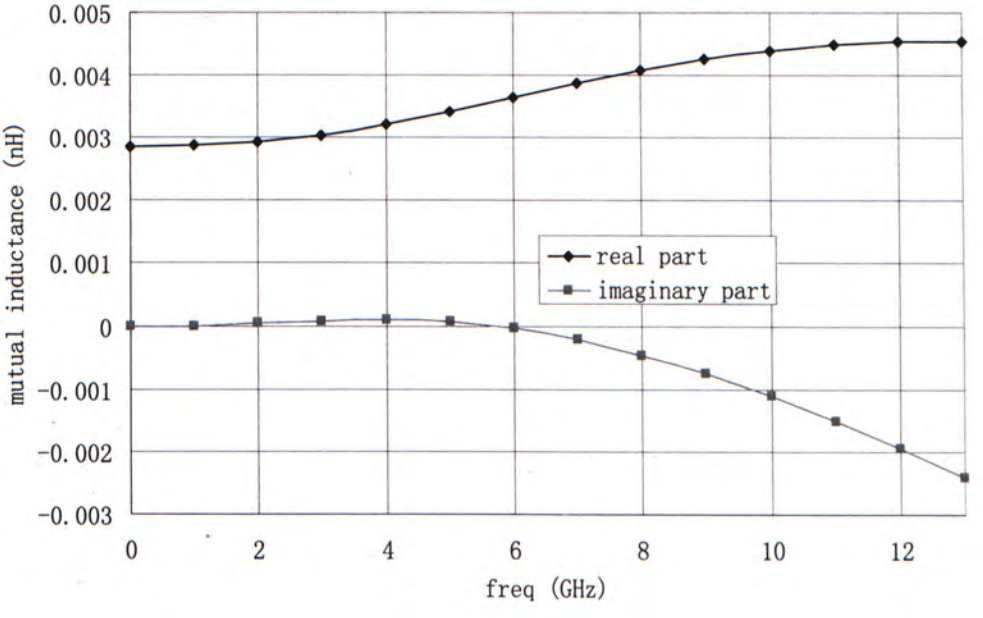

(b)

Figure 4-3 (a) 3-D structure of a microstrip low pass filter

(b) frequency dependence of partial mutual inductance

4.4. Numerical Results of High Frequency PEEC Modeling

4.4.1 Numerical Discussion of Complex Image Method

During the full-wave analysis of PEEC, one of the key steps is to approximate the full-wave spectral Green's functions by the summation of series of exponential terms, which is also called complex image method. Since the accuracy of this approximation will have great influence on the spatial Green's functions then affect the partial elements simulation accuracy finally, in this section, the approximation error of the complex image method in the spectral domain will be studied numerically through a simple spectral function.

There are three spectral functions to be approximated by complex image method. A substrate with a dielectric constant of 2.2 and height of 0.794mm is used to verify the approximation accuracy of the complex image method. The same substrate will be adopted in the following example structures, microstrip low-pass filter and patch antenna. Three spectral functions are:

$$f_1 = \frac{Kf_e}{1+Kf_e} \tag{4-17}$$

$$f_2 = \frac{\Gamma_{TE} f_e}{1+\Gamma_{TE} f_e} \tag{4-18}$$

$$f_3 = f_2 - f_1 + \frac{2(\varepsilon_r - 1)u_1^2}{(u_1+u_0)(u_1+\varepsilon_r u_0)(1+\Gamma_{TE} f_e)(1-\Gamma_{TM} f_e)} \tag{4-19}$$

in which

$$\begin{cases} u_1 = t + j\sqrt{\varepsilon_r}\left(1 - \dfrac{t}{T_0}\right) \\ u_0 = \sqrt{u_1^2 + (\varepsilon_r - 1)} \\ f_e = e^{-2dk_0 u_1} \\ \Gamma_{TE} = \dfrac{u_1 - u_0}{u_1 + u_0} \\ \Gamma_{TM} = \dfrac{u_1 - \varepsilon_r u_0}{u_1 + \varepsilon_r u_0} \end{cases}$$

The other parameters in the above questions, (4-17) to (4-19), all have the same definitions as [19] and [20]. With given t, the functions, f_1, f_2 and f_3, can be calculated theoretically. At the same time, they can also be approximated by the sum of exponential terms via complex image method. The results are compared to verify the approximation accuracy in the spectral domain.

In the simulation, the choice of the truncation point T_0 will also affect the accuracy. When T_0 is large, the integration path is far away from the real axis of complex k_ρ plane, which is relatively smooth, so it is easier to get higher approximation accuracy. But with the increase of T_0, the spectral functions contain more information about larger k_ρ, as a result, the information about small k_ρ will become less. So considerable simulation error may occur if the field point is far away from the source point.

On the other hand, if T_0 is too small, the integration path is very near to the real axis of complex k_ρ plane, then the complexity of the spectral function along the integration path is increased, which decreases the approximation accuracy of the complex images. At the same time, since k_ρ is always small in this case, there may be large simulation error when the field is very

near to the source. It is given in [20] that, based on the numerical experiments, T_0 should be chosen like this:

$$T_0 \geq \sqrt{\varepsilon_r - 1} \tag{4-20}$$

Table 4-1 (a), (b), (c) give the complex coefficients a_i and b_i for the three spectral functions respectively.

Complex a_i	$a_1 = 0.0371 + i0.0356$	$a_2 = 0.1854 - i0.1213$	$a_3 = 0.1766 - i0.1021$
Complex b_i	$b_1 = -1.3098 + i0.4600$	$b_2 = -2.0268 + i0.9351$	$b_3 = -3.1626 + i2.0976$

(a)

Complex a_i	$a_1 = -0.1208 - i0.3815$	$a_2 = 0.1745 - i0.0387$	$a_3 = -0.0228 + i0.0299$
Complex b_i	$b_1 = -1.2827 + i0.3805$	$b_2 = -2.5515 + i0.7645$	$b_3 = -3.8722 + i0.6953$

(b)

Complex a_i	$a_1 = 0.0842 + i0.0180$	$a_2 = 0.2307 - i0.2859$	$a_3 = -0.3166 - i0.1978$
Complex b_i	$b_1 = -1.5614 + i0.2125$	$b_2 = -2.2937 + i0.5387$	$b_3 = -3.8202 + i1.4189$

(c)

Table 4-1 Complex Coefficients for three different spectral functions

(a): function (4-57); (b) function (4-58); (c) function (4-59)

Figure 4-4 (a), (b), (c) give the comparison of the theoretical and approximated results of three spectral domain functions. They meet very well. In above three different cases, T_0 is chosen to be 5.0, 5.0, 20.0 respectively and the three numbers of complex images are all chosen to be 3, that is, each of the three spectral functions is finally approximated by the sum of three exponential terms. So through proper choice of T_0 and the number of complex images, the spectral domain functions f_1, f_2 and f_3 can be very accurately approximated by the sum of the exponential terms.

The substrates are chosen to be the same as the example in this section, they all have the same ε_r. To assure enough approximation accuracy, same as this sections, T_0 are also chosen to be 5.0, 5.0 and 20.0 for the three different spectral functions and the number of the complex images is chosen to be three.

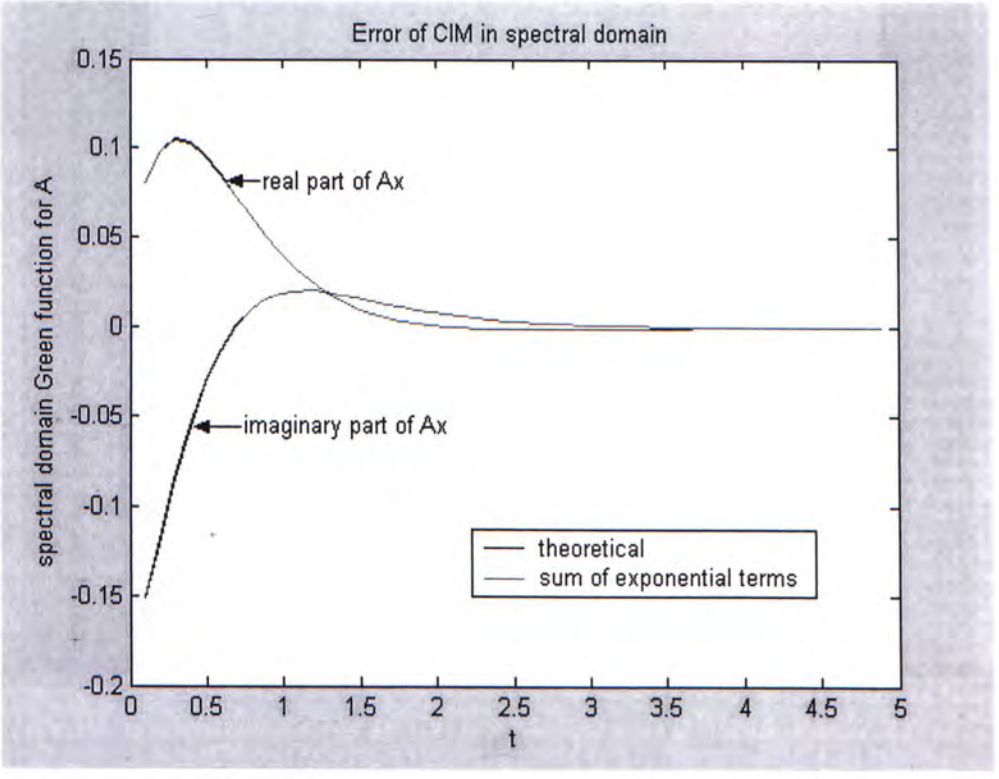

(a)

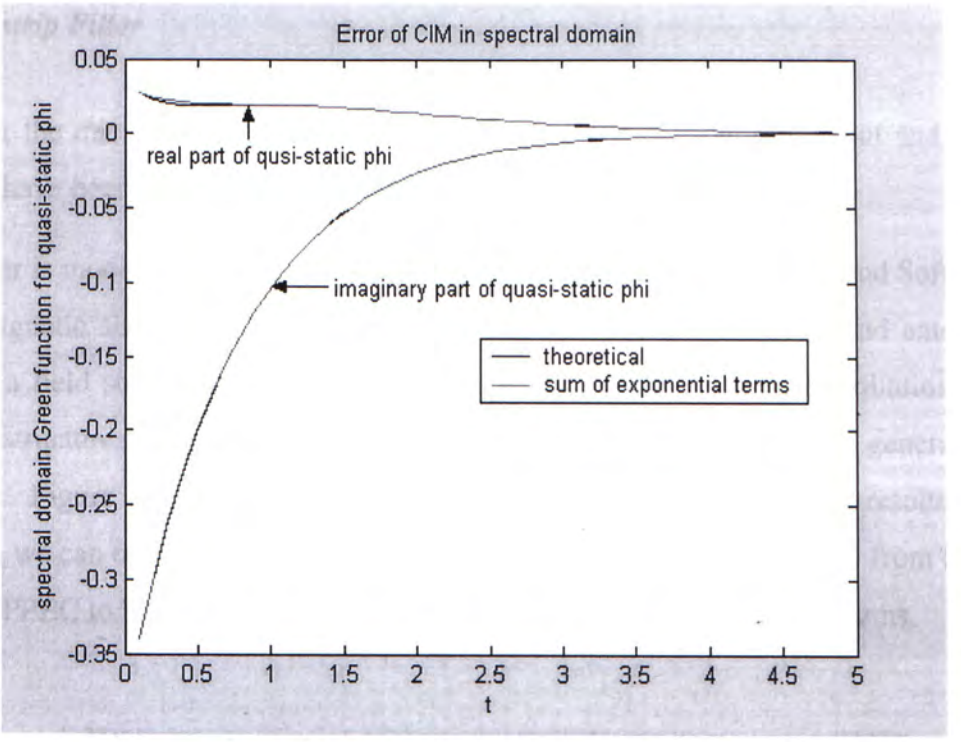

(b)

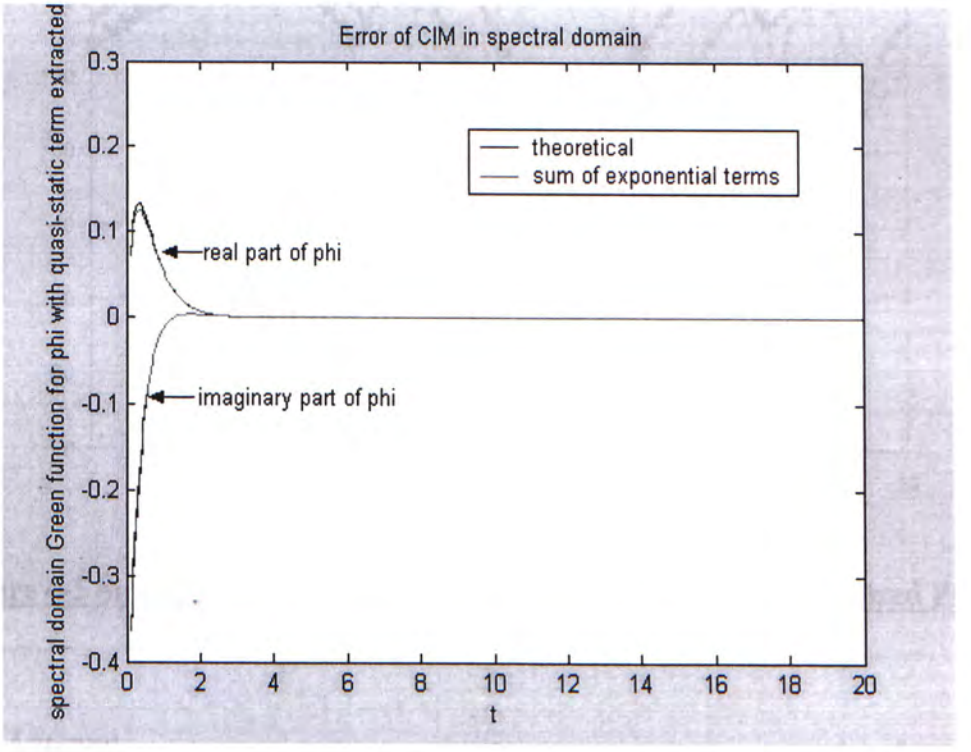

(c)

Figure 4-4 Comparison of the theoretical and approximated spectral functions

(a): function (4-57); (b) function (4-58); (c) function (4-59)

4.4.2 Microstrip Filter

Consider the microstrip filter mentioned in the previous section, the layout and the detailed dimensions have been given in figure 4-5 (a).

This filter is modeled by three simulators. The first one is IE3D, from Zeland Software, Inc. It is electromagnetic simulation and optimization software useful for circuit and antenna design, which uses a field solver, based on a full-wave, MoM to solve current distribution on 3D and multi-layer structures of general shape. The other two are conventional and generalized PEEC respectively. Figure 4-5 gives the comparison of the three simulation results. From the comparison, we can obviously see the improvement of the simulation accuracy from conventional quasi-static PEEC to high-frequency PEEC to solve such high frequency problems.

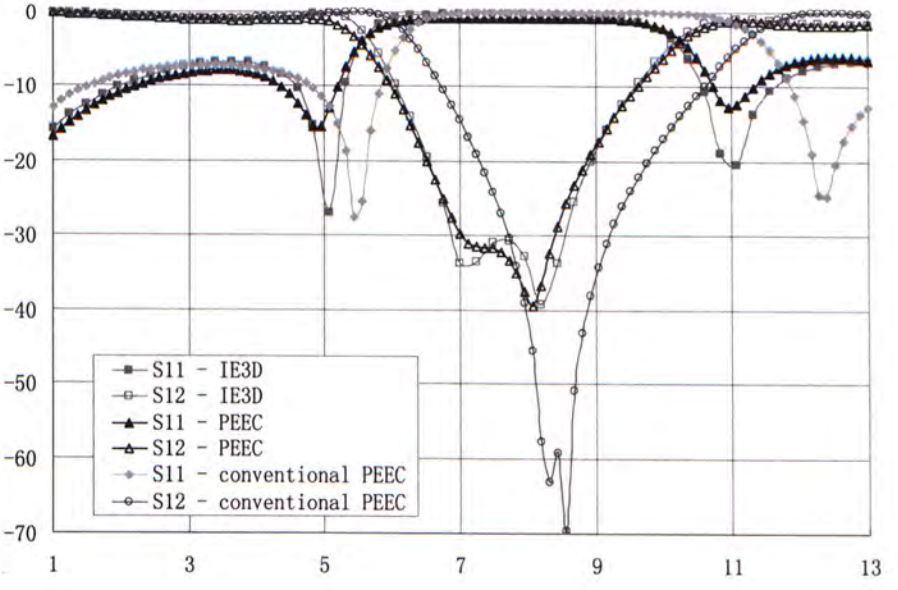

Figure 4-5 Simulation results from IE3D, conventional and generalized PEEC

4.4.3 Patch Antenna

Another example is a patch antenna fed by a microstrip line. The substrate is also the same as that in section 4.4.1.

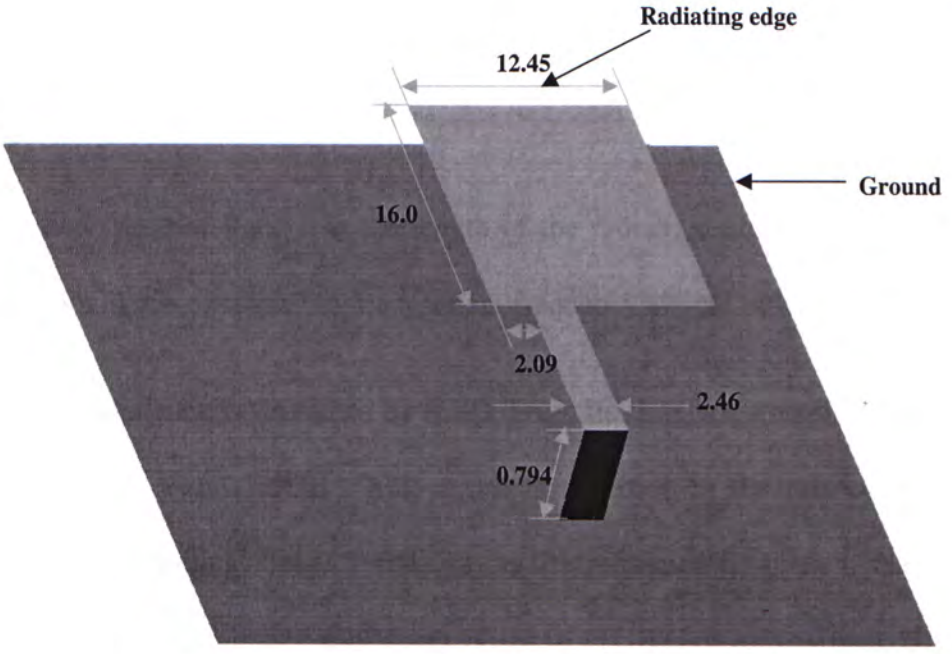

(a)

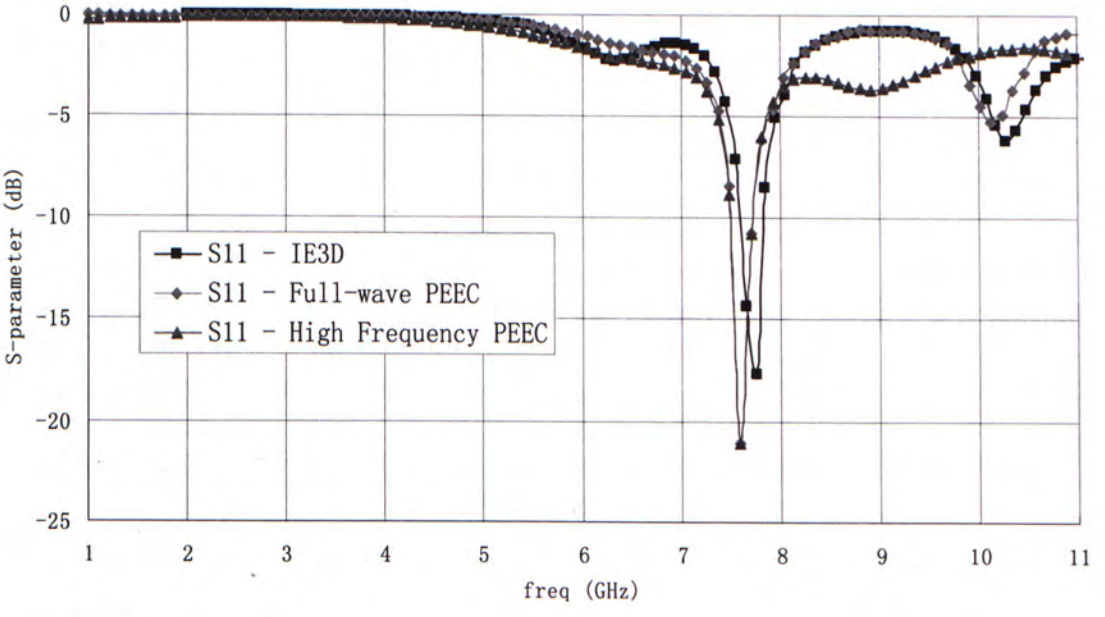

(b)

Figure 4-6 (a): 3-D layout of a patch antenna

(b) Simulation Results from IE3D, High Frequency PEEC and Full-wave PEEC

According to the theory of patch antenna, the resonant frequency should be:

$$f_r = \frac{c}{2.0a\sqrt{\varepsilon_r}} \tag{4-21}$$

in which, c is the speed of light, a is the length of the radiating edge of the rectangular patch, which is 12.45mm in this example, so the resonant frequency should be 8.12GHz.

Firstly, the patch antenna is simulated by IE3D. From its simulation results, we can see that the resonant frequency is about 7.5GHz. This result is regarded as the reference to validate the accuracy of PEEC modeling. Set 7.5 GHz to be the reference frequency, that is, the partial elements over the whole frequency band from 1GHz to 11GHz are approximated by those on the frequency 7.5GHz. The simulation result from high-frequency PEEC is given in figure 4-6 (b). From the comparison with that got from IE3D, the simulation below 8GHz is quite accurate. For the frequency band over 8GHz, the farer away from the reference frequency 7.5GHz, the worse the simulation is.

To improve the simulation accuracy, for each frequency point, the reference frequency is set to be itself. This is in fact the basic theory of full-wave PEEC. After applying this technique, the simulation accuracy has been greatly improved, as given in figure 4-6 (b). From the comparison, if the frequency band under analysis is small enough, high-frequency PEEC can provide high simulation accuracy. While if the problem under analysis is a relatively broad band one, full-wave PEEC must be applied to model it.

What's mentionable is that this antenna problem cannot be solved by conventional PEEC because in the quasi-static approximation of the conventional algorithm, since the full-wave terms related with radiation are totally omitted, no radiation loss is included. While in generalized

PEEC, as stated in equation (4-41), B is the term related to the radiated waves. So by applying full-wave techniques, PEEC has been generalized to solve such problems including radiation loss with satisfactory accuracy.

4.5. Summary

Due to the quasi-static approximation made in the conventional PEEC algorithm, it is well suited to model low frequency or electric small problems. To generalize the algorithm to solve high frequency problems or problems including radiation loss, full-wave technique is introduced into PEEC to replace quasi-static approximation. The key step in the application of the full-wave technique is the replacement of the quasi-static Green's functions by the full-wave counterparts. The calculation of the partial elements from the spatial Green's functions is carried out through Gauss numerical methods instead of closed-form analytical expressions in the conventional algorithm because of the increasing complexity of the integrands due to the application of the full-wave Green's functions.

From some numerical examples, it is obvious that after the application of the full-wave technique, the simulation accuracy of PEEC algorithm has been greatly improved and also it can be used to model problems with radiation loss, which cannot be modeled in the conventional algorithm.

5

Concluding Remarks

5.1. Two Enhancements in PEEC Modeling

With the ever-increasing complexity of the RF circuits nowadays, there are always both passive and active components in one physical system. To understand the performance of the whole system, the combination of EM simulation and circuit domain analysis becomes more and more important. PEEC modeling method is particularly suitable for solving this kind of mixed EM and circuit problems. It can extract an equivalent circuit model from the original passive structure and solve it, together with the active components in the same RF system, through conventional circuit solvers, such as SPICE.

While in conventional PEEC modeling, to simplify the analysis process and accelerate the simulation speed, many approximations are supposed, somehow limiting the application of this modeling method to some special cases. In [7], an efficient generalized PEEC algorithm is proposed to model the LTCC circuits with finite metal strip thickness. It breaks the limitation of the thin-film approximation supposed in conventional PEEC. In this thesis, some other enhancements of conventional algorithm are proposed to generalize the application of this modeling method.

In conventional PEEC, the basic building element for modeling a passive structure is a rectangle. Almost all of the most commonly used structures in passive circuit design are rectangular ones, such as interconnects, which are always thin and long, so PEEC is well suitable to model such geometries. But when the structure under analysis is irregular, it is intuitive to be unsuitable to model a non-rectangular structure with rectangular meshes. A mixed rectangular and annular meshing scheme is proposed in this thesis to solve this problem. By applying this new meshing scheme in PEEC, the simulation accuracy of the irregular structures, especially those mixed rectangular and annular ones, is greatly improved.

Another approximation in conventional PEEC is the quasi-static approximation, which makes it possible to get closed-form partial inductances and partial capacitances, hence greatly shortens the simulation time, compared with time-consuming numerical techniques adopted in full-wave analysis. But this approximation will bring considerable error when the structure dimensions become comparable to or even larger than the operating wavelength because of the neglect of the surface and leaky wave effects in the quasi-static approximation. Furthermore, since leaky wave effects are not included in conventional PEEC, it cannot be used to model radiation problems, such as antennas. To facilitate the PEEC modeling method to model such problems, full-wave techniques are applied to replace the quasi-static approximation.

Compared with other EM modeling software, such as HFSS and IE3D, if quasi-static approximation is used in PEEC, the simulation speed will be much faster because it avoids the time-consuming numerical integrations in some dimensions and also neglects the leaky wave and surface wave effects. Furthermore, PEEC can derive simplified equivalent circuit model, from which the electrical performance of the passive structure can be understood from circuit domain, which is much more intuitively than from field domain. Based on these features of PEEC, also

with the help of aggressive space-mapping techniques, a new design and optimization method for RF passive circuit design and optimization applying PEEC is introduced in this thesis.

5.2. Limitations of Enhanced PEEC Modeling

Although some enhancements have been introduced to generalize the application of PEEC modeling method, there are still some limitations remained in the current algorithm. Firstly, in full-wave analysis, the complex image method is used to approximate the spectral Green's functions with the sum of several exponential terms. During the implementation, it is found that Prony's method adopted in the complex image is very noise-sensitive, which will influence the simulation accuracy. Secondly, although full-wave technique has been applied to PEEC, only single layer substrate case is considered in the current algorithm. But due to the ever-increasing application of multi-layer geometries, such as multi-layer microstrip antennas, the generalization of PEEC to model multi-layer substrate problem is becoming more and more necessary.

5.3. Future Work

Aiming at the limitations mentioned in the previous section, more work could be done to further generalize the PEEC modeling method.

1. Least-square Prony's method or generalized pencil of function (GPOF) [24] can be tried to replace the Prony's method adopted in the current version of complex image method.

2. Multi-layered media Green's functions for integral equations are developed in [25], the results of which can be used in PEEC to replace the current single layered substrate full-wave Green's functions.

3. Many other techniques can be applied to further accelerate the PEEC.

Since PEEC modeling method does show a promising potential in microwave circuit design and optimization, it is worthwhile to carry on the study on it further.

APPENDIX A

Filter Dimensions for the circular spiral inductor shown in figure 3-9 in P. 53

The first layer with z = 238.76 microns:

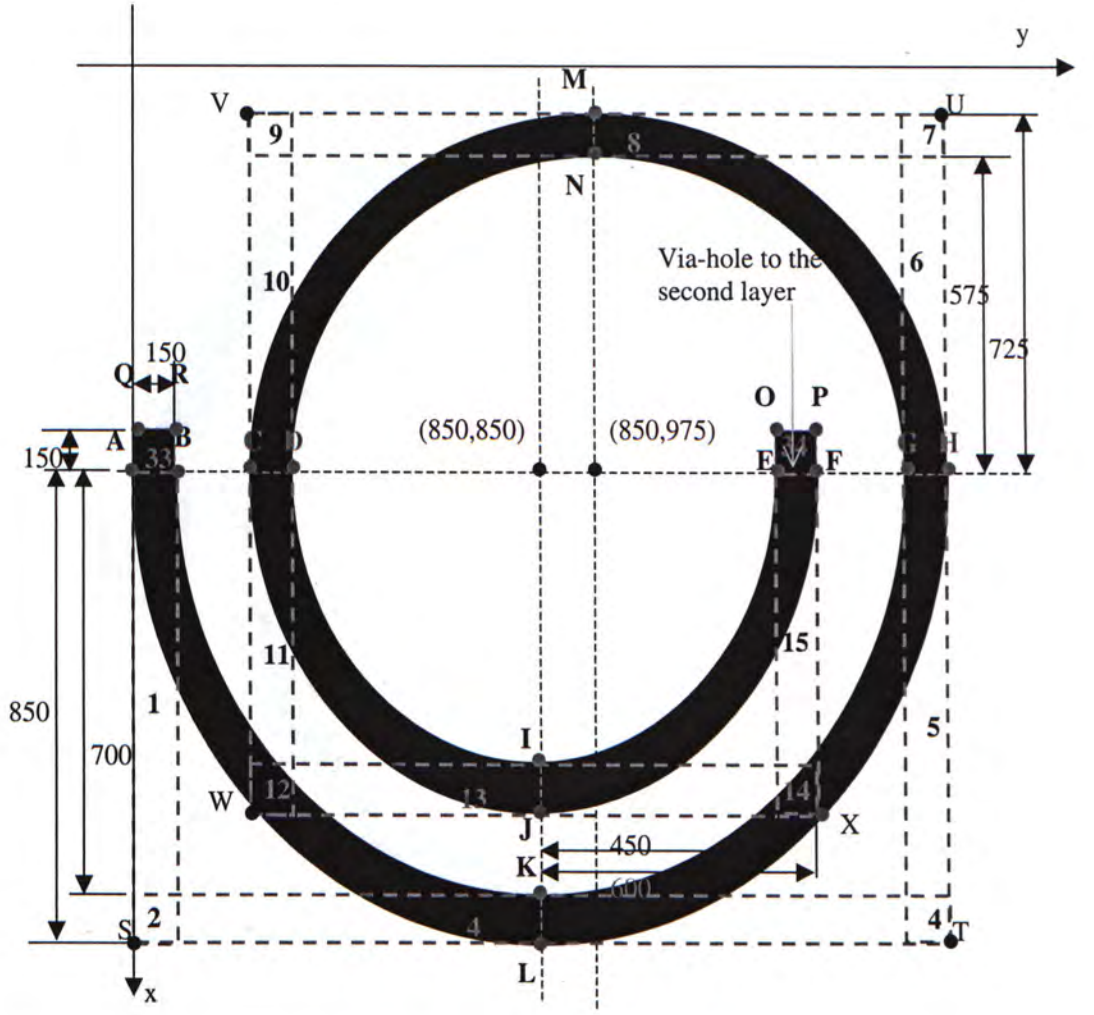

Figure A-1

The coordinates for labeled points:

A: (850,0), B: (850,150), C: (850, 250), D: (850, 400), E: (850, 1300), F: (850, 1450), G: (850, 1550), H: (850, 1700), I: (1300, 850), J: (1450, 850), K: (1550, 850), L: (1700, 850), M: (125,

975), N: (275, 975), O: (700, 1300), P: (700, 1450), Q: (700, 0), R: (700, 150), S: (1700, 0), T: (1700, 1700), U: (125, 1700), V: (125, 250), W: (1450, 250), X: (1450, 1450)

The second layer with z = 317.5 microns:

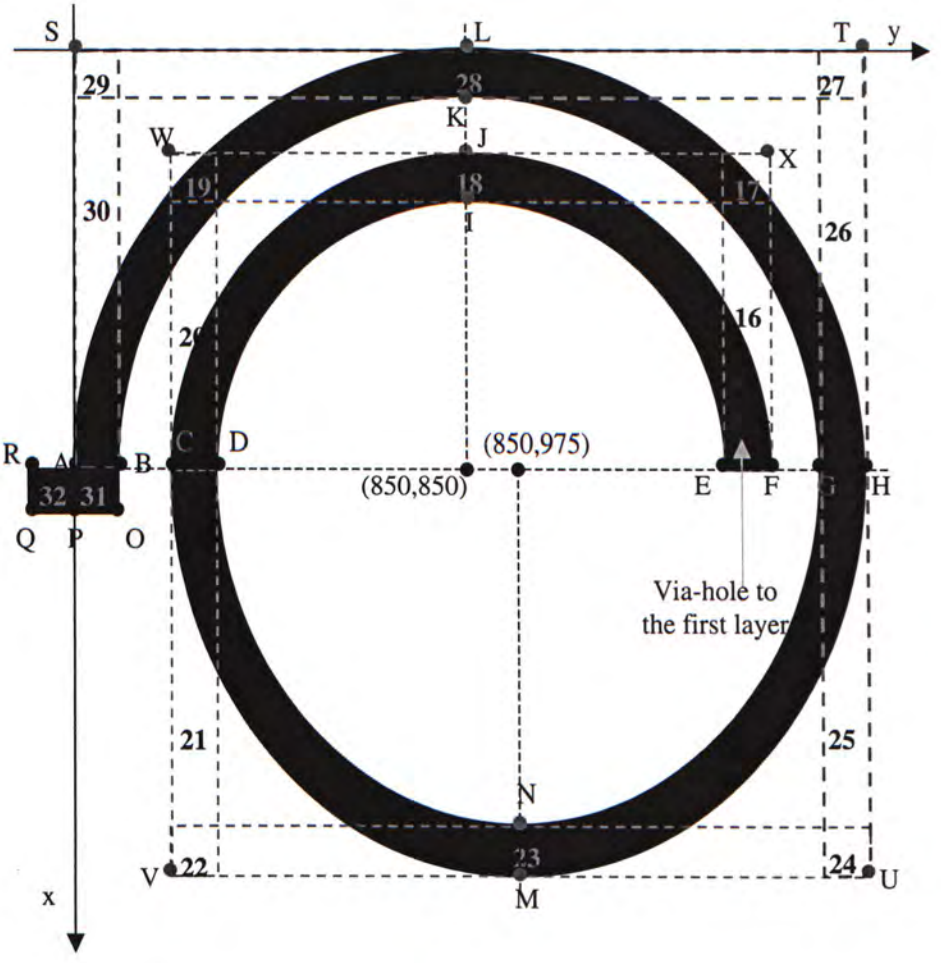

Figure A-2

A: (850, 0), B: (850, 150), C: (850, 250), D: (850, 400), E: (850, 1300), F: (850, 1450), G: (850, 1550), H: (850, 1700), I: (400, 850), J: (250, 850), K: (150, 850), L: (0, 850), M: (1550, 975), N: (1700, 975), O: (1000, 150), P: (1000, 0), Q: (1000, -150), R: (850, -150), S: (0, 0), T: (0, 1700), U: (1550, 1700), V: (1550, 150), W: (250, 150), X: (250, 1450)

APPENDIX B

LTCC Diplexer in Figure 3-13 in P.64

Some variables are defined for the simplification of presentation.

x_{C1}, x_{C24}, y_{C2}, x_{C3}, x_{C5}, R_{in_L2}, R_{in_L3}, y_{L4}, y_{L5}, y_{L6}, y_{L7}, y_{L8} are the variables to be optimized, whose values have been given in table 3-3 and labeled in figure B-1.

$L_x = 4500$, $L_y = 3200$, $via\_R = 50$

$W = 150$, $S = 100$, $via\_strip = 200$, $x0_{L2} = 400$, $L_{y1} = 1460$, $C_{gap} = 100$

$R_{in\_L4} = R_{in\_L5} = R_{in\_L6} = R_{in\_L7} = R_{in\_L8} = 50$

$R_{out\_Li} = R_{in\_Li} + W$, in which, $i = 2,3,...,8$

$y_{C1} = y_{C3} = y_{C4} = y_{C5} = L_{y1}$

$x0_{C5} = 4000 - x_{C5}$

$x0_{C32} = x0_{L2} + 2R_{out\_L2} + S + 2R_{out\_L4} + W + via\_strip$, $x_{C32} = x0_{C5} - \left(x0_{C32} + C_{gap}\right)$

$x0_{C24} = x0_{C32} - \left(x_{C24} + via\_strip\right)$, $x0_{C31} = x0_{C24} - \left(x_{C3} + C_{gap}\right)$

$x0_{C1} = x0_{C31} - \left(x_{C1} + C_{gap}\right)$

$R1_{in\_Li} = R_{out\_Li} - \left(1.5W + 0.5S\right)$, $R1_{out\_Li} = R1_{in\_Li} + W$, $i = 2,3,...$

$R2_{in\_Li} = R_{out\_Li} - \left(2W + S\right)$, $R2_{out\_Li} = R2_{in\_Li} + W$, $i = 2,3,...$

Low Pass Filter:

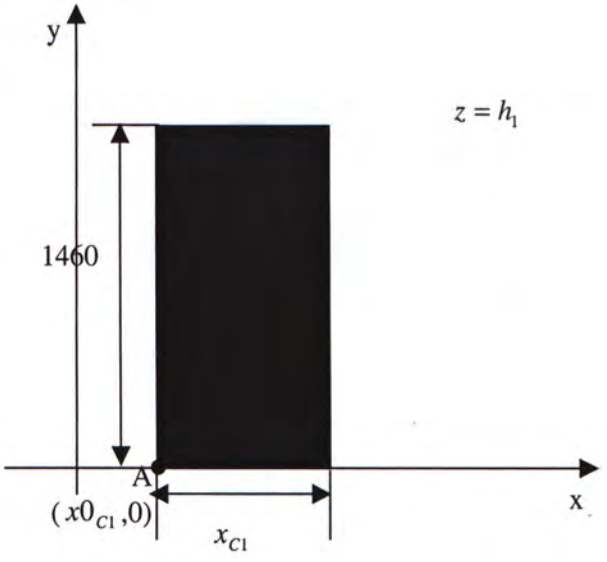

Figure B-1: C_1 in the low pass filter

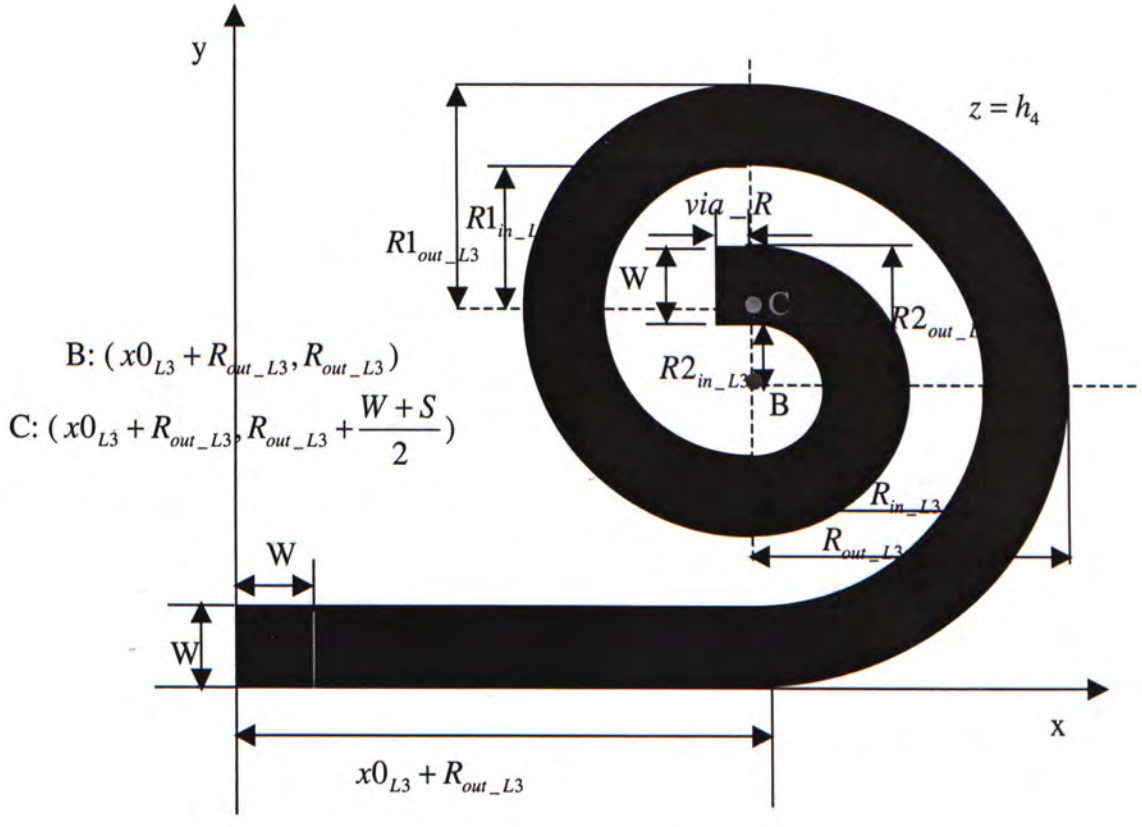

Figure B-2: L_3 in the low pass filter

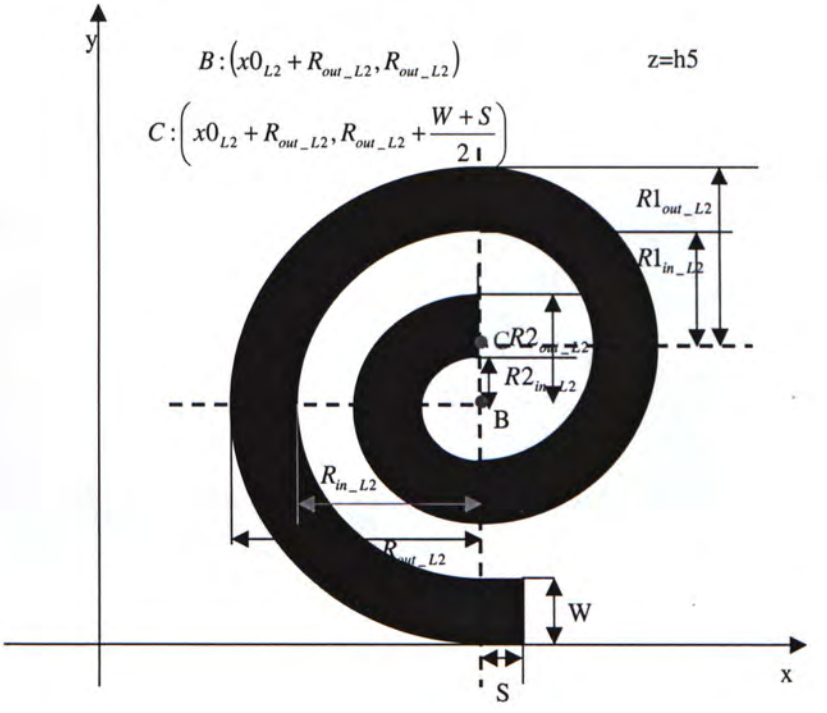

Figure B-3: the lower layer of L_2 in the low pass filter

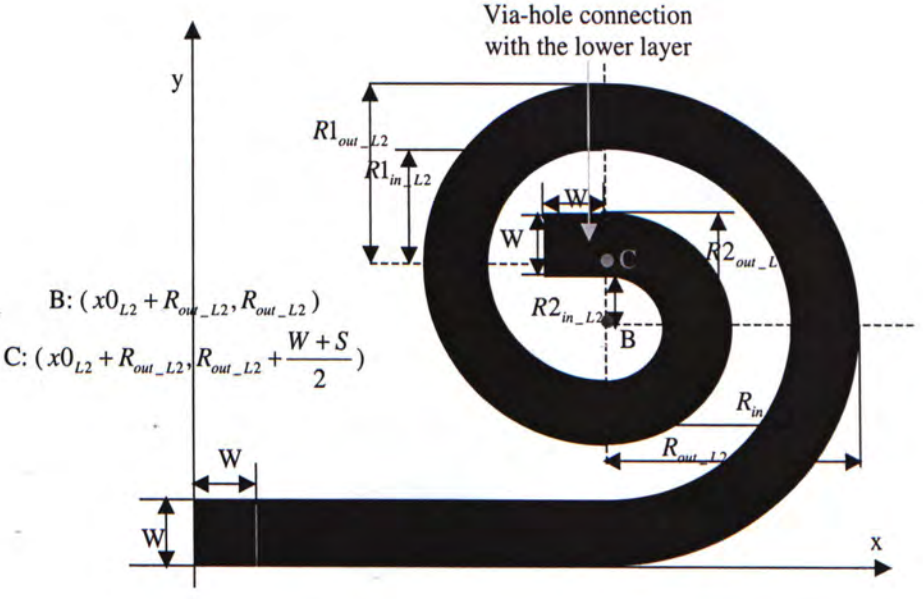

Figure B-4: the upper layer of L_2 in the low pass filter

High Pass Filter:

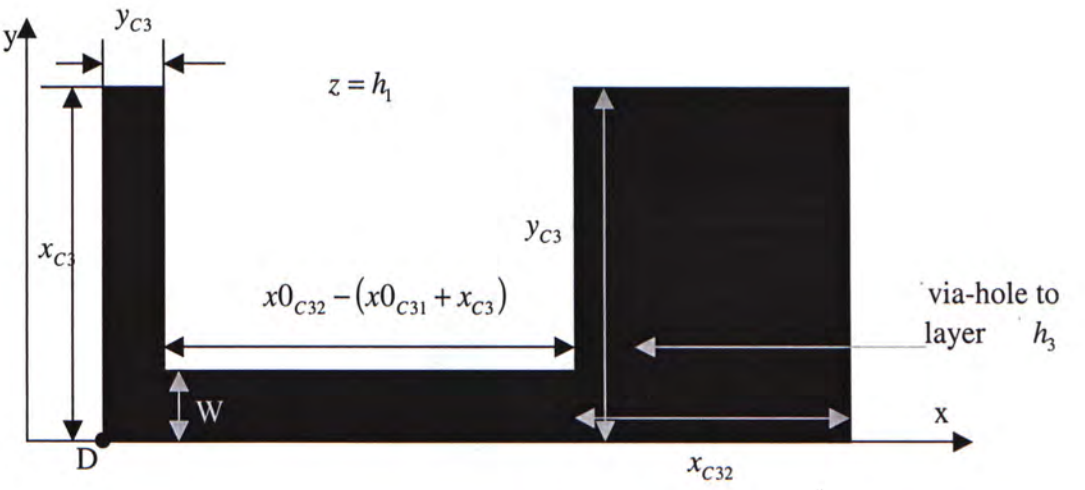

Figure B-5: C_3 in the high pass filter

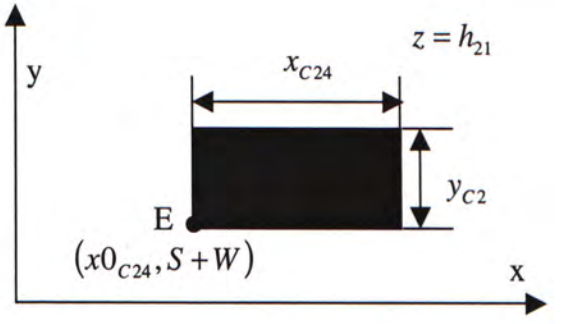

Figure B-6: C_4 in the high-pass filter

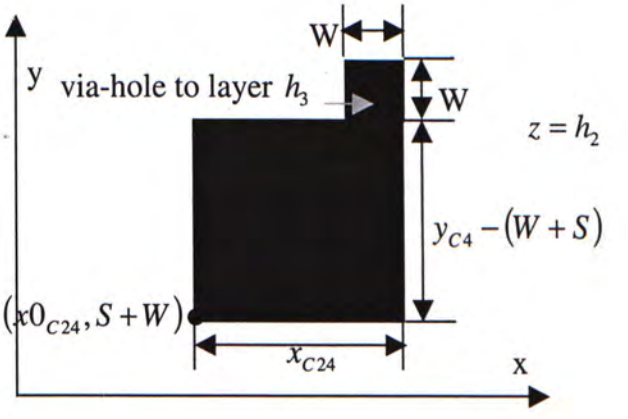

Figure B-7: C_{24} in the high-pass filter

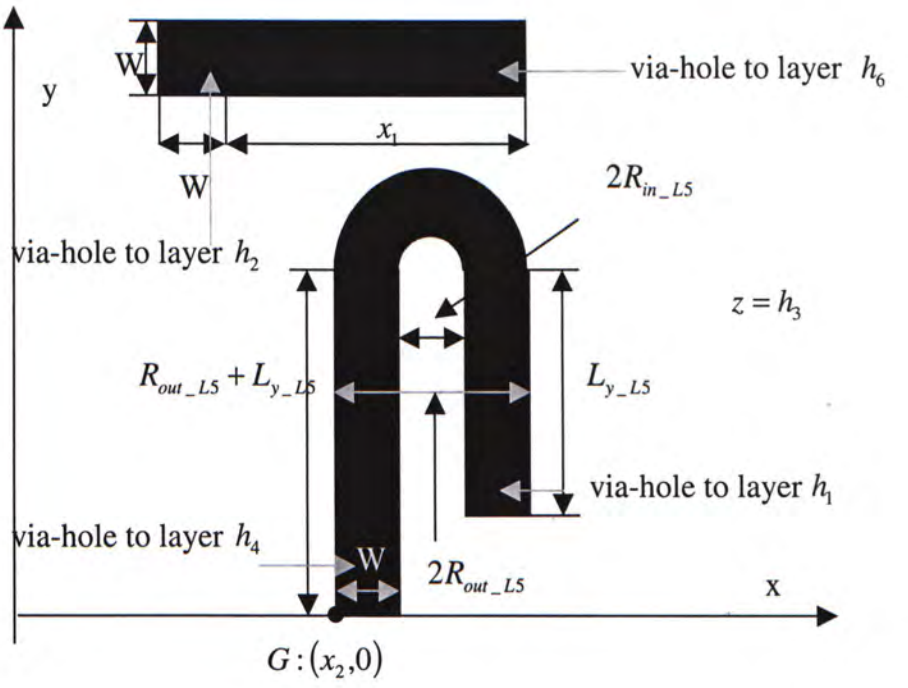

Figure B-8 (a) 1st layer of L_5

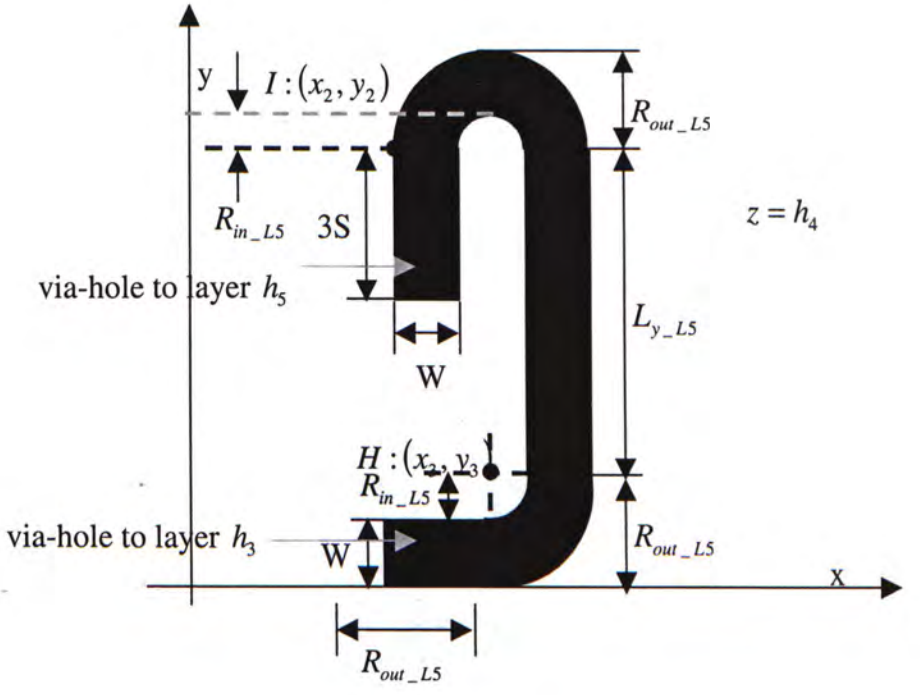

Figure B-8 (b) 2nd layer of L_5

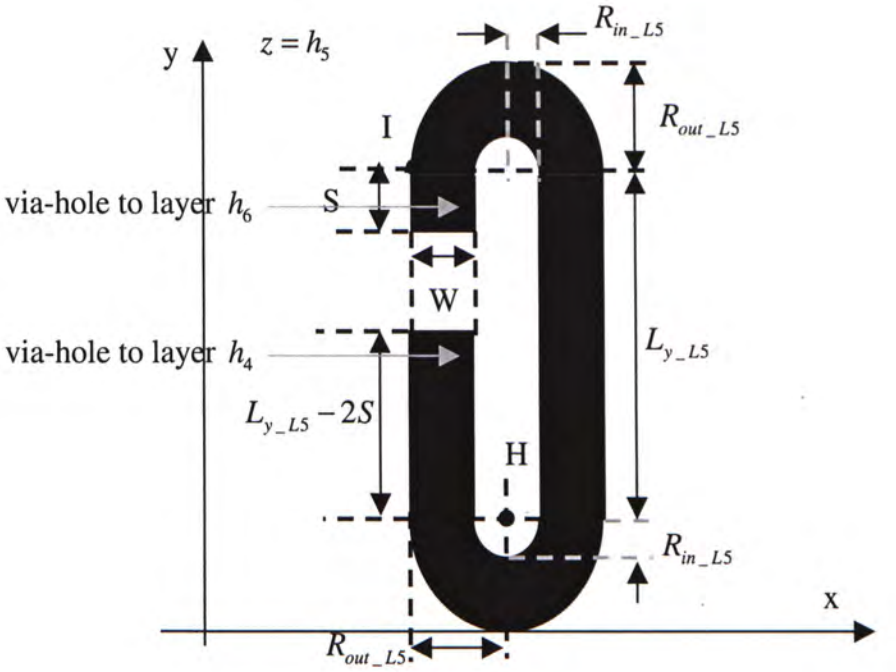

Figure B-8 (c) 3rd layer of L_5

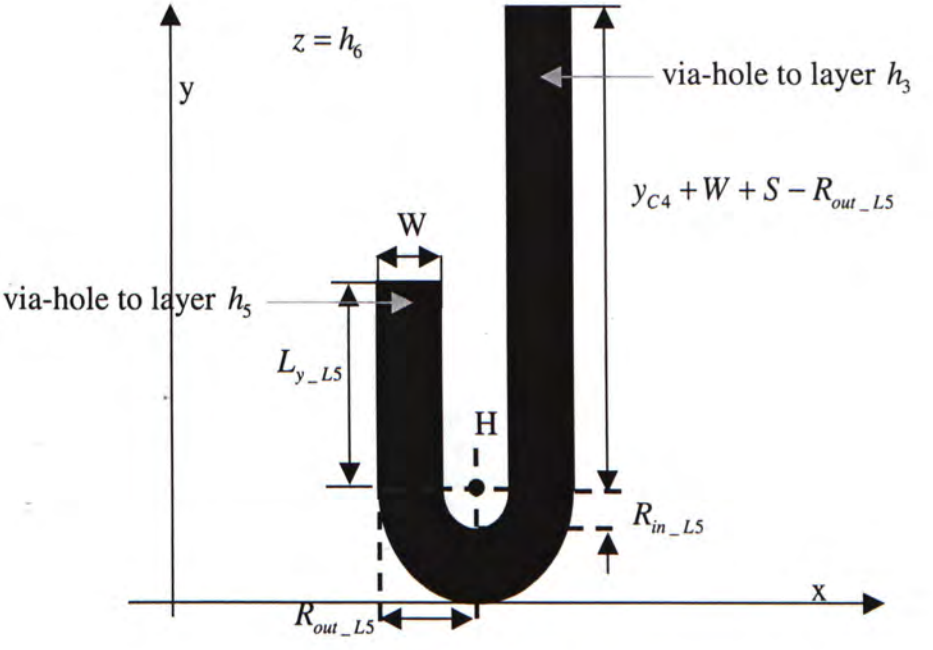

Figure B-8 (d) 4th layer of L_5

in which, $x_1 = 2\left(R_{out\_L5} + R_{out\_L4} + R_{out\_L2}\right) + S + W + x0_{L2} + via\_strip$

$x_2 = x0_{L2} + S + W + via\_strip + 2\left(R_{out\_L2} + R_{out\_L4}\right),\ y_2 = L_{y\_L5} + R_{out\_L5}$

$x_3 = x_2 + W + R_{in\_L5},\ y_3 = R_{out\_L5}$

Following is the inductor L_4 in the high-pass filter.

Like the case of L_5, some parameters are defined for the simplicity of presentation:

$x_4 = x0_{L2} + 2R_{out\_L2} + W + S,\ y_4 = L_{y\_L4} + R_{out\_L4}$

$x_5 = x_4 + W + R_{in\_L4},\ y_5 = R_{out\_L4}$

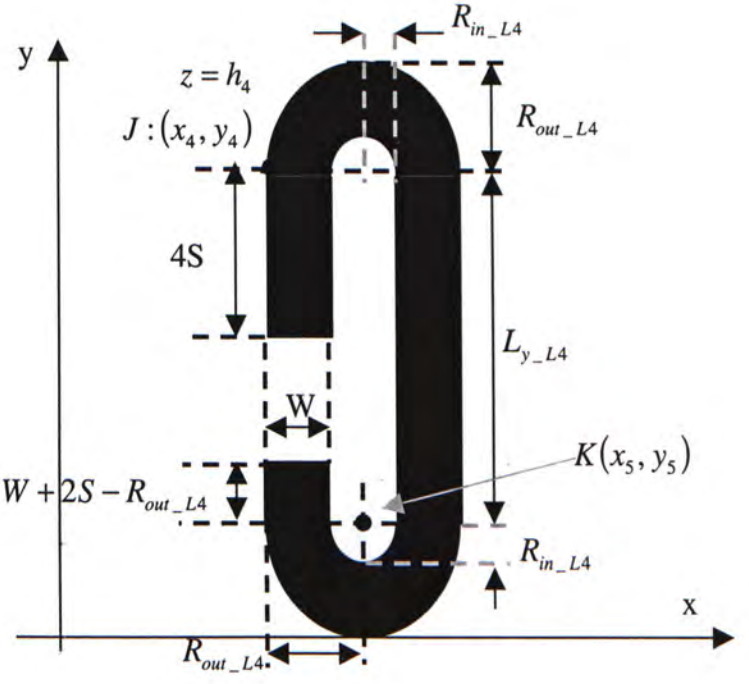

Figure B-9 (a) 1st layer of L_4

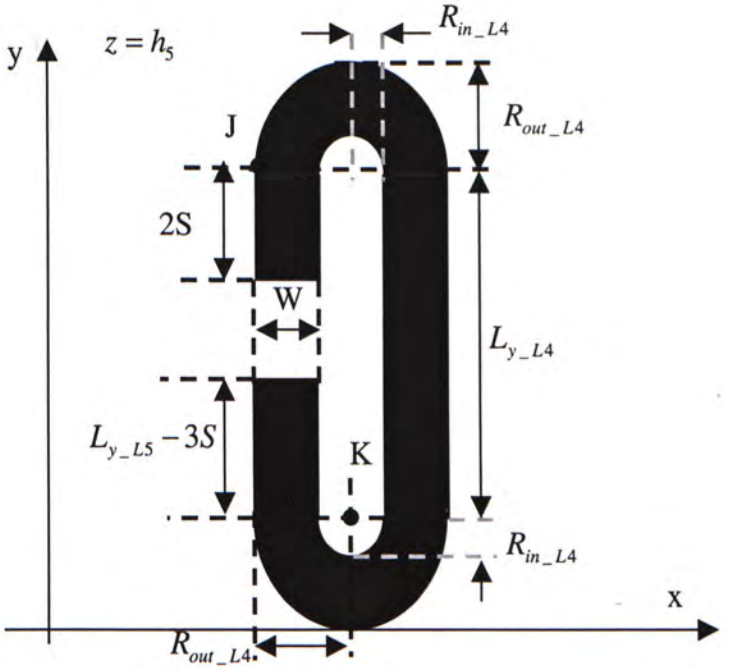

Figure B-9 (b) 2nd layer of L_4

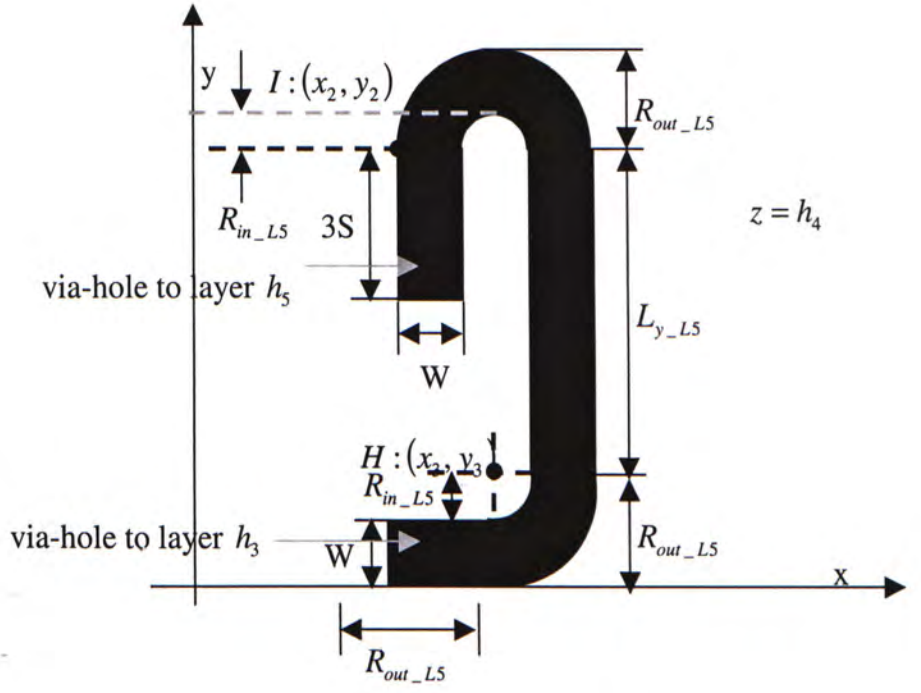

Figure B-9 (c) 3rd layer of L_4

REFERENCE:

[1] C. Hoer and C. Love, "Exact inductance equations for rectangular conductors with applications to more complicated geometries," J. Research of the National Bureau of Standard – C, Engineering and Instrumentation, vol. 69C, no. 2, pp. 127 – 137, April – June 1965

[2] A. E. Ruehli and P. A. Brennan, "Efficient capacitance calculations for three-dimenional multi-conductor systems," *IEEE Trans. Microwave Theory Tech.,* vol. 21, no. 2, pp. 76-82, Feb. 1973.

[3] A. E. Ruehli, "Electrical analysis of interconnections in a solid-state circuit environment," in Dig. IEEE Int. Solid-State Circuit Conf. (New York, 1972), pp. 64, 65 and pp. 216.

[4] Roger F. Harrington, "Field Computation by Moment Methods" New York: Macmillan, 1993, pp. 62-65.

[5] A. E. Ruehli, "Inductance calculations in a complex integrated circuit environment," IBM J. Res. Develop., vol. 16, pp. 470-481, Sept. 1972.

[6] A. Gopinath and P. Silvester, "Calculation of inductance of finite-length strips and its variation with frequency," *IEEE Trans. Microwave Theory Tech.,* vol. MTT-21, pp. 380-386, June 1973

[7] Lap Kun Yeung "PEEC Modeling Of LTCC Embedded RF Passive Devices" pp. 82, July 2002, Master of Philosophy Thesis, Chinese University of Hong Kong.

[8] S. M. Rao "Electromagnetic Scattering and Radiation of Arbitrarily-shaped Surfaces by Triangular Patch Modeling", August, 1980, Ph.D. Dissertation, The University of Mississippi.

[9] S. M. Rao, D. R. Wilton, and A. W. Glisson, "Electromagnetic scattering by surfaces of arbitrary shape", *IEEE Trans. Antennas Propagation,* vol. AP-30, pp. 409-418, May 1982.

[10] S. M. Rao, A. W. Glisson, D. R. Wilton, and B. S. Vidula, "A Simple Numerical Solution Procedure for Statics Problems Involving Arbitrary Shaped Surfaces", *IEEE Trans Antennas and Propagation*, vol. AP-27, pp. 604 - 608, September 1979.

[11] D. H. Schaubert, D. R. Wilton, and A. W. Glisson, "A tetrahedral modeling method for electromagnetic scattering by arbitrarily shaped inhomogeneous dielectric bodies" *IEEE Trans. Antennas Propagation,* vol. AP-32, pp. 77-85, January 1984.

[12] Vikram Jandhyala, Yong Wang, Dipanjan Gope, "Coupled Electromagnetic-Circuit Simulation of Arbitrarily-Shaped Conducting Structures using Triangular Meshes", Proceedings of the International Symposium on Quality Electronic Design, pp. 38, March 18-21, 2002.

[13] Aosheng Rong and Andreas C. Cangellaris, "Generalized PEEC models for three-dimensional interconnect structures and integrated passives of arbitrary shapes", Electrical Performance of Electronic Packaging, 29-31, Oct. 2001, pp. 225-228.

[14] Gupta, K.C., Garg, R., Chadha, R., Computer-Aided Design of Microwave Circuits, Artech House, 1981, pp 205-227.

[15] Philip J. Davis and Philip Rabinowitz, "Numerical integration", Waltham, Mass., Blaisdell Pub. Co., 1967

[16] Milton Abramowitz and Irene A. Stegun "Handbook of mathematical functions, with formulas, graphs, and mathematical tables" New York, Dover Publications, 1965, pp 916-919.

[17] J. W. Bandler, R. M. Bierncki, S. H. Chen, R. H. Hemmers, and K. Madsen, "Electromagnetic optimization exploiting aggressive space mapping" *IEEE Trans. Microwave Theory Tech.,* vol. 43, pp. 2874-2881, Dec. 1995.

[18] Narayana Rao, "Elements of engineering Electromagnetics" Upper Saddle River, N.J., Prentice Hall.

[19] Fang D.G., "Spectral Domain Approach in Electromagnetics" (in Chinese), Anhui Education Publishing House, 1995

[20] Yang J.J. "The Exact Image Theory for the Layered Medium Structure" (in Chinese), September 1987, East China Institute of Technology, pp11-13.

[21] Fang D.G., Yang J.J. and Delisle G.Y., "Discrete image theory for horizontal electric dipoles in a multi-layered medium above a conducting ground plane" IEE Proc. H, vol. 135 pp 297-303, 1988

[22] Y.L.Chow, J.J.Yang, D.G.Fang, and G.E.Howard, "A closed-form spatial Green's function for the thick microstrip substrate" *IEEE Trans. Microwave Theory Tech.,* vol. 39, pp. 588-592, Mar. 1991

[23] Robert A. Kipp and Chi H. Chan, "Complex Image Method for Sources in Bounded Regions of Multi-layer Structures" *IEEE Trans. Microwave Theory Tech.,* vol. 42, No. 5, May 1994

[24] Andrew J. Mackay and A. Mccowen, "An improved pencil-of-functions method and comparisons with traditional methods of pole extraction", *IEEE Trans. Antennas and Propagation*, vol. AP-35, No. 4, April 1987

[25] G. Dural and M. I. Aksun, "Closed-form Green's functions for general sources and stratified media", *IEEE Trans. Microwave Theory and Techniques*, vol. 43, No. 7, July 1995